Universitat Politècnica de Catalunya
Programa de Doctorat de Matemàtica Aplicada

Departament de Matemàtica Aplicada III

Continuous-discontinuous modelling for quasi-brittle failure: propagating cracks in a regularised bulk

by

Elena Tamayo-Mas

PhD dissertation
Advisor: Antonio Rodríguez-Ferran
Barcelona, October 2013

Al Guillem,

Abstract

Continuous-discontinuous modelling for quasi-brittle failure: propagating cracks in a regularised bulk

Elena Tamayo-Mas

A new strategy to describe failure of quasi-brittle materials —concrete, for example— is presented. Traditionally, numerical simulation of quasi-brittle failure has been tackled from two different points of view: damage mechanics and fracture mechanics. The former, which belongs to the family of continuous models, describes fracture as a process of strain localisation and damage growth. The latter, which falls in the family of discontinuous models, explicitly introduces displacement discontinuities. Recently, some new approaches that merge these two classical theories have been devised. Although these combined approaches allow a better characterisation of the whole failure process, there are still some issues that need to be addressed, specially regarding the model switching —from the continuous to the continuous-discontinuous strategy.

The goal of this thesis is to present a new contribution in this direction. Our main concern is to properly account for the three main difficulties that emerge when dealing with combined strategies: (1) the pathological mesh-dependence exhibited by local softening models needs to be corrected; (2) the crack-path location has to be determined and (3) the switching from the continuous to the continuous-discontinuous strategy should be done in such a way that the two approaches are energetically equivalent.

First, we extend the applicability to a two- and three-dimensional setting of an alternative approach to regularise strain-softening —where non-locality is introduced at the level of displacements rather than some internal variable. To this end, we propose new combined boundary conditions for the regularisation equation (for the smoothed displacement field). As illustrated with different two- and three-dimensional examples, these boundary conditions allow to obtain physical realistic results for the first stages of the failure process.

Second, we present a new combined formulation that allows the propagation of cracks through a regularised bulk. To define the crack-path, instead of the classical mechanical criteria, we propose to use a geometrical criterion. More specifically, given a regularised damage field $D(\boldsymbol{x})$, the discontinuity propagates following the direction

dictated by the medial axis of the isoline (or isosurface in 3D) $D(\boldsymbol{x}) = D^*$. That is, a geometric tool widely used for image analysis, computer vision applications or mesh generation purposes is used here to locate cracks. We illustrate the capabilities of this new approach by carrying out different two- and three-dimensional numerical tests.

Last, we propose a new criterion to estimate the energy not yet dissipated by the bulk when switching models, so it can be transferred to the cohesive crack. This ensures that the continuous and the continuous-discontinuous strategies are energetically equivalent. Compared to other existing techniques, we present a strategy that accounts for the different unloading branches of damage models thus better estimating the energy that has to be transferred. We illustrate the performance of this technique with one- and two-dimensional examples.

Resum

Modelització contínua-discontínua de la fallida de materials quasi-fràgils: propagant fissures en un medi regularitzat

Elena Tamayo-Mas

En aquesta tesi, presentem una nova estratègia per tal de descriure el procés de fallida de materials quasi-fràgils, com ara el formigó. Típicament la simulació numèrica d'aquest procés s'ha dut a terme mitjançant models de dany o models de fractura. Els primers —models continus— descriuen la fractura com un procés de localització de deformacions on el dany creix i es propaga. Els models de fractura, en canvi, són models discontinus que introdueixen de manera explícita discontinuïtats en el camp de desplaçaments. Recentment s'han proposat estratègies que combinen aquestes dues teories clàssiques. Tot i que aquestes formulacions alternatives permeten simular millor el procés de fallida, encara queden alguns aspectes per aclarir, especialment pel que fa al canvi de models —de l'estratègia contínua a la discontínua.

En aquesta tesi es presenta una nova estratègia contínua-discontínua. El nostre principal objectiu és proposar nous mètodes per tal de resoldre tres de les dificultats que presenten aquests models combinats: (1) solucionar la dependència patològica de la malla d'elements finits que presenten els models locals amb reblaniment; (2) determinar la trajectòria de la fissura i (3) assegurar-se que el canvi de models —del continu al discontinu— es fa de manera que les dues estratègies siguin energèticament equivalents.

En primer lloc, ampliem l'ús —per tal de poder simular problemes dos i tres dimensionals— d'una estratègia alternativa que regularitza el reblaniment de les lleis de tensió-deformació. Aquí la no-localitat s'introdueix a nivell del camp de desplaçaments i no a través d'una variable interna com succeeix en les formulacions estàndards. Per aquest motiu, proposem noves condicions de contorn combinades per l'equació de regularització (pel camp de desplaçaments suavitzat). Tal com s'observa en diferents exemples dos i tres dimensionals, aquestes condicions permeten simular de manera físicament realista les primeres etapes del procés de fallida.

En segon lloc, presentem una nova formulació combinada on les fissures es propaguen a través del medi regularitzat. Per tal de definir la trajectòria d'aquestes fissures, utilitzem un criteri geomètric, a diferència dels criteris mecànics clàssics. En

particular, sigui $D(\boldsymbol{x})$ un camp regularitzat de dany, les discontinuïtats es propaguen seguint la direcció marcada per l'eix mitjà de la isolínia (o isosuperfície mitjana en 3D) $D(\boldsymbol{x}) = D^*$. És a dir, utilitzem aquí aquesta eina geomètrica —molt emprada en d'altres aplicacions com ara l'anàlisi d'imatges, la visió artificial o la generació de malles— per tal de propagar les fissures. En aquest cas, donem també exemples dos i tres dimensionals.

Finalment, proposem un nou criteri per tal d'estimar l'energia que l'estructura encara no ha dissipat en el moment en que canviem de model, per tal que pugui ser transferida a la fissura cohesiva. D'aquesta manera, s'assegura que l'estratègia contínua i la contínua-discontínua siguin energèticament equivalents. En comparació amb d'altres tècniques, aquesta estratègia té en compte les diferents branques de descàrrega dels models de dany i permet estimar de manera més precisa l'energia que cal transmetre. Per tal de mostrar aquest balanç energètic es duen a terme diferents exemples en una i dues dimensions.

Acknowledgments

The work developed in this thesis would not have been possible without the support, guidance, motivation and suggestions of many people. I would like to express my sincere gratitude to all of them.

First of all, I would like to thank my advisor Antonio Rodríguez. *Antonio, moltes gràcies per introduir-me en el món de l'enginyeria. Gràcies per la infinita paciència durant tots aquests anys, per les múltiples tardes de pissarra i pels nombrosos consells que m'has donat. Però sobretot, gràcies per prohibir-me dir això no ho sé fer!*

My gratitude also to Antonio Huerta and to all LaCàN members for these years together. Special thanks to Coque, Irene, Marino, Pedro and Yongxing for all their comments during the NMASE's and our research meetings on Evolving smeared discontinuities. Also many thanks to David O.: *David, gràcies per fer-me la vida una mica més fàcil, ajudant-me sempre que ha calgut.*

I really enjoyed the daily life with the LaCàN people. Many thanks to Abel, Aleks, David M., Eva, Francho, Giorgio, Imma, Joan, Jordi, Marco, Miquel, Omid, Raquel, Raúl and Xevi. *¡Gracias por los pasteles, los cafés, las cenas y las birras! Eloi, gràcies per ajudar-me amb un somriure cada vegada que he necessitat fer una malla, utilitzar el Paraview o fer servir l'Inkscape. Alba, gràcies pel teu suport incondicional en els inicis d'aquesta tesi. Esther, gràcies per enredar-me a entrar al LaCàN, per resoldre'm tots els dubtes que he tingut d'X-FEM sempre que ho he necessitat i per fer que la meva experiència com a docent fos immillorable! Cris, gracias por la energía que me has transmitido en esta última etapa, por estar siempre ahí y por ser la mejor estresada con quien poder quemar el último cartucho.*

Many thanks to all my friends, who have helped me not to go crazy. Special thanks to Arnau, Inma and Víctor for being always there during our parallel PhD trajectories. *De debò, gràcies per fer-me costat, pels sopars, pels mojitos i en definitiva, per tots els bons moments compartits. Us agraeixo també a vosaltres, als de mates, als terminals i a les de Sabadell, haver-me ajudat a no perdre el món de vista.*

Many thanks to my family. *Papes, gràcies per inculcar-me els valors de l'esforç, de la feina ben feta, de la responsabilitat i de la constància. Sense ells, no hauria arribat pas fins aquí. Merci, de debò: per ser-hi i escoltar-me.* And last but not least... *gràcies a tu, Guillem, per ser el meu pilar en els bons moments, però també en els difícils. Gràcies per tot el que hem viscut i gràcies per deixar-me ser la teva companya en aquesta nova etapa que comencem. Espera'm, que tot i el fred, ara vinc!*

Contents

List of figures

List of tables

List of symbols

Latin symbols

A	Parameter that controls the residual strength in a damage model
$\mathbf{B}$	Derivative shape function matrix
B	Parameter that controls the slope of softening in a damage model
$\boldsymbol{C}$	Elastic stiffness tensor
$\mathbf{D}$	Diffusivity matrix
$\mathbf{D}_\psi$	Enriched diffusivity matrix
D	Scalar damage parameter
D^*	Isovalue (to set the domain for the medial axis computation)
D_{crit}	Critical damage value
E	Young's modulus
G	Fracture energy
I_1	First invariant of the strain tensor
J_2	Second invariant of the deviatoric strain tensor
$\mathbf{K}_{\text{BC}}$	Combined boundary conditions matrix
$\mathbf{K}_{\psi,\text{BC}}$	Enriched combined boundary conditions matrix
$\mathbf{K}_{\text{cohesion}}$	Cohesive matrix
$\mathbf{K}_{\text{loc}}$	Local tangent matrix
$\mathbf{K}_{\psi,\text{loc}}$	Enriched local tangent matrix
$\mathbf{K}_{\text{sec}}$	Secant tangent matrix
$\mathbf{K}_{\psi,\text{sec}}$	Enriched secant tangent matrix
k	Ratio of compressive strength to tensile strength
ℓ	Characteristic length of a non-local damage model
$\mathbf{M}$	Mass matrix
$\mathbf{M}_\psi$	Enriched mass matrix
$\mathbf{N}$	Matrix of standard finite element shape functions
$\boldsymbol{n}$	Outward unit normal to the boundary
$\mathbf{T}$	Matrix that takes into account the cohesive forces
$\boldsymbol{t}_1$, $\boldsymbol{t}_2$	Tangent unit vectors to the boundary
$\bar{\boldsymbol{t}}$	Traction on the Neumann boundary
$\bar{\boldsymbol{t}}_d$	Traction on the discontinuity surface

$\boldsymbol{u}$	Standard displacement field
$\boldsymbol{u}^1$	Regular standard displacement field
$\boldsymbol{u}^2$	Enhanced standard displacement field
$\mathbf{u}$	Standard nodal displacement vector
$\mathbf{u}^1$	Regular standard nodal displacement vector
$\mathbf{u}^2$	Enhanced standard nodal displacement vector
$\widetilde{\boldsymbol{u}}$	Smoothed displacement field
$\widetilde{\boldsymbol{u}}^1$	Regular smoothed displacement field
$\widetilde{\boldsymbol{u}}^2$	Enhanced smoothed displacement field
$\widetilde{\mathbf{u}}$	Smoothed nodal displacement vector
$\widetilde{\mathbf{u}}^1$	Regular smoothed nodal displacement vector
$\widetilde{\mathbf{u}}^2$	Enhanced smoothed nodal displacement vector
u^*	Prescribed displacement on the Dirichlet boundary
$[\![\boldsymbol{u}]\!]$	Crack opening
$[\![\boldsymbol{u}]\!]_n$	Normal component of $[\![\boldsymbol{u}]\!]$
$[\![\boldsymbol{u}]\!]_s$	Sliding component of $[\![\boldsymbol{u}]\!]$
$\boldsymbol{x}$	Spatial coordinate vector
Y	Local state variable of a damage model
$\widetilde{Y}$	Smoothed state variable of a damage model
Y_0	Damage initiation state variable
Y_f	Maximum admissible value for the state variable

Greek symbols

β	Slope of the stress-strain relation
Γ	Boundary surface
Γ_d	Discontinuity surface
Γ_t	Boundary surface where tractions are prescribed (Neumann boundary)
Γ_u	Boundary surface where displacements are prescribed (Dirichlet boundary)
$\boldsymbol{\varepsilon}$	Small strain tensor
$\widetilde{\boldsymbol{\varepsilon}}$	Smoothed small strain tensor
ε_i	Principal strains
θ	Separation angle
λ_D	Width of the damage profile (1D)
ν	Poisson's ratio
$\boldsymbol{\sigma}$	Stress tensor
τ	Equivalent effective stress
τ_0	Damage initiation equivalent effective stress
τ_i	Principal effective stresses
Ψ_C	Energy dissipated with a continuous model
Ψ_{CD}	Energy dissipated with a continuous-discontinuous model
Ψ_{transfer}	Energy that needs to be transferred to the cohesive crack

ψ	Sign function
ψ_C	Specific energy in a continuous model
Ω	Domain of $\mathbb{R}^n$ occupied by the solid in a space of n dimensions ($n = 1, 2, 3$)
$\boldsymbol{\omega}$	Test function of the space of admissible local displacement (disp.) variations
$\boldsymbol{\omega}^1$	Regular test function of the space of admissible local disp. variations
$\boldsymbol{\omega}^2$	Enhanced test function of the space of admissible local disp. variations
$\widetilde{\boldsymbol{\omega}}$	Test function of the space of admissible smoothed disp. variations
$\widetilde{\boldsymbol{\omega}}^1$	Regular test function of the space of admissible smoothed disp. variations
$\widetilde{\boldsymbol{\omega}}^2$	Enhanced test function of the space of admissible smoothed disp. variations

Operators

In the following, a scalar is represented with the italic type S, a vector with the bold-face type $\boldsymbol{V}$ and tensors with the bold-face type $\mathbf{A}, \mathbf{B}$.

:	Double contraction Double contraction of two tensors: $\mathbf{A} : \mathbf{B} = A_{ij}B_{ij}$
∇	Gradient Gradient of a scalar in cartesian coordinates: $\nabla S = \frac{\partial S}{\partial x}\boldsymbol{e}_x + \frac{\partial S}{\partial y}\boldsymbol{e}_y + \frac{\partial S}{\partial z}\boldsymbol{e}_z$ Gradient of a vector in cartesian coordinates: $\nabla \boldsymbol{V} = \begin{pmatrix} \frac{\partial V_x}{\partial x} & \frac{\partial V_x}{\partial y} & \frac{\partial V_x}{\partial z} \\ \frac{\partial V_y}{\partial x} & \frac{\partial V_y}{\partial y} & \frac{\partial V_y}{\partial z} \\ \frac{\partial V_z}{\partial x} & \frac{\partial V_z}{\partial y} & \frac{\partial V_z}{\partial z} \end{pmatrix}$
$\nabla\cdot$	Divergence Divergence of a vector in cartesian coordinates: $\nabla \cdot \boldsymbol{V} = \frac{\partial V_x}{\partial x} + \frac{\partial V_y}{\partial y} + \frac{\partial V_z}{\partial z}$
∇^2	Laplacian Laplacian of a scalar in cartesian coordinates: $\nabla^2 S = \frac{\partial^2 S}{\partial x^2} + \frac{\partial^2 S}{\partial y^2} + \frac{\partial^2 S}{\partial z^2}$
∇^s	Symmetrised gradient Symmetrised gradient of a vector in cartesian coordinates: $\nabla^s \boldsymbol{V} = \frac{1}{2}\left(\nabla \boldsymbol{V} + \nabla \boldsymbol{V}^T\right)$

Acronyms

$\theta-$SMA	$\theta-$simplified medial axis
FEM	Finite element method
MA	Medial axis
PDE	Partial differential equation
SEL	Bažant's Size Effect Law
TLS	Thick level set
X-FEM	Extended finite element method

Chapter 1

Introduction

1.1 Motivation

The understanding of material failure —the reliable prediction of material degradation, crack initiation and propagation— is of vital importance in engineering and materials science. To this end, both experimental, through which real material structures can be analysed, and numerical tests can be carried out. Although both approaches are complementary, there are several advantages of performing numerical simulations. Indeed, compared to laboratory experiments, numerical tests can be easily repeated and allow the analysis of full scale structures for long time periods at a lower cost.

From a numerical viewpoint, failure of quasi-brittle materials —concrete or rocks, for example— has been extensively studied. Traditionally, two different kinds of approaches have been used: (a) damage mechanics, which belongs to the family of continuous models, and (b) fracture mechanics, which falls in the family of discontinuous models.

Continuum models for failure analysis —damage or softening plasticity— are characterised by continuous displacement fields. As discussed by Lemaitre and Chaboche (1990), they may describe the early stages of the failure process, between the undamaged state and macroscopic crack initiation. They are based on constitutive laws with *strain softening*, which leads to an ill-posed problem —if standard local models are used— when the peak in the stress-strain curve is reached. As a consequence, and regarding numerical simulations, the solution with the smallest energy

dissipation that is available in the finite dimensional solution space is obtained. To overcome this physically unrealistic behaviour, different solutions have been proposed in the literature, see Jirásek (2002) and the recent review by Rabczuk (2013). One of these remedies are the so-called non-local continua, in which a non-local effect is introduced either by integral-type (Pijaudier-Cabot and Bažant (1987), Bažant and Jirásek (2002)) or gradient-type (de Borst et al. (1995), Peerlings et al. (1998)) formulations. However, despite the regularisation, they cannot be used to simulate macroscopic cracks, since displacement discontinuities are not introduced.

In contrast to continuum models, with smeared cracks, fracture mechanics describes failure by means of a discontinuous displacement field. Hence, they can be employed in order to capture the last stages of failure, when cracks are physically observed. From a numerical viewpoint, their applications were first restricted, since the standard finite element method (FEM), which performs well approximating smooth functions, is not suited for the approximation of non-smooth solutions. Nevertheless, different methods, see Jirásek and Belytschko (2002), such as the eXtended Finite Element Method (X-FEM) (Belytschko and Black (1999), Moës et al. (1999)) have emerged in order to overcome this limitation and nowadays discontinuous models can adequately be used in the final stages of failure. However, discontinuous models cannot describe neither damage inception nor its diffuse propagation.

Recently, some new approaches that merge these two classical theories —damage and fracture mechanics— have emerged. The basic idea of these continuous-discontinuous strategies is to employ damage mechanics in order to describe the inception and the propagation of damage and fracture mechanics in order to deal with cracks and material separation. Although they have proved efficient to simulate the whole failure process, further research is needed to better understand their capabilities.

The objective of this dissertation is to present a new continuous-discontinuous approach. For the early stages of the failure process, a gradient-enhanced model based on smoothed displacements is employed. When damage parameter exceeds a critical value, a discontinuous approximation of the displacement field is incorporated. Special emphasis is placed on some of the arising difficulties when dealing with the transition from regularised damage models to evolving cracks such as the crack path tracking or the energetic consistency between the models.

1.2 Goals and layout of this thesis

The objective of this thesis is to develop a finite element approach for quasi-brittle failure that bridges damage and fracture mechanics. To this end, four goals have been considered:

1. **To extend the applicability of smoothed displacements to a multi-dimensional setting**. Introducing non-locality at the level of displacements (rather than some internal variable) is an alternative way to obtain physically realistic results and to avoid the typical pathological mesh sensitivity exhibited by classical continuum theories. This idea, presented by Rodríguez-Ferran et al. (2005), emerged as a computationally attractive approach to regularise softening, but only the one-dimensional setting was considered. As discussed by Jirásek and Marfia (2005), the extension to a multidimensional context is not straightforward, since it requires either the modification of the averaging operator (for the integral-type version) or appropriate boundary conditions (for the gradient-type version). In Chapter 3, we focus on the implicit gradient version of this alternative regularisation method. We discuss the shortcomings of usual boundary conditions —Dirichlet, homogeneous Neumann and non-homogeneous Neumann— and we propose new conditions —combined conditions— that provide physically realistic results in two- and three-dimensional settings.

2. **To propose the continuous-discontinuous formulation based on non-local displacements**. Combined approaches have emerged as a suitable manner to overcome the limitations of classical failure approaches —damage and fracture mechanics. In Chapters 4 and 5, we describe how to merge smoothed displacements with discontinuities. Firstly, in Chapter 4, we propose to drive the model switching —from the continuous to the continuous-discontinuous strategy— by means of a critical damage value $D_{\text{crit}} \simeq 1$. Thus, we focus on the coupling between smoothed displacements and traction-free cracks. Secondly, in Chapter 5, the transition is induced by a critical damage value $D_{\text{crit}} < 1$ thus introducing a cohesive crack. Details on the variational formulation of the proposed model, on the consistent tangent matrix needed to attain quadratic convergence in the full Newton-Raphson method and on its numerical integra-

tion when dealing with cracked elements are given in Appendices A, B and C respectively.

3. **To propose a new criterion (based on geometrical assumptions) to track the crack path**. In a regularised continuous model, the crack path cannot be analytically derived. In other words, fracture mechanics cannot be employed, since the critical imperfection from which cracking initiates is unknown. Therefore, other criteria should be used. Typically, this is tackled from a mechanical point of view: Gauss-point mechanical quantities —non-local stress, non-local strain or damage— ahead of the crack tip are used to locate the propagating discontinuity. However, due to the singularity of the stress and strain fields, an incorrect crack propagation may be derived. Hence, in Chapter 4, we propose an alternative way of defining the direction of the crack path: the discontinuity propagates following the direction dictated by the medial axis, see Blum (1967), of the already formed damage field. Since this technique is exclusively based on the shape of this regularised field, no mesh sensitivity is observed when determining the crack direction.

4. **To propose a new criterion to estimate the energy that needs to be transferred to the cohesive interface**. The *equivalent crack concept* states that a damage zone can be replaced by a discrete crack provided that the two models are energetically equivalent. Therefore, if the transition takes place when the material is not fully degraded (if $D_{\text{crit}} < 1$), the energy not yet dissipated by the continuous approach should be transferred to the cohesive zone. However, the applicability of this energy balance is hampered by one main drawback: without carrying out a continuous simulation first, the amount of energy to be transferred is not known. As a consequence, it needs to be estimated. In Chapter 5 we discuss the shortcomings of not predicting accurately the unloading response (as done in some existing combined techniques) and we propose a new strategy that provides a more accurate approximation of the fracture energy.

Chapter 2

State of the art

This chapter provides an overview of some of the challenges when dealing with numerical simulation of quasi-brittle failure. This overview focuses on strategies where the bulk material is modelled as a continuum. First, continuum approaches —*continuum failure models*— are considered in Section 2.2. Our main concern is to review the existing techniques to eliminate the mesh dependence exhibited by local models with softening. Second, continuum models with discontinuities —*discontinuous failure models*— are addressed in Section 2.3. The advantages and disadvantages of some of the most popular computational methods for fracture are discussed. Finally, different continuous-discontinuous techniques are reviewed in Section 2.4. Special attention toward the model switching —from the continuum to the discrete strategy— is given.

2.1 Introduction

Numerical simulation of failure of quasi-brittle materials —such as concrete or rocks— is traditionally tackled from two different points of view: continuous and discontinuous approaches. On the one hand, *continuous approaches* simulate failure assuming a continuously differentiable displacement field throughout a continuum, thus leading to a continuous strain field. Hence, cracks are represented by continuum regions that have lost their load-carrying capacity. On the other hand, *discontinuous approaches* describe cracks by means of a discontinuous displacement field. Therefore, the strain field consists of two contributions: a regular part obtained by standard differentia-

tion of the displacement field and a singular part dealing with the contribution of the displacement jump.

In fact, and within the framework of non-linear finite element strategies for failure simulation, *discrete approaches* can also be employed, see Grassl and Jirásek (2010). They are considerably different from the two above-mentioned strategies, since they describe failure processes by means of discrete elements that interact, see Kawai (1978) and Cundall and Strack (1979). That is, the bulk of the material is not modelled as a continuum —as done in continuous or discontinuous approaches— but by means of particles or lattices. Since these approaches are not addressed in this dissertation, the terms *discontinuous* and *discrete* will be used as synonyms to refer to *continuum models with discontinuities*.

2.2 Continuous failure models

Description of quasi-brittle failure requires constitutive laws with *strain softening*. That is, it requires stress-strain laws that are nearly linear up to the peak stress, whereas they decrease after it is reached. This phenomenon may be conveniently described by models based on continuum mechanics. If classical (local) continuum theories are used, i.e. if the stress at a point uniquely depends on the strain history at that point, strain softening leads to a physically unrealistic treatment of the energy dissipated during the failure process, see Jirásek (2007). This local dependence between stress and strain leads to a process zone whose thickness may become arbitrarily small. As a consequence, and regarding numerical simulations, the results suffer from sensitivity to the discretisation parameters such as the mesh size. Indeed, let us consider a bar under uniaxial tension (with imposed displacements at the free side), see Figure 2.1(a). If a local damage model is used, both the slope of the post-peak branch (in the force-displacement curve) and the strain profiles strongly depend on the number of elements of the finite element mesh, see Figures 2.1(b) and 2.1(c) respectively.

Different solutions have been proposed in the literature to remedy this physically unrealistic behaviour. For a general overview, we refer to the recent review by Rabczuk (2013) and references therein. Here, some of the most popular techniques are briefly reviewed.

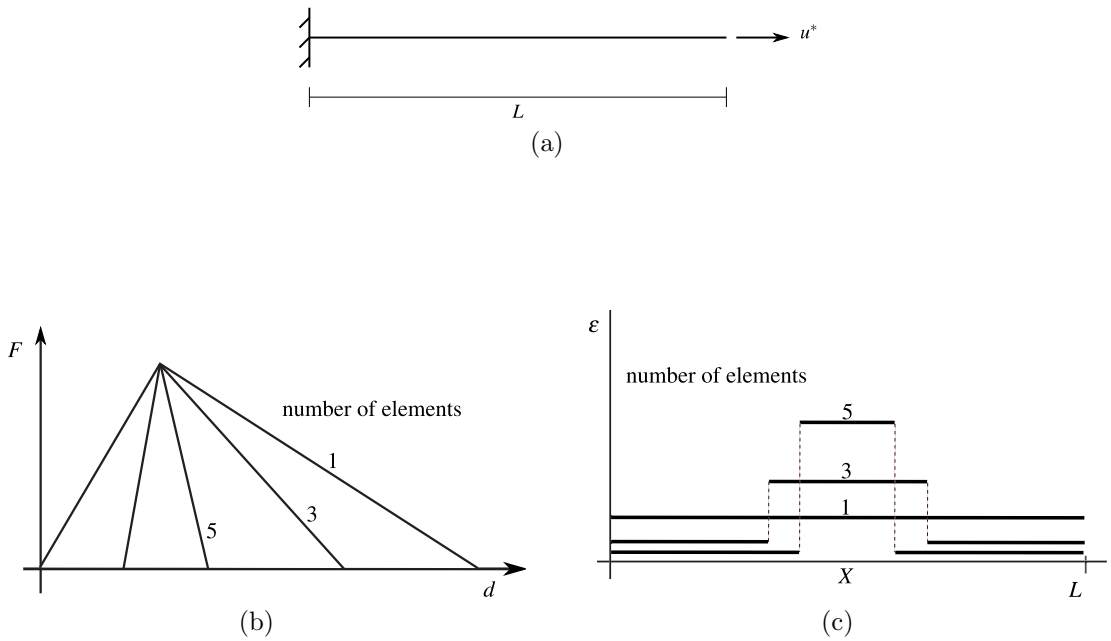

Figure 2.1: If a local damage model is used to simulate a (a) uniaxial tension test, a pathological mesh dependence is observed. Indeed, both (b) load-displacement curves and (c) strain profiles depend on the mesh refinement.

Crack-band approach. A possible remedy is to use the crack band model presented by Bažant and Oh (1983). This method, also called *fracture energy approach* or the *mesh-adjusted softening modulus*, consists of adjusting the post-peak slope of the stress-strain curve by means of the element size. This remedy presents one main advantage. Despite the adjustment, the formulation remains local. Therefore, the structure of the finite element code does not require major changes. This may be easily exploited in many practical engineering computations. However, as discussed by Jirásek and Bauer (2012), the applicability of this method is hampered by one main drawback. The criterion for estimating the width of the crack band is not straightforward. Although it is often considered as the element size, the effective width of the localised band depends on the element type, the element shape and the direction of the crack band with respect to the mesh edges.

Regularised formulations. These models, often called *localisation limiters*, incorporate an additional material parameter —the characteristic length— to prevent strain localisation into an arbitrarily small volume. That is, the process zone is en-

forced to have a certain minimum width. The main drawback of this remedy is the quantitative determination of this internal length parameter. Indeed, it remains a difficult and debated issue, since it cannot be directly measured and it may be only inferred by inverse analysis of test results. Examples of these models include non-local integral and gradient-enriched formulations.

In *integral-type models*, a certain variable is replaced by its non-local counterpart. This is obtained by weighted averaging over a spatial neighbourhood of each point under consideration. That is, the stress at a given point does not only depend on the strain at that point but also on the strain of the considered neighbourhood. A number of non-local formulations have been published, starting from the paper by Pijaudier-Cabot and Bažant (1987). Nevertheless, as discussed by Jirásek (1998), not all of them provide an appropriate description of the complete failure process. Indeed, if the equivalent strain or the energy release rate are selected to incorporate non-locality, the complete fracture is correctly reproduced. However, averaging the damage variable or the inelastic stress may lead to spurious residual stresses and to an unrealistic spread of the softening area. For a detailed overview of these non-local models, we refer to the review by Bažant and Jirásek (2002).

Gradient-type non-local models, see de Borst et al. (1995) and Peerlings et al. (1998), can be considered as an approximation to integral-type models, with a differential —rather than integral— relation between local and non-local variables. In other words, a partial differential equation (PDE) is added to the system relating the local and non-local variables. Gradient-type formulations present one main advantage. From a mathematical viewpoint, they are local models, since non-local interaction is accounted for by means of higher-order derivatives. Nevertheless, its main drawback is the requirement of appropriate boundary conditions for the PDE, which is still a debated issue.

In this dissertation, a gradient-enriched formulation is used to regularise softening.

2.3 Discontinuous failure models

Numerical simulation of failure phenomena can also be tackled by means of discontinuous models. The main idea of these techniques is to consider a displacement field with jumps across a line (in a two-dimensional setting) or a surface (in 3D

problems). These jumps, technically named *strong discontinuities*, result then in an unbounded strain field at the discontinuity. If strong discontinuities are used, see the cohesive crack model introduced by Hillerborg et al. (1976), softening is described by a traction-separation law, whose definition depends on the mode of fracture, see Figure 2.2. Hence, tractions transmitted by the crack are related to the displacement jump.

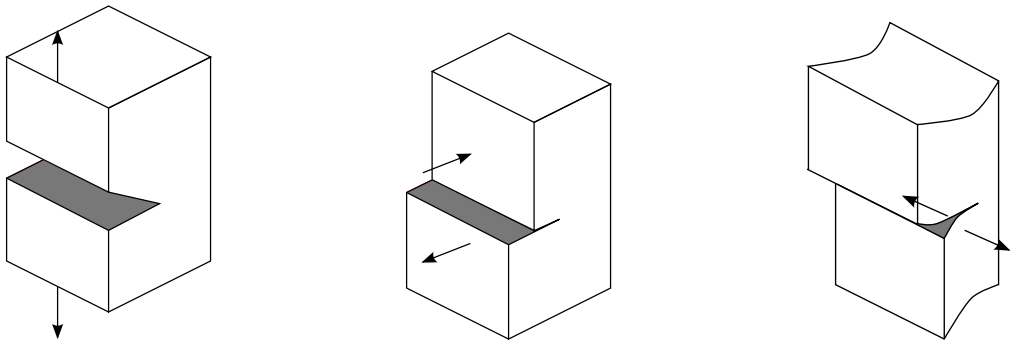

Figure 2.2: The three fracture modes: (a) mode I or opening mode, (b) mode II or sliding mode and (c) mode III or tearing mode.

A number of different approaches accounting for displacement discontinuities have been proposed in the literature, see for instance the pioneering works by Simo et al. (1993), Simo and Oliver (1994) and Armero and Garikipati (1996). These techniques allow a reliable simulation of failure processes, where macroscopic cracks arise. However, from a numerical point of view, a main difficulty appears. Indeed, standard finite element approximations cannot capture these strong discontinuities and thus, special techniques need to be used. Here, some of the existing computational methods to handle displacement discontinuities are briefly reviewed. For a more detailed overview, we refer to the review articles of Jirásek and Belytschko (2002) and Rabczuk (2013).

Remeshing. In remeshing methods, the standard FEM is used. Indeed, as long as the element faces (or edges in 2D) are aligned with the crack and the nodes located on these faces (or edges) are doubled, the standard finite element method can properly account for displacement discontinuities. However, due to the propagating nature of the crack, these requirements are only achieved if the finite element mesh

is reconstructed at each time crack propagates. Although some interesting remeshing techniques to model crack propagation can be found in the literature, see for instance Bouchard et al. (2000), their applicability is hampered by one main drawback. It requires repeatedly projecting variables of the initial mesh onto the new one, which is difficult and computationally inefficient.

Embedded discontinuities. Embedded discontinuity models, see Jirásek (2000) for a detailed review, enrich the approximation of the displacement field with additional parameters that allow to capture displacement jumps. This technique, inspired by the work of Ortiz et al. (1987) and Belytschko et al. (1988), is based on an elemental enrichment. That is, the additional unknowns needed to account for the displacement jumps are compacted at elemental level. Hence, small changes in finite element codes are needed. In contrast to the above-mentioned technique, discontinuities do not need to lie at element interfaces thus eliminating the need for continuous remeshing.

Extended Finite Element Method (X-FEM). In the past years, X-FEM, see Belytschko and Black (1999) and Moës et al. (1999), has become one of the most used techniques to simulate the presence of cracks in a finite element framework. The main idea of this approach, based on the partition of unity concept (Melenk and Babuška (1996), Babuška and Melenk (1997)), is to decompose the displacement field into a continuous part and a discontinuous part. In other words, the standard FE interpolation of the displacement field is enriched with discontinuous functions (chosen depending on the kind of information that needs to be incorporated into the solution), see Belytschko et al. (2009) and Fries and Belytschko (2010) for a detailed overview of this technique.

Although embedded discontinuities and X-FEM are quite similar methods —they are based on enrichment functions that are added to the standard finite element displacement field—, the former is based on an elemental enrichment while the latter on a nodal one. As discussed by Jirásek and Belytschko (2002), elements with embedded discontinuities present some limitations. Indeed, in spite of the displacement enrichment, the strain field on both sides of the crack is not fully uncoupled. Nevertheless, in a more recent comparison, Oliver et al. (2006) observe that the different kind of enrichment does not affect the accuracy of the representation of the discontinuity.

In this thesis, X-FEM is the technique used to introduce propagating cracks.

Apart from the above-mentioned strategies, there exist approaches of a different nature that can be used to model fracture. Among these techniques, *meshless methods* stand out. As pointed out first by Belytschko et al. (1996) and then by Nguyen et al. (2008), due to the absence of a mesh, *meshless methods* can be efficiently used to model evolving discontinuities. Another alternative approach to fracture consists of using *phase-field methods*, see the pioneering works by Francfort and Marigo (1998) and Bourdin et al. (2000), where the cracks are supposed to propagate along the minimum energy path.

2.4 Continuous-discontinuous failure models

Continuous-discontinuous models (see for instance Mazars and Pijaudier-Cabot (1996), Jirásek and Zimmermann (2001), Wells et al. (2002), Simone et al. (2003) and Comi et al. (2007)) emerged to achieve a better characterisation of the whole failure process. The basic idea of these integrated strategies is to combine continuous and discontinuous descriptions of failure. The former allow to describe the early stages of the failure process, between the undamaged state and macroscopic crack initiation. The latter allow to incorporate into the model discontinuous displacement fields. Their main features, shown in Figure 2.3, are summarised here:

- **Continuous regime**: in order to simulate the first stages of the failure process, non-local continuous models are used. Thus, as discussed in Section 2.2, the numerical difficulties, such as mesh dependence, exhibited by local failure descriptions are overcome.
- **Transition**: at the end of each time step, the approach checks if the transition criterion is fulfilled. In such a case, a discontinuity is introduced. Different critical issues need to be taken into account:
  - **Switching criterion**: the transition from a continuous to a discontinuous model is carried out when the damage (the strain or the stress) field reaches a critical damage (strain or stress) value. The definition of this critical value has consequences. Indeed, if the transition is triggered when the material is fully degraded, traction-free cracks can be introduced. Otherwise, cohesive cracks need to be inserted. In general, few attention is paid to this issue, although some attempts have been made to link this

critical value to the element size, see Comi et al. (2007), thus ensuring that the transition is triggered earlier if a coarser mesh is employed.

- **Crack-path definition**: the location and propagation of a crack in combined strategies is hampered by one main drawback. Since linear elastic fracture mechanics cannot be employed in a regularised bulk, the crack-path cannot be analytically derived. Hence, alternative criteria should be used. In fact, a few number of contributions address this issue and in general, the path of the propagating crack is assumed to be known beforehand.
- **Energy consistency**: in order to replace a damage zone by a crack, energetic considerations need to be accounted for. When switching models, the energy not yet dissipated by the bulk needs to be transferred to the cohesive crack. This idea, assumed in several of the exiting continuous-discontinuous techniques, needs to be further investigated. Indeed, two main shortcomings should be addressed. First, the computation of the remaining energy to be transferred to the cohesive interface is not straightforward without knowing the solution of a continuous reference model. Second, the extension to a multidimensional setting of the available techniques to estimate this quantity still needs to be improved.

• **Discontinuous regime**: once a crack is introduced, a discontinuous approach is used to model the final stages of the failure process. Due to the appealing properties that X-FEM offers, most existing combined approaches use this technique to deal with displacement discontinuities.

Different integrated strategies have already been proposed in the literature. Without attempting to be complete, in this section, some of these techniques are reviewed.

A first contribution of coupled models is given by Mazars and Pijaudier-Cabot (1996), where thermodynamic relationships between the two classical theories are presented. It is shown that it is possible to obtain the fracture energy from a non-local damage model and vice versa, a crack may be represented by a damage zone.

Jirásek and Zimmermann (2001) propose to describe failure phenomena combining smeared cracks —for the early stages of material degradation— with embedded discontinuities —for the stages where strain reaches a critical value. In other words, at the beginning of the failure process, the bulk is characterised by a non-local dam-

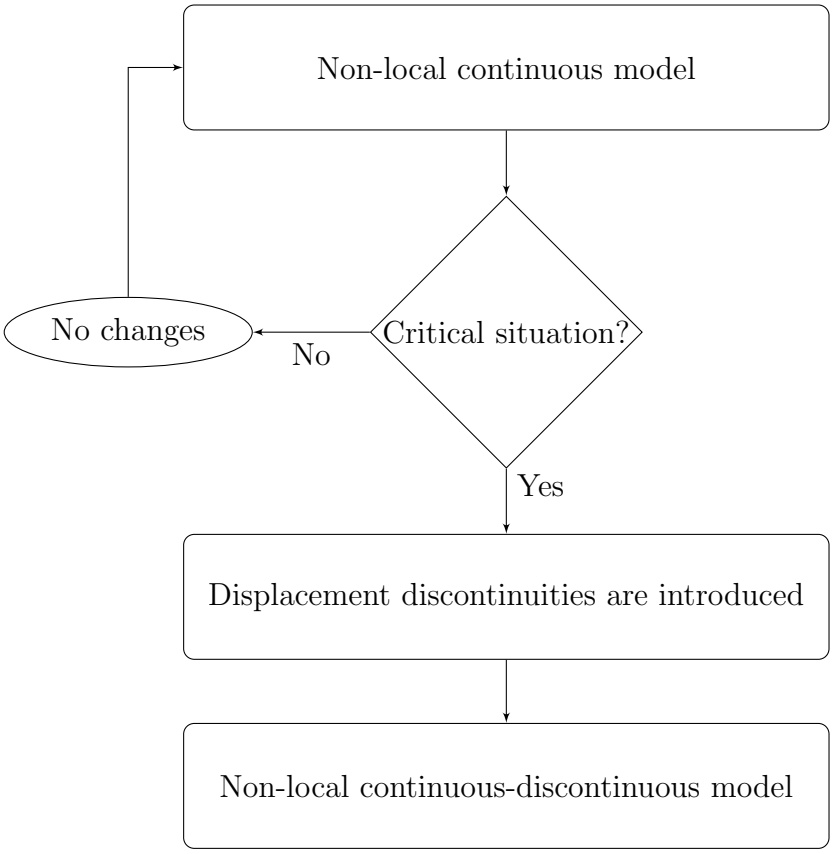

Figure 2.3: Scheme of a standard continuous-discontinuous model.

age model. Once a crack is introduced, the damage field is not allowed to increase and the bulk material is treated as linear elastic with the stiffness that corresponds to the secant unloading of the model.

In Wells et al. (2002), an additional improvement is achieved by using the partition of unity concept to couple a softening viscoplasticity model with traction-free discontinuities. Since the transition is driven at the later stages of the failure process, no energetic considerations need to be taken into account. A similar coupled continuous-discontinuous model is presented by Simone et al. (2003), where an implicit gradient-enhanced continuum damage model is combined with a traction-free crack that propagates following the direction of maximum accumulation of the non-local equivalent strain.

In order to avoid one of the shortcomings of these strategies, where the transition takes place when damage tends to one, an alternative coupled approach can

be employed, see Comi et al. (2007). The key idea is to define a critical damage value $D_{\text{crit}} < 1$ beyond which the transition is triggered. Then, an energetically equivalent cohesive crack is introduced. In order to compute its fracture energy, an energy balance is prescribed: the energy not yet dissipated by the continuous approach is transferred to the cohesive interface. Similar energetic assumptions are made by Cazes et al. (2009), when dealing with elastic-damage models, and Cazes et al. (2010), for damage-plasticity. Indeed, given a solution of a continuous reference model, an energetic equivalent cohesive law is incrementally built. In Seabra et al. (2011), an energetic balance is also prescribed to establish the crack surface in a coupled continuous-discontinuous model for ductile materials. Cuvilliez et al. (2012) also take into account these energetic considerations when proposing an alternative combined approach. Indeed, in order to simulate the first stages of a failure process, a gradient damage model, where the gradient of the damage field is used to regularise softening, is employed. As soon as damage reaches a critical value the switching to a cohesive crack —whose growth direction is known in advance— is carried out. In order to allow the transition to occur at early stages of values, an energy conservation between models is prescribed.

Another recent strategy is the regularised extended finite element approach (Re-XFEM) by Benvenuti and Tralli (2012). They propose to characterise the failure process by means of three different stages. In a first stage, a continuous damage model is used. Then, when damage achieves a critical value, this continuous model is switched to a regularised discontinuous approach (Re-XFEM). Finally, a purely discontinuous strategy, where the standard X-FEM is retrieved, is used. This approach overcomes some of the shortcomings of existing techniques such as the pathological mesh-dependence of local models and the energetic consistency at the transition. However, it is only used for problems where the crack path is known *a priori*.

In addition to the reviewed strategies, there exist approaches of a different nature where the importance of merging continuous and discontinuous formulations is also highlighted.

On the one hand, cracks can be introduced as a post-processing technique. Indeed, in Dufour et al. (2008) and Dufour et al. (2012), an integral non-local isotropic damage model is used to simulate the whole failure process. Then, using the global tracking algorithm proposed by Oliver and Huespe (2004), the crack path and the crack opening are computed as a post-process of the continuous numerical solution.

On the other hand, cracks can be easily located by means of the thick-level set (TLS) approach. This strategy, first presented by Moës et al. (2011) and improved by Bernard et al. (2012), considers damage as a function of a level set. Then, fully damaged zones play the role of macro-cracks thus leading to not necessarily zero-thickness discontinuities. Although it is a promising strategy to model the transition between damage and fracture, further research is needed in order to include, for instance, cohesive forces.

Chapter 3

Continuous damage model with smoothed displacements

In this chapter, the regularisation technique based on smoothed displacements is extended to a two- and three-dimensional setting. In this formulation, mechanical displacements $\boldsymbol{u}$ coexist with smoothed displacements $\widetilde{\boldsymbol{u}}$, which are the solution of a diffusion-reaction equation. Our main concern is to prescribe appropriate boundary conditions to the regularisation equation. More specifically, since usual boundary conditions —Dirichlet, homogeneous Neumann and non-homogeneous Neumann— do not allow neither to regularise softening if damage starts on the boundary nor to preserve volume, new conditions —combined conditions— are proposed. These satisfy the necessary properties for regularisation: (a) reproducibility of order 1 ($\widetilde{\boldsymbol{u}} = \boldsymbol{u}$ if $\boldsymbol{u}$ is an affine field) in order to ensure that a constant strain field leads to a constant stress, (b) displacement smoothing along the boundary and (c) volume preservation. Different two- and three-dimensional examples have been carried out to illustrate that smoothed displacements allow to preclude mesh dependence also in a multidimensional setting.

3.1 Introduction

Regularised damage models —integral- and gradient-type formulations— are able to overcome the well-known problems of standard approaches such as pathological

mesh dependence thus providing an objective description of the first stages of failure processes. The key idea of these formulations is to replace a certain variable by its non-local counterpart. Typically, the selected variable to introduce this non-locality is the internal state variable but a number of different proposals can be found in the literature, as reviewed by Jirásek (1998).

One of these alternative formulations consists of selecting the displacement field to incorporate non-locality, as presented and illustrated with a one-dimensional example by Rodríguez-Ferran et al. (2005). As discussed, this new formulation is very attractive from a computational viewpoint —especially regarding the computation of the consistent tangent matrix. Moreover, adding non-locality at the level of displacements —rather than some internal variable— has the advantage of not interfering with the constitutive driver.

In this chapter, we extend the applicability of this gradient-enriched formulation to a two- and three-dimensional setting. For the sake of simplicity, only elastic-scalar damage models are considered here. However, as discussed by Rodríguez-Ferran et al. (2011), smoothed displacements can be easily extended to other approaches such as plasticity models. Specifically, in this chapter we propose:

1. **To extend the applicability of this alternative formulation to a two- and three-dimensional setting**. We propose to analyse the regularisation capabilities of this new formulation by means of two- and three-dimensional problems. Different damage models and damage laws are analysed to illustrate that smoothed displacements are an efficient way to regularise softening.

2. **To prescribe new boundary conditions for the regularisation equation**. The advantage of using gradient-enriched formulations is that although they are non-local models, they are local from a mathematical viewpoint, since non-local interaction is accounted for by means of higher-order derivatives. Nevertheless, their main disadvantage arises from the requirement of additional boundary conditions. In Rodríguez-Ferran et al. (2005), Dirichlet boundary conditions are prescribed for the regularisation equation. Nevertheless, as discussed by Jirásek and Marfia (2006), they may have the negative effect of not allowing displacement smoothing along the boundary. Here, in order to overcome this difficulty, we propose to prescribe combined boundary conditions —Dirichlet boundary conditions for the normal component of the displacement field and

non-homogeneous Neumann boundary conditions for the tangential ones.

The structure of the chapter is as follows. In Section 3.2 the gradient version of the damage model based on smoothed displacements is briefly reviewed. Special emphasis is placed on the definition of the boundary conditions for the regularisation equation in Section 3.3. The regularisation capabilities are illustrated by means of some numerical examples in Section 3.4. Finally, the concluding remarks in Section 3.5 and the future directions in Section 3.6 close this chapter.

3.2 Gradient-enhanced damage model

In the implicit gradient-enhanced continuum model based on smoothed displacements, two different displacement fields coexist: (a) the standard or local displacement field $\boldsymbol{u}$ and (b) the gradient-enriched displacement field $\widetilde{\boldsymbol{u}}$, which is the solution of a partial differential equation with $\boldsymbol{u}$ as the source term. Analogously to the diffusion-reaction equation

$$\widetilde{Y}\left(\boldsymbol{x}\right) - \ell^2 \nabla^2 \widetilde{Y}\left(\boldsymbol{x}\right) = Y\left(\boldsymbol{x}\right) \tag{3.1}$$

used in standard gradient-enhanced damage models —where the state variable Y is selected to introduce non-locality and ℓ is the diffusion parameter with dimension of length— here the regularisation PDE is the diffusion-reaction equation

$$\widetilde{\boldsymbol{u}}\left(\boldsymbol{x}\right) - \ell^2 \nabla^2 \widetilde{\boldsymbol{u}}\left(\boldsymbol{x}\right) = \boldsymbol{u}\left(\boldsymbol{x}\right) \tag{3.2}$$

Hence, the key idea of this alternative formulation is to use this regularised displacement field to drive damage evolution, see Table 3.1 for details. It should be stressed that in Table 3.1, a strain-based model is considered. Indeed, the smoothed state variable depends on the smoothed strain tensor. However, smoothed displacements can also be used with stress-based damage models, as seen in Section 3.4.

3.3 Boundary conditions

In standard gradient-enriched formulations, boundary conditions for the non-local state variable $\widetilde{Y}$ are required, see Equation (3.1). Typically —we refer to the articles of

Table 3.1: Gradient-enhanced damage model based on smoothed displacements.

Constitutive equation	$\boldsymbol{\sigma} = (1 - D)\,\boldsymbol{C} : \boldsymbol{\varepsilon}$
Strains	$\boldsymbol{\varepsilon} = \nabla^s \boldsymbol{u}$
Smoothed displacements	$\widetilde{\boldsymbol{u}} - \ell^2 \nabla^2 \widetilde{\boldsymbol{u}} = \boldsymbol{u}$
Smoothed strains	$\widetilde{\boldsymbol{\varepsilon}} = \nabla^s \widetilde{\boldsymbol{u}}$
Smoothed state variable	$\widetilde{Y} = Y\left(\widetilde{\boldsymbol{\varepsilon}}\right)$
Damage evolution	$D = D(\widetilde{Y})$

Peerlings et al. (1998) and Peerlings et al. (2001)—, homogeneous Neumann boundary conditions

$$\nabla \widetilde{Y} \cdot \boldsymbol{n} = 0 \quad \text{on } \partial\Omega \tag{3.3}$$

are prescribed, where $\boldsymbol{n}$ denotes the outward unit normal to Ω.

The main reason for prescribing conditions (3.3) is the difficulty to specify a value of $\widetilde{Y}$ on the boundary. Indeed, due to the internal nature of the non-local state variable, fixing $\widetilde{Y}$ itself —that is, prescribing Dirichlet boundary conditions— seems to be difficult to motivate on physical basis. It is noted here that homogeneous Neumann boundary conditions are suggested also by Mühlhaus and Alfantis (1991) when dealing with plasticity models.

From a physical point of view, these conditions have been widely debated. As discussed by Polizzotto (2003), boundary conditions (3.3) guarantee that regularisation effects do not propagate through the boundary of the domain (insulation condition). Finally, in Benvenuti et al. (2004), these conditions are not prescribed *a priori* but they are obtained by means of a standard variational analysis.

Regarding the alternative formulation based on smoothed displacements, boundary conditions for the smoothed displacement field $\widetilde{\boldsymbol{u}}$ must be imposed. Prescribing boundary conditions at the level of displacements (rather than the internal variable $\widetilde{Y}$) seems easier to interpret. A natural option is to prescribe Dirichlet boundary conditions

$$\widetilde{\boldsymbol{u}} = \boldsymbol{u} \quad \text{on} \quad \partial\Omega \tag{3.4}$$

that have a clear physical interpretation: local and non-local displacements coincide along all the domain boundary. That is, the material response remains local at the boundary of the solid. This property guarantees one important requirement: as pointed out by Krayani et al. (2009) and Pijaudier-Cabot and Dufour (2010), non-locality should vanish at the boundary in its normal direction. As illustrated by Rodríguez-Ferran et al. (2005), these conditions can be effectively used to obtain physically realistic results in a one-dimensional setting. However, as discussed by Jirásek and Marfia (2006), this may have the negative effect of not allowing displacement smoothing along the boundary, since $\widetilde{\boldsymbol{u}}$ and $\boldsymbol{u}$ are imposed to be equal on $\partial\Omega$. Such effect, especially negative in problems where localisation starts at the boundary, does not allow a correct widening of the damage zone.

In order to avoid this unwanted behaviour and analogously to the standard gradient model, see Equation (3.3), homogeneous Neumann boundary conditions

$$\nabla\widetilde{\boldsymbol{u}} \cdot \boldsymbol{n} = \boldsymbol{0} \quad \text{on } \partial\Omega \tag{3.5}$$

may be imposed. Note that by means of these conditions, smoothed displacements $\widetilde{\boldsymbol{u}}$ do not need to be equal to $\boldsymbol{u}$ along all the boundary thus overcoming the main drawback of conditions (3.4).

Nevertheless, these alternative conditions do not guarantee neither the locality of the solution along the normal direction at the boundary nor another important requirement: reproducibility of order 1. In standard gradient-enriched models, reproducibility of constant functions must be ensured: given a constant local state variable Y, $\widetilde{Y} \equiv Y$ has to be solution of the regularisation equation (3.1) thus implying that given a constant strain field $\boldsymbol{\varepsilon}$, the stress field

$$\boldsymbol{\sigma}\left(\boldsymbol{x}\right) = \left(1 - D(\widetilde{Y})\right)\boldsymbol{C} : \varepsilon\left(\boldsymbol{x}\right) = \left(1 - D\left(Y\right)\right)\boldsymbol{C} : \varepsilon\left(\boldsymbol{x}\right) \tag{3.6}$$

is also constant. Hence, and taking into account that $\boldsymbol{\varepsilon} = \nabla^s\boldsymbol{u}$, reproducibility of order 1 should be ensured: given an affine displacement field $\boldsymbol{u}$, $\widetilde{\boldsymbol{u}} = \boldsymbol{u}$ has to be solution of the regularisation equation (3.2).

Note that if homogeneous Neumann boundary conditions (3.5) are prescribed, this is not guaranteed. Indeed, let us assume an affine vector field

$$\boldsymbol{u}(\boldsymbol{x}) = \boldsymbol{a} + \boldsymbol{B}\boldsymbol{x} \tag{3.7}$$

where $\boldsymbol{x} = (x_1, \ldots, x_{\text{nsd}})^T$, $\boldsymbol{a} = (a_1, \ldots, a_{\text{nsd}})^T$ (where nsd denotes the number of space dimensions) and $\boldsymbol{B}$ is a matrix. Then, the affine displacement field

$$\widetilde{\boldsymbol{u}}(\boldsymbol{x}) = \boldsymbol{a} + \boldsymbol{B}\boldsymbol{x} \tag{3.8}$$

is not the solution of the boundary problem consisting of equation (3.2) and conditions (3.5), since the constraint

$$\nabla\widetilde{\boldsymbol{u}} \cdot \boldsymbol{n} = \boldsymbol{B} \cdot \boldsymbol{n} = \boldsymbol{0} \tag{3.9}$$

is not satisfied $\forall \boldsymbol{B}$.

As suggested by the above discussion and in order to solve these difficulties — smoothed displacement along the domain boundary and reproducibility of order 1—, alternative boundary conditions should be prescribed. In Jirásek and Marfia (2006), non-homogeneous Neumann boundary conditions

$$\nabla\widetilde{\boldsymbol{u}} \cdot \boldsymbol{n} = \nabla\boldsymbol{u} \cdot \boldsymbol{n} \quad \text{on } \partial\Omega \tag{3.10}$$

are proposed. Nevertheless, if these new conditions are prescribed, non-locality does not vanish along the normal direction at the boundary of the solid. Moreover, they pose another drawback: volume conservation is not ensured. Indeed, let us suppose constant density and use the divergence theorem. Then,

$$0 = \int_\Omega \nabla \cdot (\widetilde{\boldsymbol{u}} - \boldsymbol{u}) \, \mathrm{d}\Omega = \int_{\partial\Omega} (\widetilde{\boldsymbol{u}} - \boldsymbol{u}) \cdot \boldsymbol{n} \, \mathrm{d}\Gamma \tag{3.11}$$

that is satisfied with Dirichlet boundary conditions (since $\boldsymbol{u}$ and $\widetilde{\boldsymbol{u}}$ are equal along all the boundary) but is not guaranteed with homogeneous or non-homogeneous Neumann boundary conditions.

Note that preservation of volume may be interesting in some constitutive models. For example, let us assume that the regularised plasticity model presented in Rodríguez-Ferran et al. (2011) is used. Then, given isochoric local strains ($\nabla \cdot \boldsymbol{u} = 0$), isochoric non-local strains ($\nabla \cdot \widetilde{\boldsymbol{u}} = 0$) are obtained if preservation of volume is prescribed.

As an alternative to equations (3.4), (3.5) or (3.10) we propose here to use combined boundary conditions. That is, to prescribe Dirichlet boundary conditions for the normal component of the displacement field whereas non-homogeneous Neumann boundary conditions are imposed for the tangential components

$$\left.\begin{array}{rcl} \widetilde{\boldsymbol{u}} \cdot \boldsymbol{n} & = & \boldsymbol{u} \cdot \boldsymbol{n} \\ \nabla(\widetilde{\boldsymbol{u}} \cdot \boldsymbol{t}_1) \cdot \boldsymbol{n} & = & \nabla(\boldsymbol{u} \cdot \boldsymbol{t}_1) \cdot \boldsymbol{n} \\ \nabla(\widetilde{\boldsymbol{u}} \cdot \boldsymbol{t}_2) \cdot \boldsymbol{n} & = & \nabla(\boldsymbol{u} \cdot \boldsymbol{t}_2) \cdot \boldsymbol{n} \end{array}\right\} \text{on } \partial\Omega \tag{3.12}$$

where $\boldsymbol{n}$ denotes the outward unit normal to Ω and $\boldsymbol{t}_1$, $\boldsymbol{t}_2$ are tangent vectors such that $\{\boldsymbol{n}, \boldsymbol{t}_1, \boldsymbol{t}_2\}$ form an orthonormal basis for $\mathbb{R}^3$.

Note that by means of the boundary condition $(3.12)_1$, the material response remains local along the normal direction at the boundary of the solid and preservation of volume is ensured, whereas with conditions $(3.12)_2$ and $(3.12)_3$, some relative slip between local and non-local displacements is allowed. Moreover, reproducibility of order 1 is guaranteed by means of these conditions, see Table 3.2 for a summary.

Table 3.2: Summary table: boundary conditions and their properties.

	Dirichlet	Homogeneous Neumann	Non-homogeneous Neumann	Combined
Reproducibility of order 1	✓	×	✓	✓
Displacement smoothing along the boundary	×	✓	✓	✓
Local response normal to boundaries	✓	×	×	✓
Volume preservation	✓	×	×	✓

It is worth pointing out here that the resolution of the vector equation (3.2) is equivalent to solving a scalar equation for each component of the vector field separately only if the boundary conditions keep them uncoupled. This occurs if boundary conditions (3.4), (3.5) or (3.10) are prescribed. Nevertheless, combined boundary conditions (3.12) keep the components of the vector field uncoupled only in the case where the boundary is parallel to the Cartesian planes. It must be stressed that this coupling has no critical consequences. On the one hand, the components of the vector field $\boldsymbol{u}$ are already coupled due to the equilibrium equation. On the other hand, assuming the boundaries of the structure parallel to the Cartesian planes is not very restrictive. Indeed, a wide range of examples with this property have been carried out, see Section 3.4.

To illustrate the above discussion, the regularisation equation (3.2) defined on the two-dimensional domain $\Omega = [0,1] \times [0,1]$ —where $\boldsymbol{u} = (u_x, u_y)$ and $\widetilde{\boldsymbol{u}} = (\widetilde{u}_x, \widetilde{u}_y)$— and two different source terms $\boldsymbol{u}$ are considered. For the sake of simplicity, let us

consider

$$u := u_x = u_y \tag{3.13}$$

As a first test, the diffusion-reaction equation (3.2) is solved considering an affine source term u, see Figure 3.1(a). On the one hand, as seen in Figure 3.1, given an affine function u, solutions $\widetilde{u} = u$ are admitted if Dirichlet, non-homogeneous Neumann or combined boundary conditions are prescribed. On the other hand, if homogeneous Neumann boundary conditions are used, a solution $\widetilde{\boldsymbol{u}} \neq (u, u)$ is obtained, see Figure 3.1(c) thus leading to the following problem from a mechanical point of view: given a constant strain field $\boldsymbol{\varepsilon}(\boldsymbol{x})$, a non-constant stress field $\boldsymbol{\sigma}(\boldsymbol{x})$ is obtained, see Table 3.1.

As a second test, the source term shown in Figure 3.2(a) is analysed. As seen in Figure 3.2(b), Dirichlet boundary conditions do not allow a relative slip along the boundary. However, this is permitted if Neumann boundary conditions are employed, see Figures 3.2(c) and 3.2(d). By means of combined boundary conditions, the fields $\widetilde{u}_x$ and $\widetilde{u}_y$ of Figures 3.2(e) and 3.2(f) are obtained. Note that the field $\widetilde{u}_y$ is not smoothed along the boundary. Nevertheless, the displacement field $\widetilde{u}_x$, the relevant one for examples of mode I —see Section 3.4—, is smoothed along the boundary $\{y = 0\} \cup \{y = 1\}$.

3.4 Numerical examples

In this section we present some numerical examples to illustrate the capabilities of the new method. On the one hand, in Section 3.4.1, the influence of the above discussed boundary conditions is analysed. On the other hand, in Section 3.4.2, the regularisation capabilities of the new model with combined boundary conditions are illustrated.

3.4.1 Validation of the boundary conditions

The objective of this first section is to illustrate the influence of the above discussed boundary conditions. To this end, different two- and three-dimensional benchmark tests are carried out. For each of them, the four proposed boundary conditions are considered.

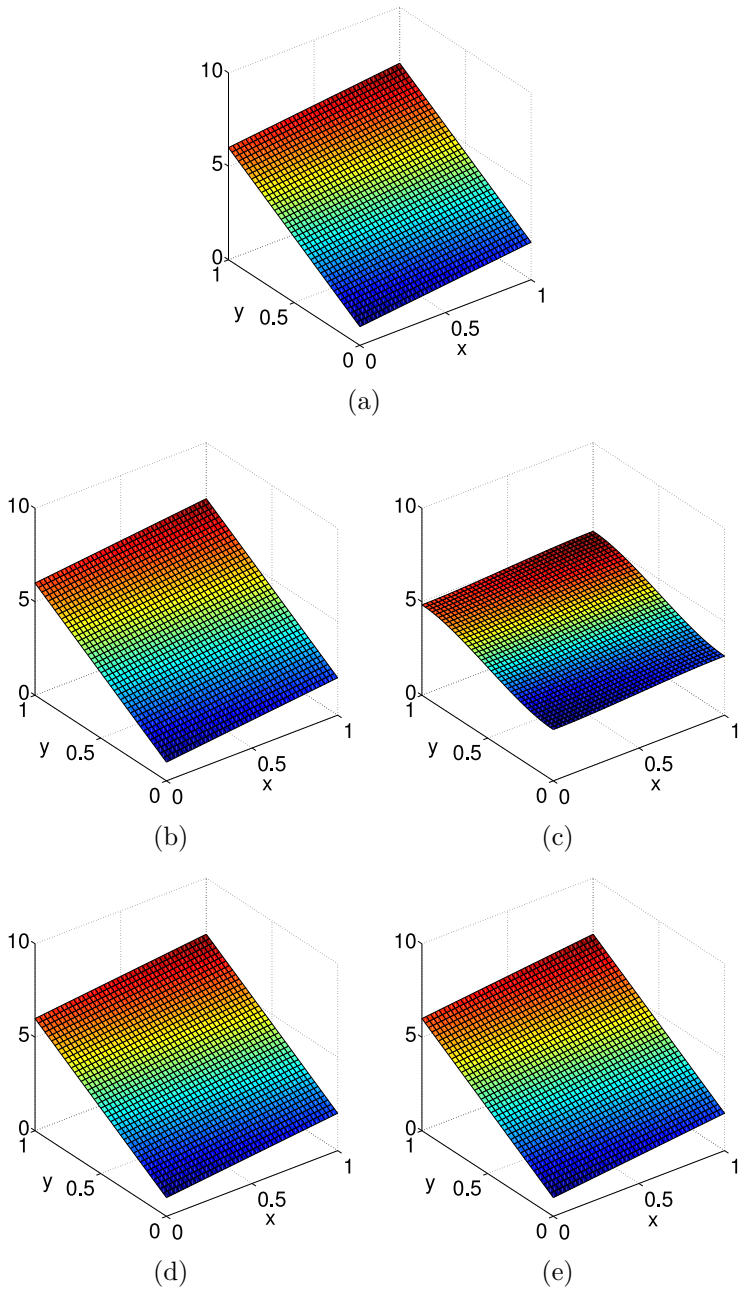

Figure 3.1: Validation test with (a) an affine source term $u(\boldsymbol{x}) = u(x, y) = 1 + x + 5y$. $\widetilde{u}$ solutions, where $\widetilde{\boldsymbol{u}} = (\widetilde{u}, \widetilde{u})$, obtained with (b) Dirichlet, (c) homogeneous Neumann, (d) non-homogeneous Neumann and (e) combined boundary conditions.

Uniaxial tension test. As a first example, a uniaxial tension test is carried out. In order to trigger localisation, the central part of the specimen is weakened (10% reduction in Young's modulus), see Figure 3.3.

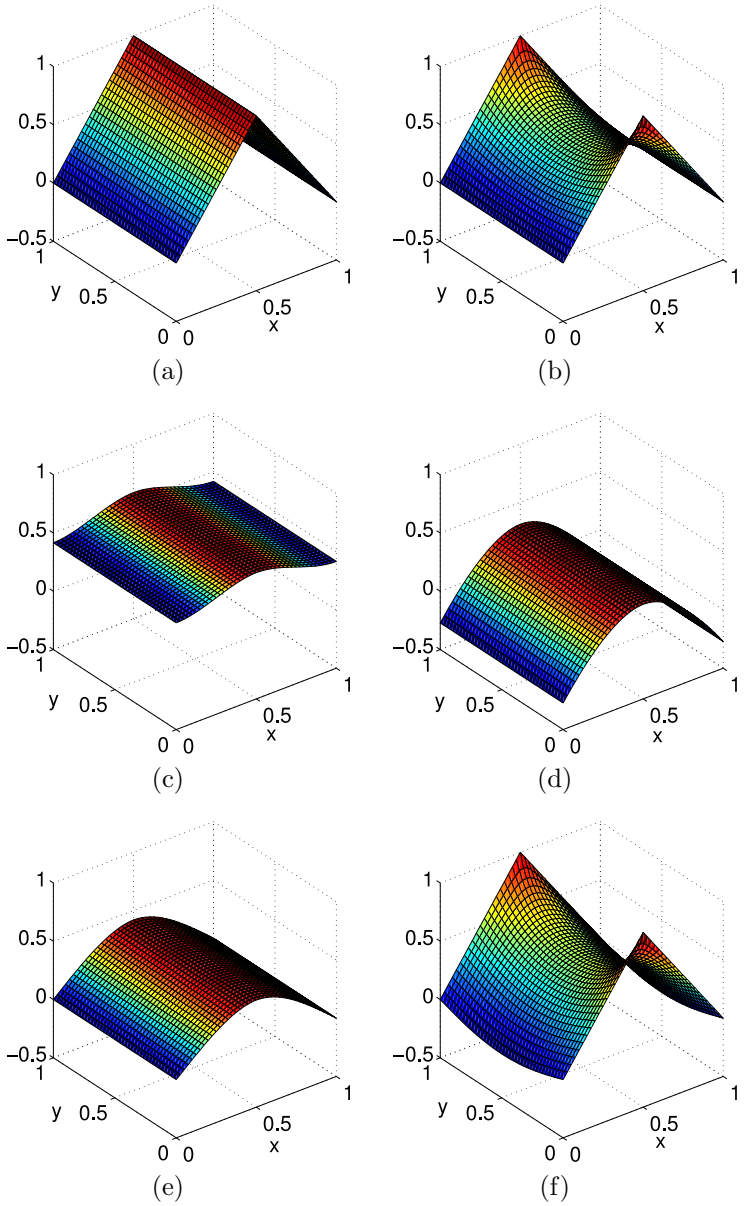

Figure 3.2: Validation test with (a) a *tent* function source term $u(\boldsymbol{x})$. Solutions obtained with (b) Dirichlet ($\widetilde{u}_x = \widetilde{u}_y$), (c) homogeneous Neumann ($\widetilde{u}_x = \widetilde{u}_y$), (d) non-homogeneous Neumann ($\widetilde{u}_x = \widetilde{u}_y$), (e) combined ($\widetilde{u}_x$) and (f) combined ($\widetilde{u}_y$) boundary conditions.

The geometric and material parameters are summarised in Table 3.3. The sim-

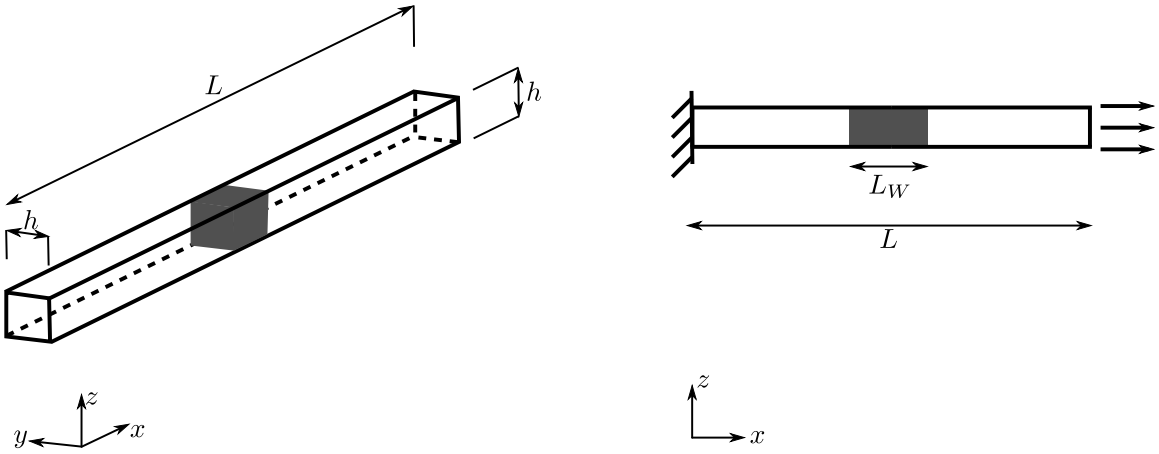

Figure 3.3: Uniaxial tension test: problem statement. Displacements are restrained at the left whereas displacements along the x axis are prescribed at the right. A weakened region (dark grey) is considered to trigger localisation.

plified Mazars model (Mazars, 1986)

$$Y = \sqrt{\sum_{i=1}^{3} \left(\max(0, \varepsilon_i)\right)^2} \tag{3.14}$$

with ε_i $(i = 1, 2, 3)$ the principal strains is considered. A linear damage evolution law

$$D(Y) = \begin{cases} 0 & \text{if } Y < Y_0 \\ \frac{Y_f}{Y_f - Y_0}\left(1 - \frac{Y_0}{Y}\right) & \text{if } Y_0 < Y < Y_f \\ 1 & \text{if } Y_f < Y \end{cases} \tag{3.15}$$

with Y_0 the damage initiation state variable and Y_f the final state variable is used. Note that the Poisson's coefficient is set to $\nu = 0$ in order to reproduce a purely one-dimensional problem. A calculation with a uniform mesh of 10 000 $(100 \times 10 \times 10)$ eight-noded hexahedral elements is carried out.

The results are summarised in Figure 3.4. On the one hand, Dirichlet boundary conditions lead to an underestimation of the dissipated energy through the failure process. This behaviour was already observed by Tamayo-Mas and Rodríguez-Ferran (2012) with the two-dimensional model and is due to the fact that essential conditions do not allow to obtain smoothed displacements along the boundary. On the other hand, as seen in Figure 3.4(b) and Figure 3.5, Dirichlet boundary conditions lead to a lack of a one-dimensional behaviour, since they do not allow the damage zone to be widened.

Table 3.3: Uniaxial tension test: geometrical and material parameters.

Meaning	**Symbol**	**Value**
Length of the beam	L	100 mm
Length of the weaker part	L_W	20 mm
Depth and height of the beam	h	10 mm
Young's modulus	E	20 000 MPa
Young's modulus of the weaker part	E_W	18 000 MPa
Damage initiation state variable	Y_0	10^{-4}
Final state variable	Y_f	1.25×10^{-2}
Poisson's ratio	ν	0.00

Note that due to the simplicity of the test, no differences are observed by means of the other boundary conditions. Indeed, if Neumann (both homogeneous and non-homogeneous) or combined boundary conditions are prescribed, the expected one-dimensional behaviour is observed, see Figures 3.4(a) and 3.4(c)-3.4(e) and Rodríguez-Ferran et al. (2005).

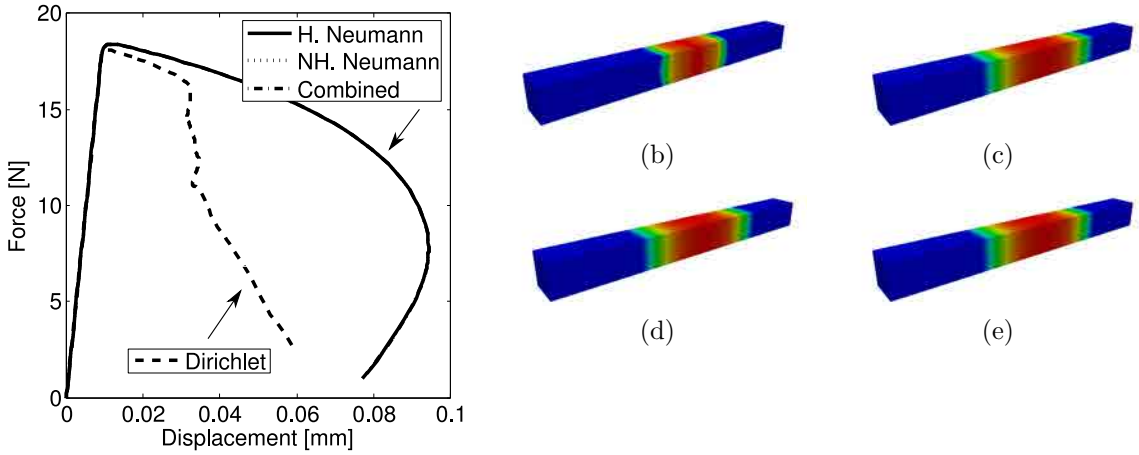

(a)

Figure 3.4: Uniaxial tension test: (a) force-displacement curves obtained with the four analysed boundary conditions and damage profiles obtained with (b) Dirichlet, (c) homogeneous Neumann, (d) non-homogeneous Neumann and (e) combined boundary conditions.

Three-point bending test. The second example concerns the simulation of a three-point bending test in a three-dimensional setting, see Figure 3.6.

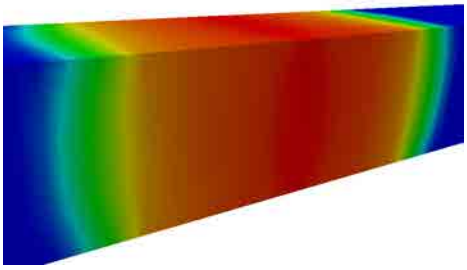

Figure 3.5: Close-up of the final damage distribution if Dirichlet boundary conditions are prescribed for the regularisation equation.

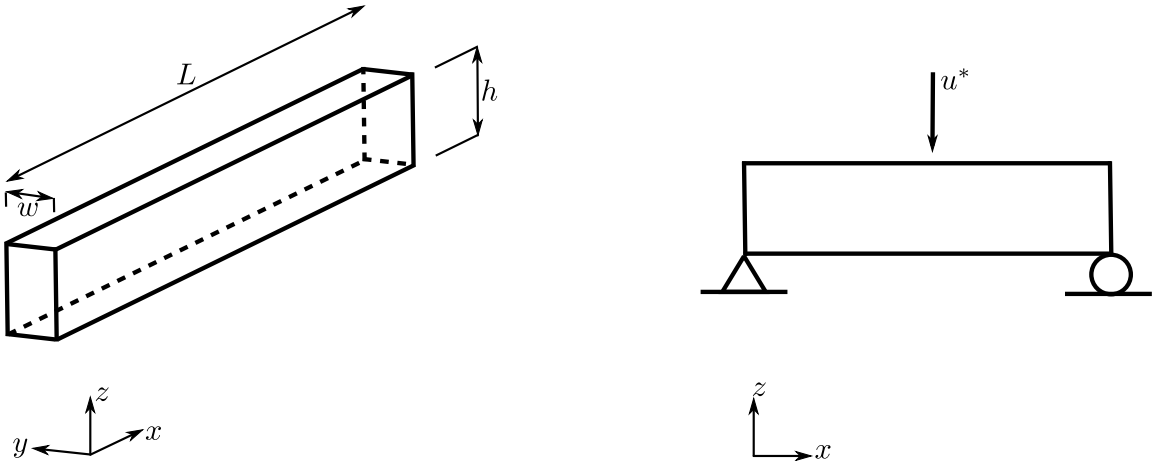

Figure 3.6: Three-point bending test: problem statement.

The geometric and material parameters are summarised in Table 3.4. Here, the truncated Rankine damage model

$$\tau = \sum_{i=1}^{3} \max(0, \tau_i) \tag{3.16}$$

with τ_i $(i = 1, 2, 3)$ the principal effective stresses and an exponential damage evolution law

$$D(\tau) = 1 - \frac{\tau_0}{\tau} \exp\Big(-\beta(\tau - \tau_0)\Big) \tag{3.17}$$

are considered. The calculation is carried out using a uniform mesh of 8 064 ($63 \times 8 \times 16$) eight-noded hexahedral elements.

The results are summarised in Figure 3.7. On the one hand, prescribing that mechanical and smoothed displacements must be equal all along the boundary (that is, prescribing Dirichlet boundary conditions) can be very restrictive, especially if

Table 3.4: Three-point bending test: geometrical and material parameters.

Meaning	**Symbol**	**Value**
Length of the beam	L	256 mm
Depth of the beam	w	32 mm
Height of the beam	h	64 mm
Young's modulus	E	30 000 MPa
Damage initiation equivalent effective stress	τ_0	3 MPa
Slope of the stress-strain relation	β	1.67×10^{-3} MPa^{-1}
Poisson's ratio	ν	0.00

damage starts on the boundary. As also observed in the previous example, this may lead to an underestimation of the dissipated energy, see Figure 3.7(a). On the other hand, as seen in Figure 3.7(c), if homogeneous Neumann boundary conditions are prescribed, the boundary is pathologically damaged. This behaviour is due to the fact that reproducibility of order 1 is not ensured and was already observed in two-dimensional examples, as discussed by Tamayo-Mas and Rodríguez-Ferran (2012).

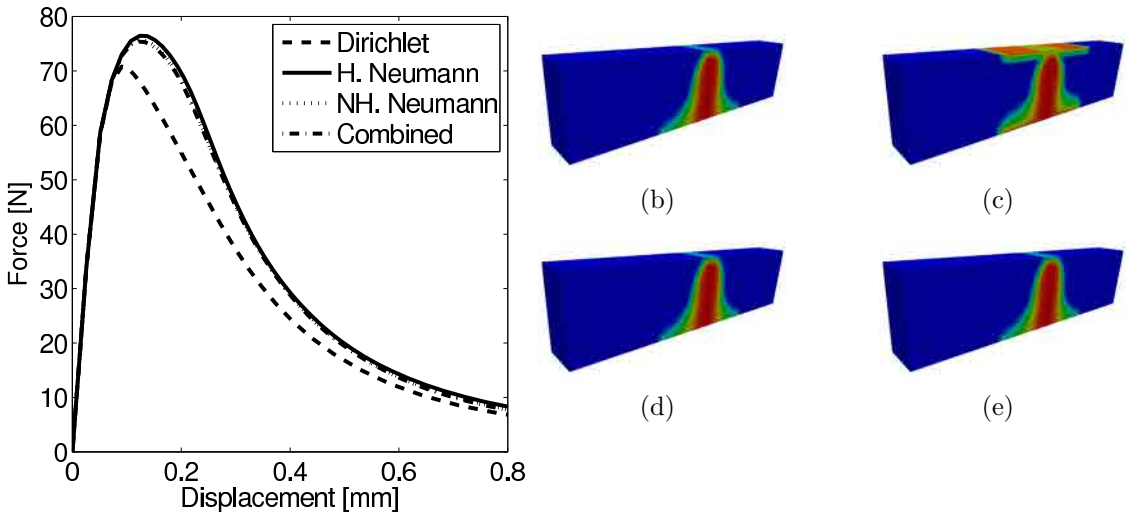

Figure 3.7: Three-point bending test: (a) force-displacement curves obtained with the four analysed boundary conditions and damage profiles obtained with (b) Dirichlet, (c) homogeneous Neumann, (d) non-homogeneous Neumann and (e) combined boundary conditions.

Square plate under mode I loading conditions. The third example concerns the simulation of a pure mode I problem in a two-dimensional setting. It deals with the solution of a square plate in tension subjected to a prescribed displacement at the top and bottom side and clamped at the right one, see Figure 3.8. In order to cause localisation, a weakened region is considered.

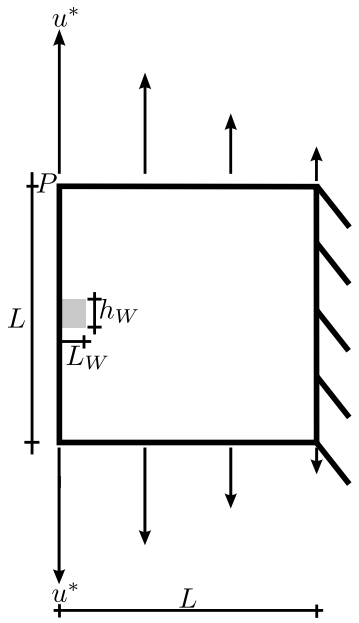

Figure 3.8: Square plate under mode I loading conditions: problem statement.

The geometric and material parameters are summarised in Table 3.5. Here, the simplified Mazars model, Equation (3.14), and a linear damage evolution law, Equation (3.15), are considered. The calculation is carried out using a uniform mesh of 1 640 (41×40) bilinear quadrilateral elements.

The results are shown in Figure 3.9. On the one hand, since the mechanical response at the top of the specimen strongly depends on the prescribed displacements, small differences are observed between the different force-displacement curves, see Figure 3.9(a). On the other hand, if reproducibility of order 1 is not ensured, the boundary is pathologically damaged, see Figure 3.9(c).

3.4.2 Validation of the regularisation capabilities

The objective of this section is to illustrate the regularisation capabilities of the proposed method. To this end, different two- and three-dimensional examples are

Table 3.5: Square plate under mode I loading conditions: geometrical and material parameters.

Meaning	**Symbol**	**Value**
Length of the plate	L	10 cm
Length of the weaker part	L_W	1 cm
Width of the weaker part	h_W	1 finite element
Young's modulus	E	20 000 MPa
Young's modulus of the weaker part	E_W	2 000 MPa
Damage threshold	Y_0	10^{-4}
Final strain	Y_f	1.25×10^{-2}
Poisson's ratio	ν	0.3

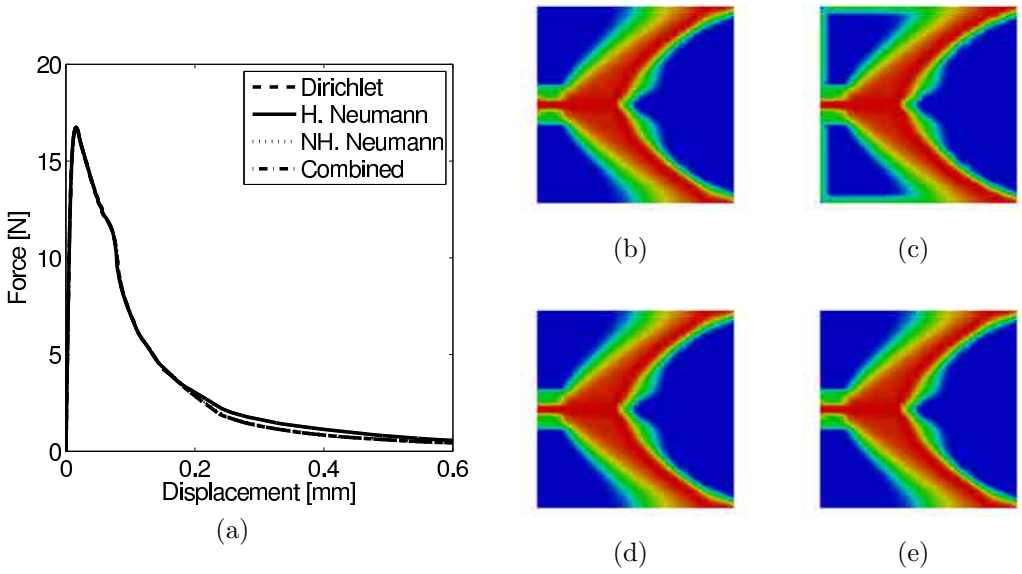

Figure 3.9: Square plate under mode I loading conditions: (a) force-displacement curves obtained with the four analysed boundary conditions and damage profiles obtained with (b) Dirichlet, (c) homogeneous Neumann, (d) non-homogeneous Neumann and (e) combined boundary conditions.

carried out by means of smoothed displacements with combined boundary conditions, see Equation (3.12).

Square plate under mode I loading conditions. As a first example, the two-

dimensional square plate analysed in Section 3.4.1 is retrieved, see Figure 3.8. The regularisation properties of the model are assessed by carrying out the analysis with four different meshes of 20×21, 30×31, 40×41 and 50×51 elements, see Figure 3.10.

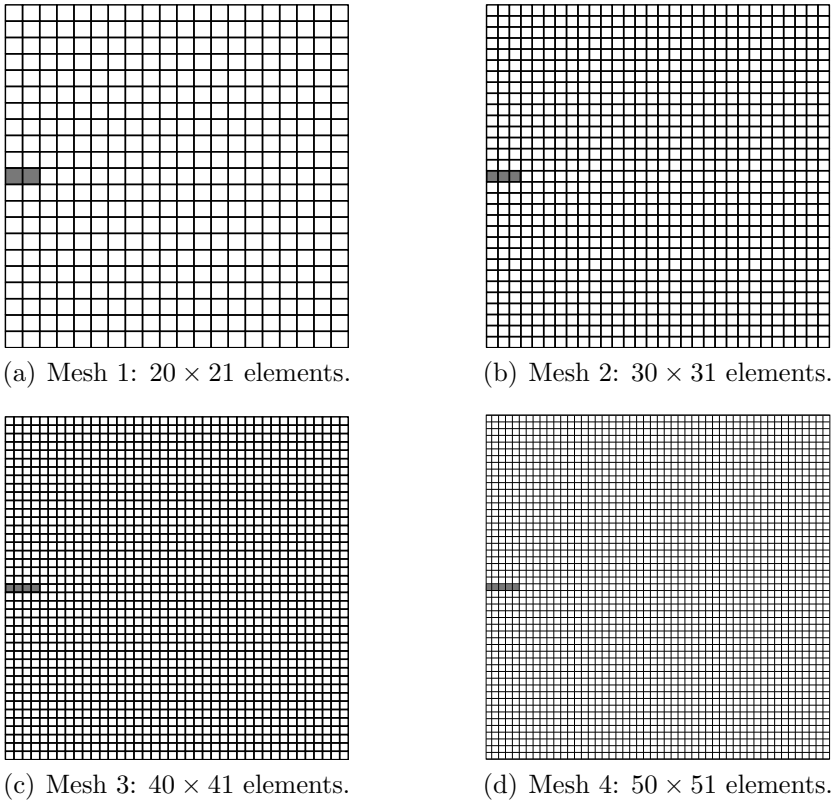

(a) Mesh 1: 20×21 elements.

(b) Mesh 2: 30×31 elements.

(c) Mesh 3: 40×41 elements.

(d) Mesh 4: 50×51 elements.

Figure 3.10: Square plate under mode I loading conditions. Four meshes with different element density and different imperfection sizes are used.

The damage profiles and the force-displacement curves are shown in Figure 3.11. As seen, the force-displacement curve and the width of damage band do not depend on numerical parameters such as the finite element mesh or the imperfection size needed to cause localisation.

Single-edge notched beam. As a second example, a single-edge notched beam subjected to an antisymmetrical four-point loading is considered, see Rodríguez-Ferran and Huerta (2000). Here, the three-dimensional domain is taken into account, see Figure 3.12. The material parameters are summarised in Table 3.6.

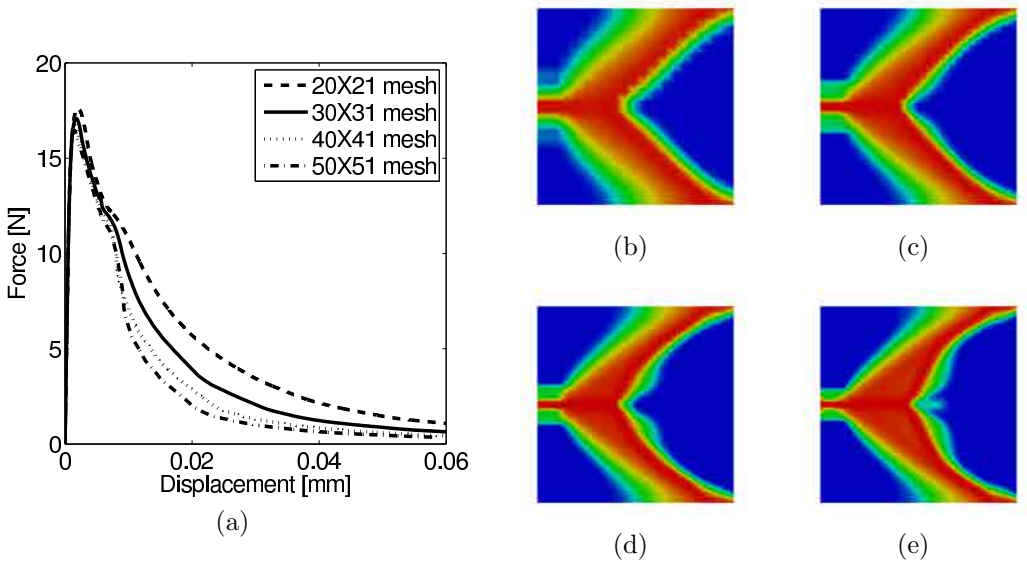

Figure 3.11: Square plate under mode I loading conditions: (a) force-displacement curves obtained with the four meshes and damage profiles obtained by means of the mesh of (b) 20×21 elements, (c) 30×31 elements, (d) 40×41 elements and (e) 50×51 elements.

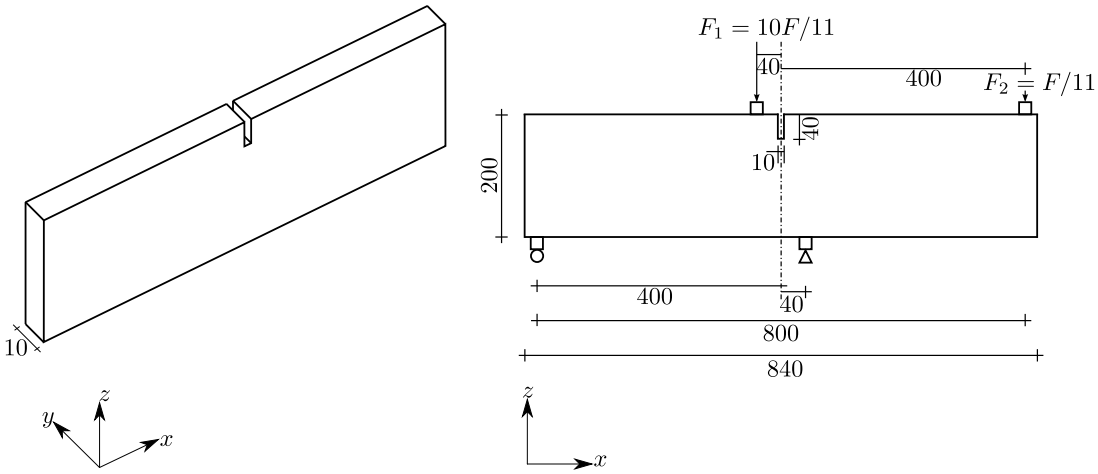

Figure 3.12: Single-edge notched beam: problem statement (measures in millimetres).

To carry out this test, the modified von Mises model, see de Vree et al. (1995),

$$Y = \frac{k-1}{2k\,(1-2\nu)} I_1 + \frac{1}{2k}\sqrt{\left(\frac{k-1}{1-2\nu} I_1\right)^2 + \frac{12k}{(1+\nu)^2} J_2} \tag{3.18}$$

is considered, where k is the ratio of compressive strength to tensile strength, ν is the

Table 3.6: Single-edge notched beam: geometrical and material parameters.

Meaning	**Symbol**	**Concrete**	**Steel**
Young's modulus	E	28 000 MPa	280 000 MPa
Poisson's ratio	ν	0.1	0.2
Compressive-to-tensile strength ratio	k	10	10
Damage threshold	Y_0	1.5×10^{-4}	
Residual strength	A	0.8	
Slope of the soft. branch at peak	B	9 000	

Poisson's coefficient, I_1 is the first invariant of the strain tensor and J_2 is the second invariant of the deviatoric strain tensor.

Thus, the exponential damage evolution

$$D = 1 - \frac{Y_0\,(1-A)}{Y} - A \exp\Big(-B\,(Y - Y_0)\Big) \tag{3.19}$$

is considered.

The regularisation properties of the model are assessed by carrying out the analysis with a fixed characteristic length $\ell = 2\sqrt{10}$ mm and three different meshes. The results are shown in Figure 3.13. As seen, neither the force-displacement curve nor the width of damage profiles depend on the finite element mesh.

Three-point reinforced prestressed bending beam. As a third example, the doubly notched reinforced prestressed beam subjected to three-point bending analysed in Cervera et al. (2011) is reproduced, see Figure 3.14.

The goal of this last example is to show the influence of the internal length scale ℓ. To this end, an analysis with a fixed finite element mesh and three different characteristic lengths —$\ell = 0.1$ cm, $\ell = 0.2$ cm and $\ell = 0.5$ cm— is carried out. In view of symmetry, only one half of the specimen —its right half— has been discretised. The material parameters both for the web and the reinforcement are summarised in Table 3.7.

The truncated Rankine damage model, Equation (3.16) with an exponential damage evolution law, Equation (3.17), are considered for the beam web, whereas the flanges are assumed elastic. The damage profiles and the force-displacement curves

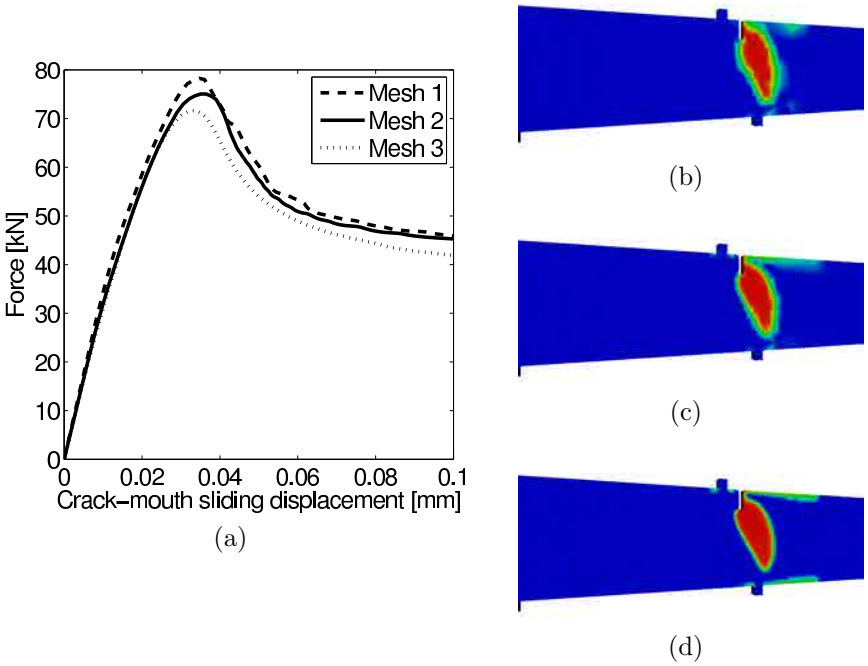

Figure 3.13: Single-edge notched beam: (a) force-displacement curves obtained with the three meshes and damage profiles obtained by means of the mesh with (b) 1 221 elements, (c) 2 289 elements and (d) 8 991 elements.

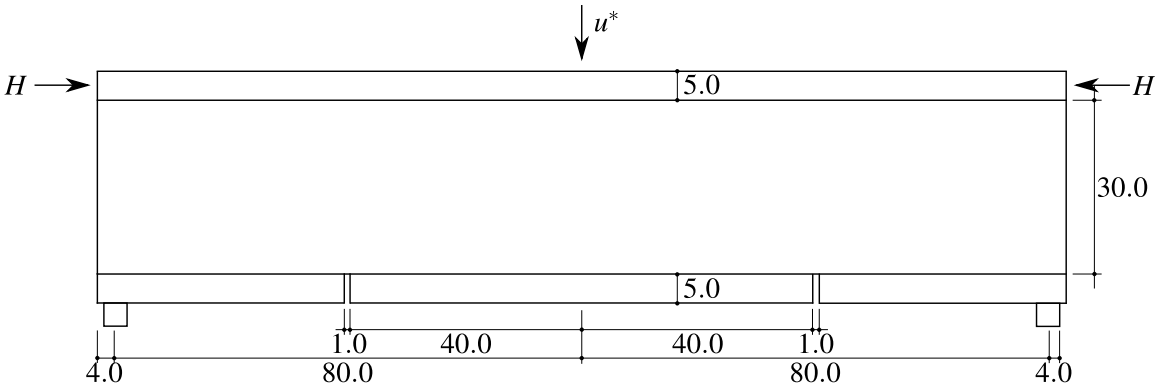

Figure 3.14: Three-point reinforced prestressed bending beam: problem statement (measures in centimetres).

are shown in Figure 3.15. As seen, both the ductility in the force-displacement response and the width of the final damage profile increase with the internal length scale.

For comparison purposes, the standard gradient-enhanced damage model, see

Table 3.7: Three-point reinforced prestressed bending beam: material parameters.

Meaning	**Symbol**	**Value**
Young's modulus of the web	E	30 GPa
Young's modulus of the reinforcement	E_r	200 GPa
Horizontal prestressing load	H	50 kN
Damage threshold	τ_0	3 MPa
Slope of the stress-strain relation	β	1.22×10^{-2} MPa^{-1}
Poisson's ratio of the web	ν	0.0
Fracture energy of the web	G	25 J/m^2

Equation (3.3), has also been implemented. The same analysis —with the same finite element mesh and the same characteristic lengths— is carried out. As shown in Figure 3.15, the results obtained with non-local displacements are similar to those ones obtained with a non-local state variable.

3.5 Concluding remarks

In this chapter, we have extended the applicability to a two- and three-dimensional setting of an alternative gradient-enriched continuous formulation to describe the evolution of a failure process. The key idea of this new approach is to combine the standard displacement field $\boldsymbol{u}$ with a smoothed displacement field $\widetilde{\boldsymbol{u}}$, which drives damage evolution and is the solution of a diffusion differential equation.

This new model presents three main advantages. First, introducing the gradient-type enrichment at the level of displacements (rather than some internal variable) does not interfere with the constitutive driver. Second, and from a computational viewpoint, the computation of the consistent tangent matrix needed to achieve quadratic convergence in Newton iterations is much simpler than for the standard models. Third, the boundary conditions for the regularisation equation —for $\widetilde{\boldsymbol{u}}$— have a clear meaning. In this chapter, these boundary conditions have been analysed in detail. The main results are:

- Dirichlet boundary conditions have a clear physical meaning: the two displacement fields are imposed to coincide along all the domain boundary. Neverthe-

less, in a multidimensional setting, this does not allow a correct widening of the damage zone at the boundary, since displacement smoothing is not permitted.

- Analogously to the standard gradient model, homogeneous Neumann boundary conditions may be prescribed. By means of these conditions, $\widetilde{\boldsymbol{u}}$ is smoothed along the domain boundary but reproducibility of order 1 is not ensured.

- Non-homogeneous Neumann boundary conditions solve these difficulties. Nevertheless, they do not ensure conservation of volume.

- In order to solve the above discussed difficulties, combined conditions are proposed. They consist of prescribing Dirichlet boundary conditions for the normal component of the displacement field and non-homogeneous Neumann boundary conditions for the tangential ones. Therefore, preservation of volume is ensured and a relative slip is admitted.

In order to illustrate the regularisation capabilities of the new formulation, where non-locality is introduced by means of smoothed displacements with combined boundary conditions, different two- and three-dimensional tests are carried out. The main results are:

- Regularisation via smoothed displacement precludes mesh dependence also in a multi-dimensional setting: numerical results do not suffer from pathological mesh sensitivity and physically realistic force-displacement curves and damage profiles are obtained.

- Both the ductility in the force-displacement response and the width of the final damage band increase with the characteristic length ℓ.

- The new model presents the same regularisation capabilities and qualitative response than the standard model based on a smoothed state variable.

3.6 Future work

The work carried out in this chapter leaves some open research lines that need to be addressed in the near future.

Size effect. The capability to correctly reproduce size effect —the change of behaviour when the spatial dimensions are scaled— is an important issue to be considered, see Bažant (2000) for an overview of this scaling behaviour.

Together with softening regularisation, non-local models are expected to capture size effects. In fact, among other reasons, non-locality was historically motivated by the need to capture them, see Bažant and Jirásek (2002).

Hence, it would be interesting to investigate the capacity of the gradient-enhanced damage model based on smoothed displacements to reproduce these scaling effects. In Rodríguez-Ferran et al. (2011), a three-point bending test with seven different sizes is carried out. Although the numerical experiments are in reasonable accordance with Bažant's Size Effect Law (SEL), further research is needed to analyse why the correspondence with SEL is not as strong as perhaps would be expected.

Initiation of failure with non-local displacements. Regularised damage models allow to overcome the well-known problems of local approaches such as pathological mesh dependence. Nevertheless, they suffer some drawbacks such as damage initiation when dealing with notched specimens.

Indeed, in quasi-brittle failure analyses of notched specimens, experimental tests show that cracks should propagate from the notch. However, as shown by Simone et al. (2004), numerical simulations predict that cracks appear away from the tip. This pathological behaviour is due to the fact that in the presence of a predefined notch, the maximum non-local equivalent strain is inaccurately predicted, since at the crack tip, the stress field and thus the strains are singular —the stress and strain become infinitely large as the distance r from the crack tip tends to 0.

Taking into account that at the crack tip displacements are not singular, averaging the displacement field —that is, using smoothed displacements to regularise softening— may lead to a correct damage initiation.

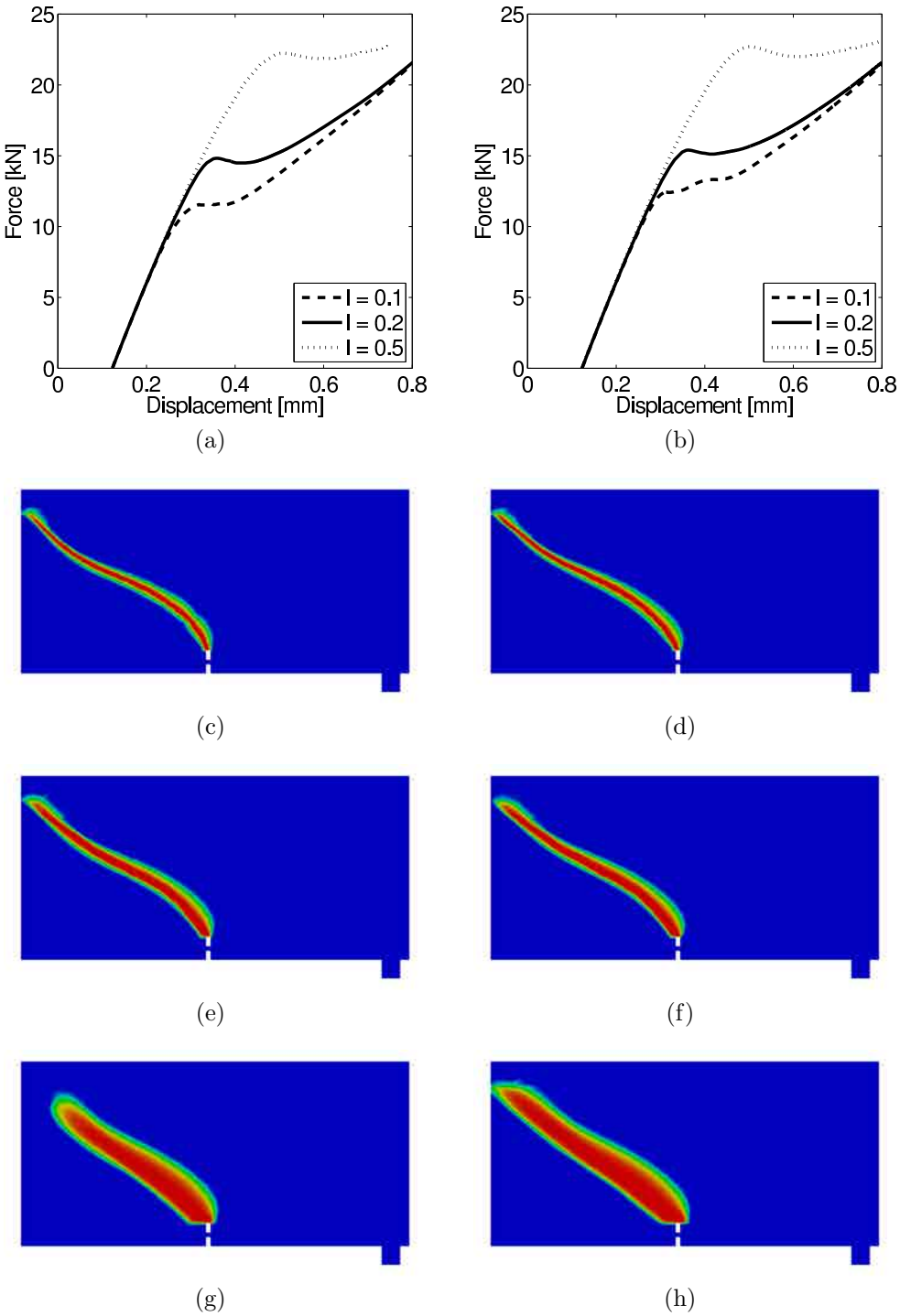

Figure 3.15: Three-point reinforced prestressed bending beam. Left column (damage model based on smoothed displacements): (a) force-displacement curves and damage profiles obtained by means of (c) $\ell = 0.1$ cm, (e) $\ell = 0.2$ cm and (g) $\ell = 0.5$ cm. Right column (standard damage model): (b) force-displacement curves and damage profiles obtained by means of (d) $\ell = 0.1$ cm, (f) $\ell = 0.2$ cm and (h) $\ell = 0.5$ cm.

Chapter 4

Continuous-discontinuous damage model: non-cohesive cracks in a regularised bulk

---

In this chapter we propose a new continuous-discontinuous strategy for the simulation of failure. The continuous bulk is regularised by means of a gradient-enhanced damage model, where non-locality is introduced at the level of displacements, see Chapter 3. As soon as the damage parameter is close or equal to 1, a traction-free crack is introduced. In order to determine the direction of crack growth, a new criterion is proposed. In contrast to traditional techniques, where mechanical criteria are used to define the crack path, here a geometrical approach is used. More specifically, given a regularised damage field $D(\boldsymbol{x})$, we propose to propagate the discontinuity following the direction dictated by the medial axis of the isoline (or isosurface in 3D) $D(\boldsymbol{x}) = D^*$. The proposed approach is tested on different two- and three-dimensional examples that illustrate that this combined methodology is able to deal with damage growth and material separation.

4.1 Introduction

On the one hand, regularised damage models (see the integral-type techniques proposed by Bažant and Lin (1988), Bažant and Pijaudier-Cabot (1988) and Comi (2001)

and the gradient-type formulations by Peerlings et al. (1996) and Comi (1999) among others) can be used to describe the early stages of the failure process. However, they do not introduce displacement discontinuities. As a consequence, numerical interaction between physically separated parts of the body persists, which may cause an unrealistic spread of damage, see Comi et al. (2007). Furthermore, dealing with material separation and explicitly modelling the crack geometry is necessary for many applications. For instance, in hydraulic fracturing processes —such as fracturing of oil and gas reservoirs— rock is fractured by an injected liquid whose hydraulic pressure depends on the shape of the crack; in structural failure due to leakage, freezing of the pore water or chemicals in the surrounding fluids, the flow of the fluid depends on the geometry of the crack and in fibre-reinforced concrete structures, where concrete contains fibrous materials that increase its structural stiffness, see Figure 4.1, the bridging capacity of fibres depend on their orientation with respect to the crack.

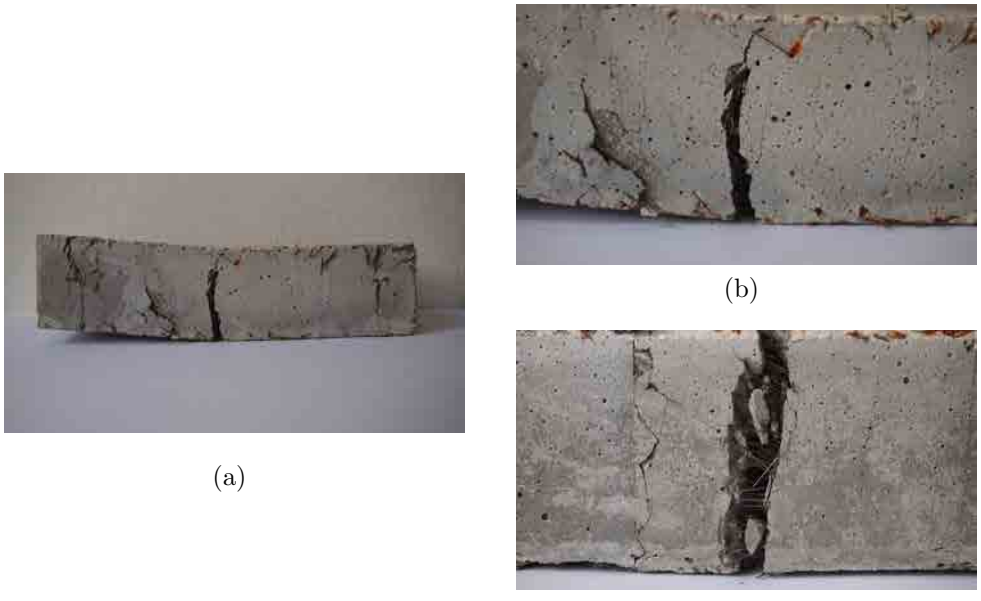

(a) (b) (c)

Figure 4.1: Steel-fibre reinforced concrete beam subjected to three-point bending. Courtesy of Climent Molins (UPC).

On the other hand, discontinuous models (see for instance the pioneering works by Simo et al. (1993), Simo and Oliver (1994) and Armero and Garikipati (1996)) can be used to describe the last stages of the failure process. Nevertheless, they cannot describe neither damage inception nor its diffuse propagation.

As suggested by the above discussion, combining these two theories —using a continuous-discontinuous approach— is a way to achieve a better characterisation of the whole failure process. The main idea of these continuous-discontinuous strategies is to employ damage mechanics in order to describe the inception and the propagation of damage and fracture mechanics in order to deal with cracks and material separation.

In this chapter, we present a new combined approach. Specifically, the main contributions of this chapter are:

1. **To propose a new combined formulation to simulate quasi-brittle failure**. In this new formulation, an implicit gradient-enhanced damage model based on smoothed displacements is used to simulate the initial stages of failure. As soon as a critical situation is achieved —the damage parameter at all the integration points in a finite element reaches a critical value $D_{\text{crit}} \simeq 1$— a non-cohesive crack is introduced. Special emphasis is placed on the consistent tangent matrix needed to attain quadratic convergence in the full Newton-Raphson method.

2. **To propose a new criterion to determine the crack path**. One important issue concerning the transition from the continuous to the discontinuous approach is the location of a crack and the definition of the direction along which it propagates. Regarding combined approaches, fracture mechanics cannot be employed, since the critical imperfection from which cracking initiates is unknown. Therefore, other criteria should be used. Here, the discontinuity is propagated following the direction dictated by the medial axis of the already damaged domain, a tool proposed by Blum (1967) that is widely used for image analysis, computer vision applications or mesh generation.

The structure of the chapter is as follows. In Section 4.2 the new continuous-discontinuous damage model based on smoothed displacements is presented. Section 4.3 deals with the new criterion to determine the crack path. The capabilities of this new combined approach are illustrated by means of some numerical examples in Section 4.4. Finally, the concluding remarks in Section 4.5 and the future directions in Section 4.6 close this chapter.

4.2 Gradient-enhanced damage model

To simulate the last stages of a failure process —where the damage parameter is close to one—, we propose to couple the implicit gradient-enhanced model based on smoothed displacements with propagating cracks. In this final stage of the process, the bulk Ω is bounded by $\Gamma = \Gamma_u \cup \Gamma_t \cup \Gamma_d$, as shown in Figure 4.2. Prescribed displacements are imposed on Γ_u, while tractions are imposed on Γ_t. The boundary Γ_d consists of the boundary of the crack.

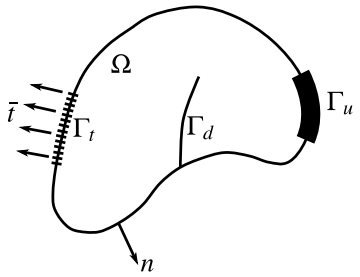

Figure 4.2: Notations for a body with a crack subjected to loads and imposed displacements.

The key idea of this combined strategy is to characterise the problem fields —both local and non-local displacements— by means of the eXtended finite element method (X-FEM), see Belytschko and Black (1999) and Moës et al. (1999). Indeed, and with X-FEM, $\boldsymbol{u}$ and $\widetilde{\boldsymbol{u}}$ can be decomposed as

$$\boldsymbol{u}(\boldsymbol{x}) = \boldsymbol{u}^1(\boldsymbol{x}) + \psi(\boldsymbol{x})\,\boldsymbol{u}^2(\boldsymbol{x}) \tag{4.1a}$$

$$\widetilde{\boldsymbol{u}}(\boldsymbol{x}) = \widetilde{\boldsymbol{u}}^1(\boldsymbol{x}) + \psi(\boldsymbol{x})\,\widetilde{\boldsymbol{u}}^2(\boldsymbol{x}) \tag{4.1b}$$

where $\boldsymbol{u}^i$, $\widetilde{\boldsymbol{u}}^i$ $(i = 1, 2)$ are continuous fields in Ω and ψ is the sign function centred at the discontinuity Γ_d —equals 1 at one side of the discontinuity and equals -1 at the other one. It is noted that if the body Ω is not entirely crossed by the discontinuity Γ_d, ψ is ambiguously defined. Nevertheless, this ambiguity is not a critical issue, since after the FE discretisation, the enrichment function is multiplied by nodal shape functions that vanish in the region where ψ is ambiguous.

Moreover, the continuous parts $\boldsymbol{u}^1$ and $\widetilde{\boldsymbol{u}}^1$ correspond to the displacement field without any crack, while the additional discontinuous fields $\psi\boldsymbol{u}^2$ and $\psi\widetilde{\boldsymbol{u}}^2$ model the crack.

It must be stressed that in Equation (4.1), both mechanical and smoothed displacements are discontinuous. This requirement —the auxiliary displacement field $\widetilde{\boldsymbol{u}}$

being discontinuous— is a natural choice. Indeed, let us consider the regularisation equation (3.2) with $\ell = 0$. Then, since the model is local, the expected solution is $\boldsymbol{u} = \widetilde{\boldsymbol{u}}$ and, therefore, given a discontinuous displacement field $\boldsymbol{u}$ the regularised displacement field $\widetilde{\boldsymbol{u}}$ must also be discontinuous.

4.2.1 Governing equations

The strong form of the equilibrium equation and boundary conditions for the body $\bar{\Omega} = \Omega \cup \Gamma$ without body forces is given by

$$\nabla \cdot \boldsymbol{\sigma} = \mathbf{0} \quad \text{in } \Omega \tag{4.2a}$$

$$\boldsymbol{\sigma} \cdot \boldsymbol{n} = \bar{\boldsymbol{t}} \quad \text{on } \Gamma_t \tag{4.2b}$$

$$\boldsymbol{\sigma} \cdot \boldsymbol{n} = \mathbf{0} \quad \text{on } \Gamma_d \tag{4.2c}$$

$$\boldsymbol{u} = \boldsymbol{u}^* \quad \text{on } \Gamma_u \tag{4.2d}$$

where $\boldsymbol{\sigma}$ is the Cauchy stress tensor, $\boldsymbol{u}^*$ is a prescribed displacement on the Dirichlet boundary, $\bar{\boldsymbol{t}}$ is the traction on the Neumann boundary and $\boldsymbol{n}$ is the outward unit normal to the body. Note that in this chapter, the transition from a continuous to a discontinuous strategy is carried out when the damage parameter is close to one thus introducing a traction-free crack, see Equation (4.2c).

In the proposed formulation, the regularisation PDE (3.2) is employed to incorporate non-locality. Therefore, appropriate boundary conditions for $\widetilde{\boldsymbol{u}}$ must be defined. Here, combined boundary conditions

$$\left.\begin{aligned} \widetilde{\boldsymbol{u}}^i \cdot \boldsymbol{n} &= \boldsymbol{u}^i \cdot \boldsymbol{n} \\ \nabla\left(\widetilde{\boldsymbol{u}}^i \cdot \boldsymbol{t}_1\right) \cdot \boldsymbol{n} &= \nabla\left(\boldsymbol{u}^i \cdot \boldsymbol{t}_1\right) \cdot \boldsymbol{n} \\ \nabla\left(\widetilde{\boldsymbol{u}}^i \cdot \boldsymbol{t}_2\right) \cdot \boldsymbol{n} &= \nabla\left(\boldsymbol{u}^i \cdot \boldsymbol{t}_2\right) \cdot \boldsymbol{n} \end{aligned}\right\} \text{on } \Gamma \tag{4.3}$$

where $i = 1, 2$, are prescribed for the continuous displacement fields $\widetilde{\boldsymbol{u}}^1$ and $\widetilde{\boldsymbol{u}}^2$, see Section 3.3 for a detailed discussion.

Both equations —equilibrium and regularisation equations— are first cast in a weak form to be subsequently linearised. Thus, the equilibrium equation (4.2) leads to

$$\int_\Omega \nabla^s \boldsymbol{\omega}^1 : \boldsymbol{\sigma} \, \mathrm{d}\Omega = \int_{\Gamma_t} \boldsymbol{\omega}^1 \cdot \bar{\boldsymbol{t}} \, \mathrm{d}\Gamma \qquad \forall \boldsymbol{\omega}^1 \in H^1(\Omega) \tag{4.4a}$$

$$\int_\Omega \psi \nabla^s \boldsymbol{\omega}^2 : \boldsymbol{\sigma} \, \mathrm{d}\Omega = \int_{\Gamma_t} \psi \boldsymbol{\omega}^2 \cdot \bar{\boldsymbol{t}} \, \mathrm{d}\Gamma \qquad \forall \boldsymbol{\omega}^2 \in H^1(\Omega) \tag{4.4b}$$

whereas the regularisation equation leads to

$$\begin{aligned}\int_\Omega \widetilde{\boldsymbol{\omega}}^1 \cdot \widetilde{\boldsymbol{u}}\,\mathrm{d}\Omega \;&+\; \ell^2 \int_\Omega \nabla\widetilde{\boldsymbol{\omega}}^1 : \left(\nabla\widetilde{\boldsymbol{u}}^1 + \psi\nabla\widetilde{\boldsymbol{u}}^2\right)\,\mathrm{d}\Omega = \int_\Omega \widetilde{\boldsymbol{\omega}}^1 \cdot \boldsymbol{u}\,\mathrm{d}\Omega + \\ &+\; \ell^2 \int_\Gamma \left(\widetilde{\boldsymbol{\omega}}^1 \cdot \boldsymbol{t}_1\right) \cdot \left[\nabla\left(\boldsymbol{u}^1 \cdot \boldsymbol{t}_1\right) \cdot \boldsymbol{n} + \psi\nabla\left(\boldsymbol{u}^2 \cdot \boldsymbol{t}_1\right) \cdot \boldsymbol{n}\right]\,\mathrm{d}\Gamma \\ &+\; \ell^2 \int_\Gamma \left(\widetilde{\boldsymbol{\omega}}^1 \cdot \boldsymbol{t}_2\right) \cdot \left[\nabla\left(\boldsymbol{u}^1 \cdot \boldsymbol{t}_2\right) \cdot \boldsymbol{n} + \psi\nabla\left(\boldsymbol{u}^2 \cdot \boldsymbol{t}_2\right) \cdot \boldsymbol{n}\right]\,\mathrm{d}\Gamma \qquad (4.5a)\end{aligned}$$

$$\begin{aligned}\int_\Omega \psi\widetilde{\boldsymbol{\omega}}^2 \cdot \widetilde{\boldsymbol{u}}\,\mathrm{d}\Omega \;&+\; \ell^2 \int_\Omega \nabla\widetilde{\boldsymbol{\omega}}^2 : \left(\psi\nabla\widetilde{\boldsymbol{u}}^1 + \nabla\widetilde{\boldsymbol{u}}^2\right)\,\mathrm{d}\Omega = \int_\Omega \psi\widetilde{\boldsymbol{\omega}}^2 \cdot \boldsymbol{u}\,\mathrm{d}\Omega + \\ &+\; \ell^2 \int_\Gamma \left(\widetilde{\boldsymbol{\omega}}^2 \cdot \boldsymbol{t}_1\right) \cdot \left[\psi\nabla\left(\boldsymbol{u}^1 \cdot \boldsymbol{t}_1\right) \cdot \boldsymbol{n} + \nabla\left(\boldsymbol{u}^2 \cdot \boldsymbol{t}_1\right) \cdot \boldsymbol{n}\right]\,\mathrm{d}\Gamma \\ &+\; \ell^2 \int_\Gamma \left(\widetilde{\boldsymbol{\omega}}^2 \cdot \boldsymbol{t}_2\right) \cdot \left[\psi\nabla\left(\boldsymbol{u}^1 \cdot \boldsymbol{t}_2\right) \cdot \boldsymbol{n} + \nabla\left(\boldsymbol{u}^2 \cdot \boldsymbol{t}_2\right) \cdot \boldsymbol{n}\right]\,\mathrm{d}\Gamma \qquad (4.5b)\end{aligned}$$

where $\boldsymbol{\omega} = \boldsymbol{\omega}^1 + \psi\boldsymbol{\omega}^2$ and $\widetilde{\boldsymbol{\omega}} = \widetilde{\boldsymbol{\omega}}^1 + \psi\widetilde{\boldsymbol{\omega}}^2$ are the test functions, see Appendix A for details.

4.2.2 Linearisation and consistent tangent matrix

Regarding the finite element discretisation, local and non-local displacements read, in the domain of an element with enhanced nodes, as

$$\boldsymbol{u}(\boldsymbol{x}) \simeq \boldsymbol{u}^h(\boldsymbol{x}) = \mathbf{N}(\boldsymbol{x})\mathbf{u}^1 + \psi(\boldsymbol{x})\mathbf{N}(\boldsymbol{x})\mathbf{u}^2 \qquad (4.6a)$$

$$\widetilde{\boldsymbol{u}}(\boldsymbol{x}) \simeq \widetilde{\boldsymbol{u}}^h(\boldsymbol{x}) = \mathbf{N}(\boldsymbol{x})\widetilde{\mathbf{u}}^1 + \psi(\boldsymbol{x})\mathbf{N}(\boldsymbol{x})\widetilde{\mathbf{u}}^2 \qquad (4.6b)$$

where $\mathbf{N}$ is the matrix of standard finite element shape functions, $\mathbf{u}^1$, $\widetilde{\mathbf{u}}^1$ are the basic nodal degrees of freedom and $\mathbf{u}^2$, $\widetilde{\mathbf{u}}^2$ are the enhanced ones. The discrete format of the equilibrium equation, see Equations (4.4), leads to the discrete weak form

$$\int_\Omega \mathbf{B}^T\boldsymbol{\sigma}\,\mathrm{d}\Omega = \int_{\Gamma_t} \mathbf{N}^T\bar{\boldsymbol{t}}\,\mathrm{d}\Gamma \qquad (4.7a)$$

$$\int_\Omega \psi\mathbf{B}^T\boldsymbol{\sigma}\,\mathrm{d}\Omega = \int_{\Gamma_t} \psi\mathbf{N}^T\bar{\boldsymbol{t}}\,\mathrm{d}\Gamma \qquad (4.7b)$$

while the regularisation equation, see Equations (4.5), leads to

$$(\mathbf{M} + \ell^2\mathbf{D})\widetilde{\mathbf{u}}^1 + (\mathbf{M}_\psi + \ell^2\mathbf{D}_\psi)\widetilde{\mathbf{u}}^2 = (\mathbf{M} + \ell^2\mathbf{K}_{\mathrm{BC}})\widetilde{\mathbf{u}}^1 + (\mathbf{M}_\psi + \ell^2\mathbf{K}_{\psi,\mathrm{BC}})\mathbf{u}^2 \qquad (4.8a)$$

$$(\mathbf{M}_\psi + \ell^2\mathbf{D}_\psi)\widetilde{\mathbf{u}}^1 + (\mathbf{M} + \ell^2\mathbf{D})\widetilde{\mathbf{u}}^2 = (\mathbf{M}_\psi + \ell^2\mathbf{K}_{\psi,\mathrm{BC}})\mathbf{u}^1 + (\mathbf{M} + \ell^2\mathbf{K}_{\mathrm{BC}})\widetilde{\mathbf{u}}^2 \qquad (4.8b)$$

with matrices defined in Appendix B.

Some remarks about the discretisation:

- Equation (4.7a) is the standard non-linear system of equilibrium equations, while Equation (4.7b) deals with the contribution of the crack. Indeed, the effect of the displacement discontinuity is taken into account by enforcing equilibrium of the enriched internal and external forces, see the terms in the LHS and in the RHS of Equation (4.7b) respectively.

- Matrices $\mathbf{M}_\psi$ and $\mathbf{D}_\psi$ can be understood as enriched mass and diffusivity matrices respectively, since the expression is the same as $\mathbf{M}$ and $\mathbf{D}$ except for the enrichment function, see Appendix B.

- Note that the appealing symmetry of Equations (4.8) is due to the fact that the enrichment function is the sign function ($\psi\psi = +1$).

Analogously to the continuous model, see Rodríguez-Ferran et al. (2005), smoothed displacements are attractive from a computational viewpoint in the combined formulation, especially regarding its consistent linearisation. Indeed, linearisation of Equations (4.7) and (4.8) results in the tangent matrix

$$\mathbf{K}_{\text{tan}} = \begin{bmatrix} \mathbf{K}_{\text{sec}} & \mathbf{K}_{\psi,\text{sec}} & \mathbf{K}_{\text{loc}} & \mathbf{K}_{\psi,\text{loc}} \\ \mathbf{K}_{\psi,\text{sec}} & \mathbf{K}_{\text{sec}} & \mathbf{K}_{\psi,\text{loc}} & \mathbf{K}_{\text{loc}} \\ -(\mathbf{M} + \ell^2\mathbf{K}_{\text{BC}}) & -(\mathbf{M}_\psi + \ell^2\mathbf{K}_{\psi,\text{BC}}) & \mathbf{M} + \ell^2\mathbf{D} & \mathbf{M}_\psi + \ell^2\mathbf{D}_\psi \\ -(\mathbf{M}_\psi + \ell^2\mathbf{K}_{\psi,\text{BC}}) & -(\mathbf{M} + \ell^2\mathbf{K}_{\text{BC}}) & \mathbf{M}_\psi + \ell^2\mathbf{D}_\psi & \mathbf{M} + \ell^2\mathbf{D} \end{bmatrix}, \tag{4.9}$$

see Appendix B for details.

Note that in continuous approaches, the evaluation of the tangent matrix usually requires the quadrature of functions that are polynomials —or functions that are well approximated by polynomials. Hence, traditional quadrature rules, for example Gauss quadratures, can be used. Nevertheless, in continuous-discontinuous strategies, the approximation space is enriched by discontinuous functions, see the tangent matrix (4.9). Therefore, alternative integration rules must be used. As reviewed by Belytschko et al. (2009), several different methods can be found in the literature. These methods include higher-order Gauss quadratures, adaptive quadratures and subdomain quadratures. In this work, this last approach is used: when an element is intersected by a discontinuity, it is subdivided into quadrature subdomains where a standard Gauss rule is used, see Appendix C for details.

4.3 Geometric criterion to determine the crack path

One important issue concerning the transition from the continuous to the discontinuous approach is the location of a crack and the definition of the direction along which it propagates. Regarding combined approaches, fracture mechanics cannot be employed, since the critical imperfection from which cracking initiates is unknown. Therefore, other criteria should be used.

Traditionally, determining the direction of crack growth is tackled from a mechanical point of view. In Jirásek and Zimmermann (2001), the crack is assumed to be perpendicular to the direction of maximum principal stress or strain. In Simone et al. (2003), the crack grows following the direction of maximum accumulation of the non-local equivalent strain in a zone ahead of the discontinuity tip. Comi et al. (2007) use the damage band to locate the propagating crack. They propose to approximate the damage values in the process zone by a fourth-order polynomial and to locate the crack perpendicular to the direction of maximum curvature of the interpolating polynomial.

As seen in the above references, the key idea of these approaches is to use the Gauss points values —non-local stress, non-local strain or damage— to define the direction of crack growth. Nevertheless, due to the singularity of the stress and strain fields at the crack tip, the value of these quantities may lead to an incorrect crack propagation.

Here, an alternative way of defining the direction of crack growth is presented. The main idea of this new approach is to avoid the use of mechanical criteria to determine the advancing crack front thus using the geometry of the damaged zone instead. More specifically, the idea is to collapse a damaged zone —which can be understood as a crack of thickness equal to the damaged band— into a zero-thickness crack. Taking into account that the width of the damaged zone is controlled by the characteristic length ℓ, and letting ℓ tend to zero, it can be intuitively seen that the zero-thickness crack should be located in the middle of the damaged zone, see Figure 4.3.

This intuitive idea —going through the middle of a given domain— can be directly formalised by means of the *medial axis* concept.

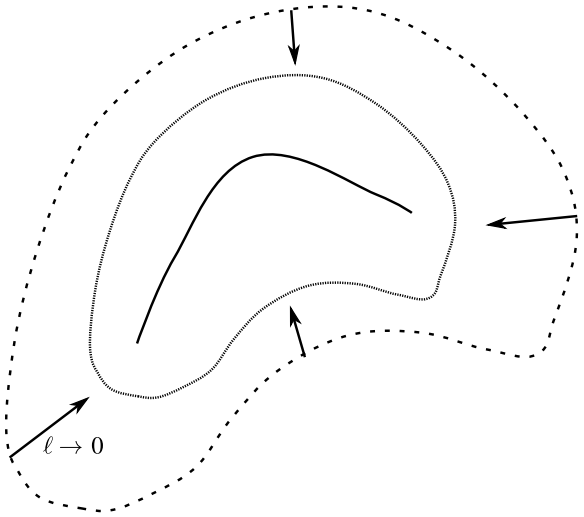

Figure 4.3: Given a damage domain (discontinuous line) and reducing the diffusion, one observes that the damaged zone can be collapsed into a zero-thickness line located in the middle of the diffuse zone.

4.3.1 Medial axis

The medial axis (MA) of a solid was first proposed by Blum (1967) as a geometric tool in image analysis. Intuitively, the MA of an object —often called *medial surface* when dealing with 3D objects— can be thought of as its skeleton. Mathematically, the MA of a solid is defined as the loci of centres of bi-tangent interior balls, see Figure 4.4.

Although this geometric tool is widely used in computer image analysis or for mesh generation purposes, the computation of the MA is a difficult task due to its instability, since it is heavily sensitive to details in the boundary of the object, see Figures 4.5(a)-4.5(d). In order to overcome this main drawback, different simplified and stable versions of the MA can be found in the literature, see Pizer et al. (2003) for a detailed survey.

One of these stable criteria is based on the separation angle, see Foskey et al. (2003). Let us consider a point P of the MA and let P_1, P_2 denote the two points of tangency of the interior ball with centre at P to the object. Then, the separation angle of this point $S(P)$ is the value in $[0, \pi]$ such that

$$S(P) = \angle P_1 P P_2, \tag{4.10}$$

see Figure 4.6(a). More generally, if there are more than two points of tangency, see

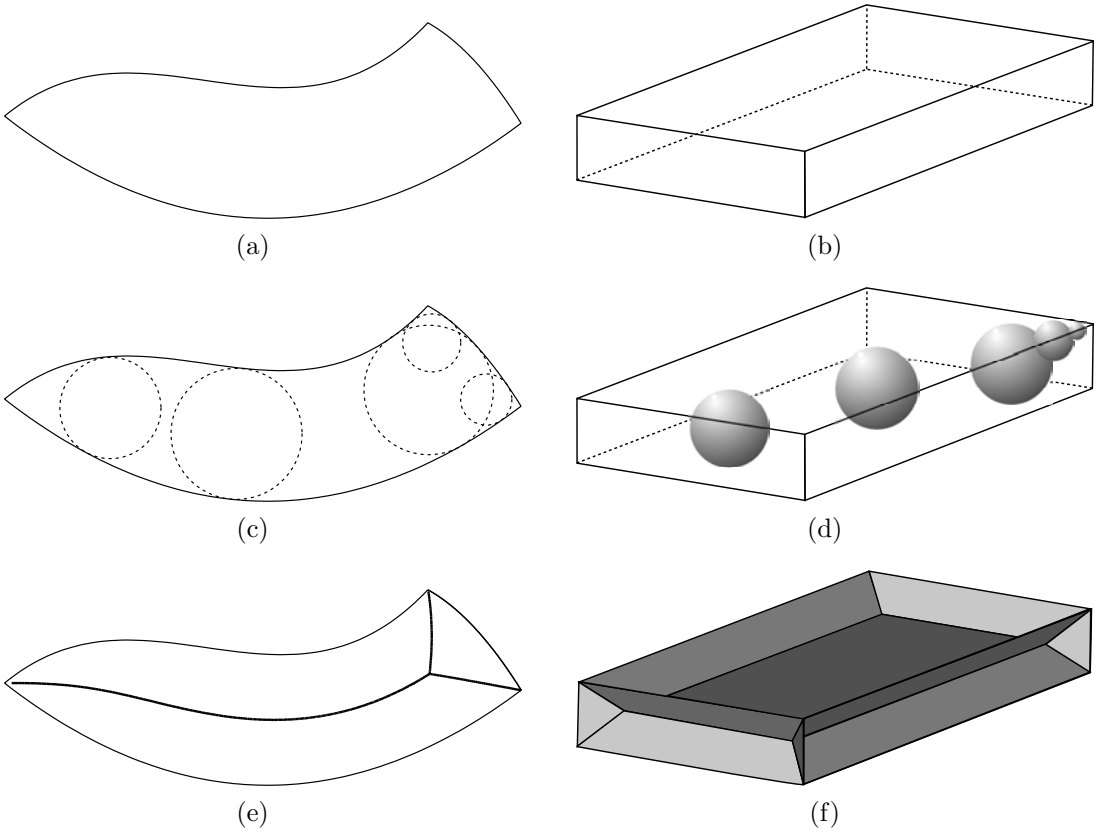

Figure 4.4: Left column (2D case): (a) a 2D object, (c) bi-tangent interior circles, (e) 2D MA. Right column (3D case): (b) a 3D object, (d) bi-tangent interior spheres, (f) 3D MA, often called *medial surface*.

Figure 4.6(b), the separation angle $S(P)$ is defined as the largest angle between P and each pair of points of tangency

$$S(P) = \max_{P_1, P_2 \in T(P)} (\angle P_1 P P_2) \tag{4.11}$$

where $T(P)$ denote the set of points of tangency of the interior ball with centre at P to the object.

Therefore, and given an angle $\theta \in [0, \pi]$, the $\theta-$SMA of an object is defined as the set of points of the MA with separation angle greater than θ. As seen in Figures 4.5(e)-4.5(g), this modified definition allows to remove the spurious branches that appear when computing the MA. It is noted here, that the use of the $\theta-$SMA does not lead to only one crack. Indeed, this tool allows to consider the coalescence and branching of cracks, see Figure 4.7.

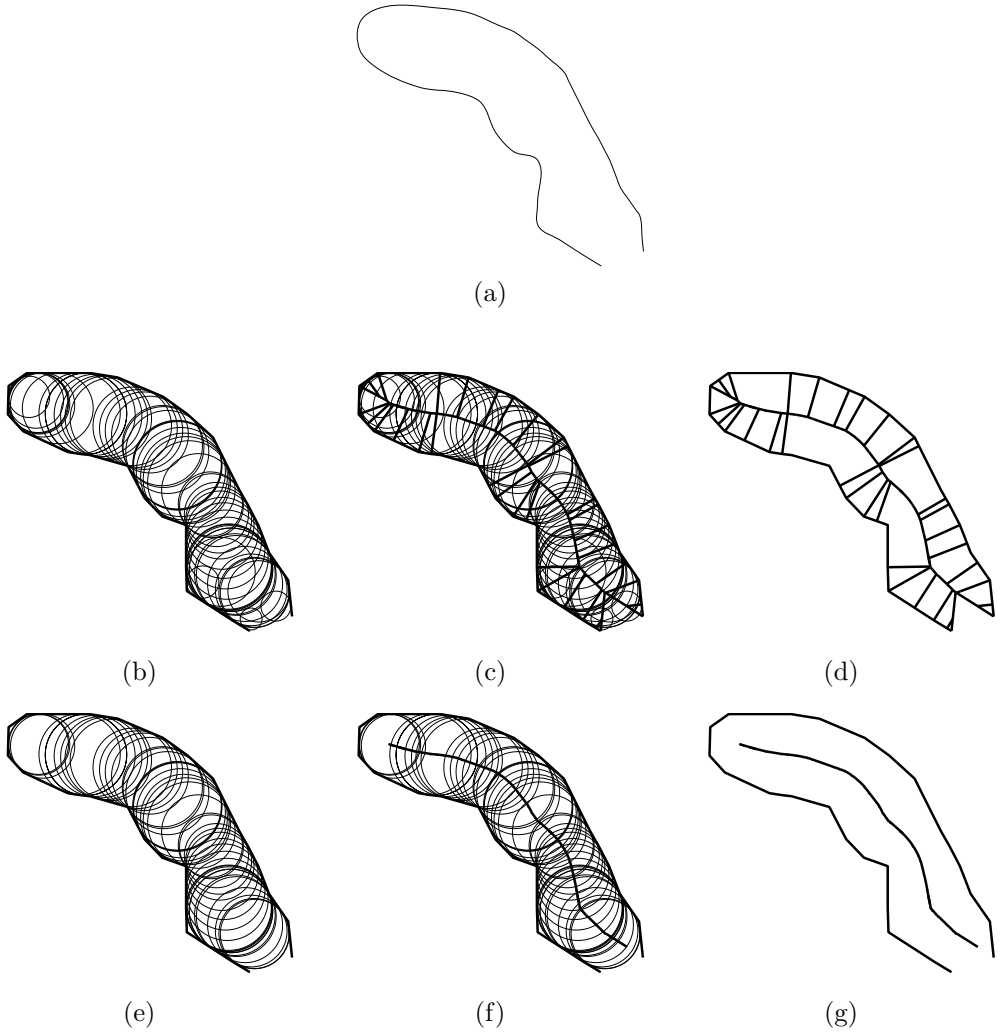

Figure 4.5: (a) Given a domain Ω, (b) the bi-tangent interior balls are computed. (c) Joining their centres, (d) the MA is obtained. (e) If only the circles with separation angle greater than $\theta = \frac{\pi}{2}$ are considered, (f) the spurious branches are removed and (g) the $\theta-$SMA is obtained.

4.3.2 The $\theta-$simplified medial axis as a tool to locate cracks

Once the transition criterion is fulfilled, a propagating crack is introduced. Note that since the crack is introduced when damage is close to one, it can be considered as a traction-free crack. The proposed strategy consists of different steps:

- Crack initiation: as done in Cervera et al. (2010), we will assume that a crack may start only from the boundary of the structure. Therefore, once the damage

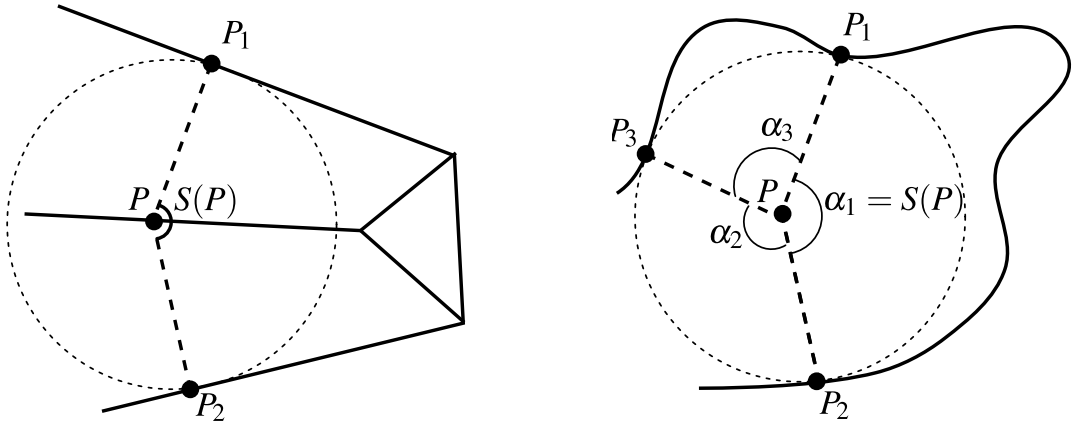

Figure 4.6: (a) Separation angle $S(P)$ of a point P: adapted from Foskey et al. (2003). (b) If there are more than two points of tangency, the separation angle $S(P)$ is defined as the largest angle between P and each pair of points of tangency.

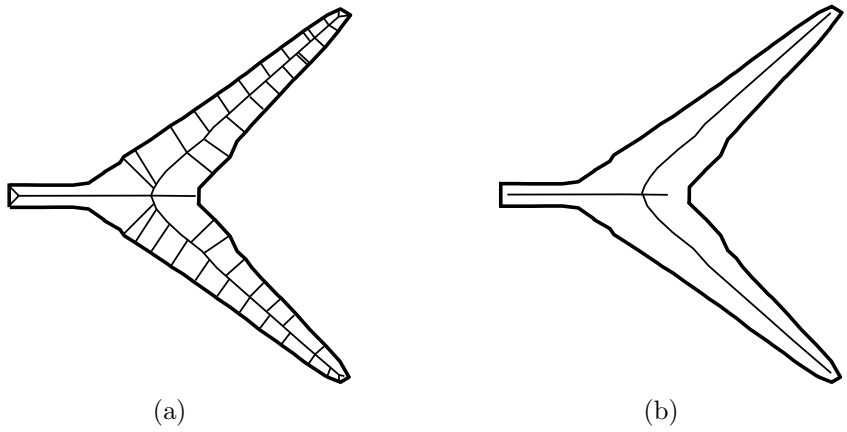

Figure 4.7: (a) Medial axis of a Y-shaped domain. (b) $\theta-$simplified medial axis of a Y-shaped domain ($\theta = \frac{2}{3}\pi$).

parameter reaches a value $D_{\text{crit}} \simeq 1$ in an element located on the boundary of the mesh, a crack is introduced in that element, see Figure 4.8(a). Moreover, the damage parameter in that cracked element is fixed to D_{crit}. Hence, the damage parameter in the cracked element does not evolve anymore and the material in the surrounding unloads.

- $\theta-$SMA computation: in order to define the direction of crack growth, and suggested by Section 4.3.1, the $\theta-$SMA of the already damaged domain is com-

puted, see Figure 4.8(b). More specifically, the $\theta-$SMA of the isoline (or the isosurface in 3D) $D(\boldsymbol{x}) = D^*$ is computed. It must be stressed that the exact computation of the MA is difficult in general due to the sensitivity to perturbations. Nevertheless, there are many available open-source software packages that allow to compute it in a user-friendly manner. Here, the Matlab routines by Suresh (2013) and the C++ code by Yoshizawa (2013) have been used to compute the MA of 2D and 3D solids respectively. Then, we have modified them to compute the $\theta-$SMA. In particular, given an angle $\theta \in [0, \pi]$, the points belonging to the MA with a separation angle lower than θ are removed.

- Crack propagation: once the crack tip is located and the $\theta-$SMA is computed, the direction of crack propagation may be defined. The discontinuity goes from the crack tip following the direction dictated by the $\theta-$SMA until $D > D_{\text{crit}}$ is no longer satisfied, see Figure 4.8(c). Note that the problem is solved by means of an incremental-iterative scheme and within each step, the crack length is fixed. In other words, *crack propagation* only takes place at the end of a time step.

- Finite element enrichment: to model a crack tip, the displacement jump at the discontinuity tip is set to zero. In order to prevent crack opening and sliding at the current crack tip, only standard degrees of freedom for the nodes of the edge containing the crack tip are considered, see Figure 4.8(d). As soon as the discontinuity is extended to the next element, nodes behind the crack tip are enriched.

As seen in step 2, in order to compute the θ-SMA, two different parameters must be considered: the value of the separation angle θ and the value of the isoline (or isosurface) $D(\boldsymbol{x}) = D^*$.

Setting the value of the separation angle $\boldsymbol{\theta}$. In this work, the $\theta-$simplified medial axis and the $\theta-$simplified medial surface are used to locate the crack through the middle of the damaged bulk. That is, their main goal is to avoid the spurious cracks emanating from the main crack. Different examples —all of them introduced in Chapter 3— have been carried out in order to analyse the sensitivity to this value.

First, the two-dimensional square plate under mode I loading conditions is retrieved. As seen in Figure 4.9, the spurious branches appear with low values of θ.

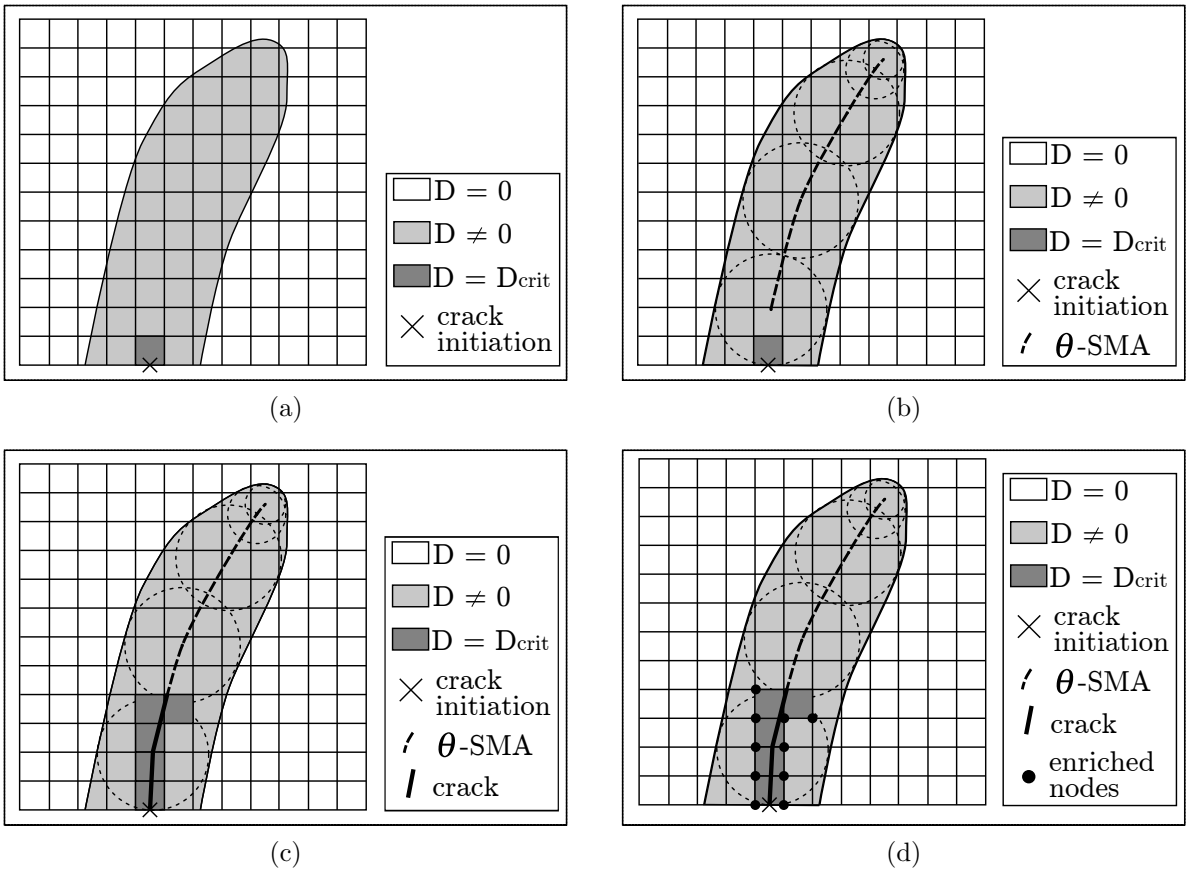

Figure 4.8: The $\theta-$SMA as a tool to locate cracks: (a) Crack initiation; (b) $\theta-$SMA computation; (c) Crack propagation; (d) Finite element enrichment by means of X-FEM.

Nevertheless, with a separation angle large enough, only the main discontinuity is captured.

Second, the two-dimensional single-edge notched beam is analysed. Analogous results are obtained, see Figure 4.10. On the one hand, if a low value of θ is considered, several spurious branches are obtained. This is due to the fact that this algorithm is unstable —small variations in the boundary of the solid may lead to large changes in its medial axis. On the other hand, if higher values of θ are considered, only the main discontinuity is captured.

To sum up, the sensitivity to the value of θ is minimal provided that θ is large enough (with $\theta > \frac{\pi}{2}$ only the main path is typically obtained).

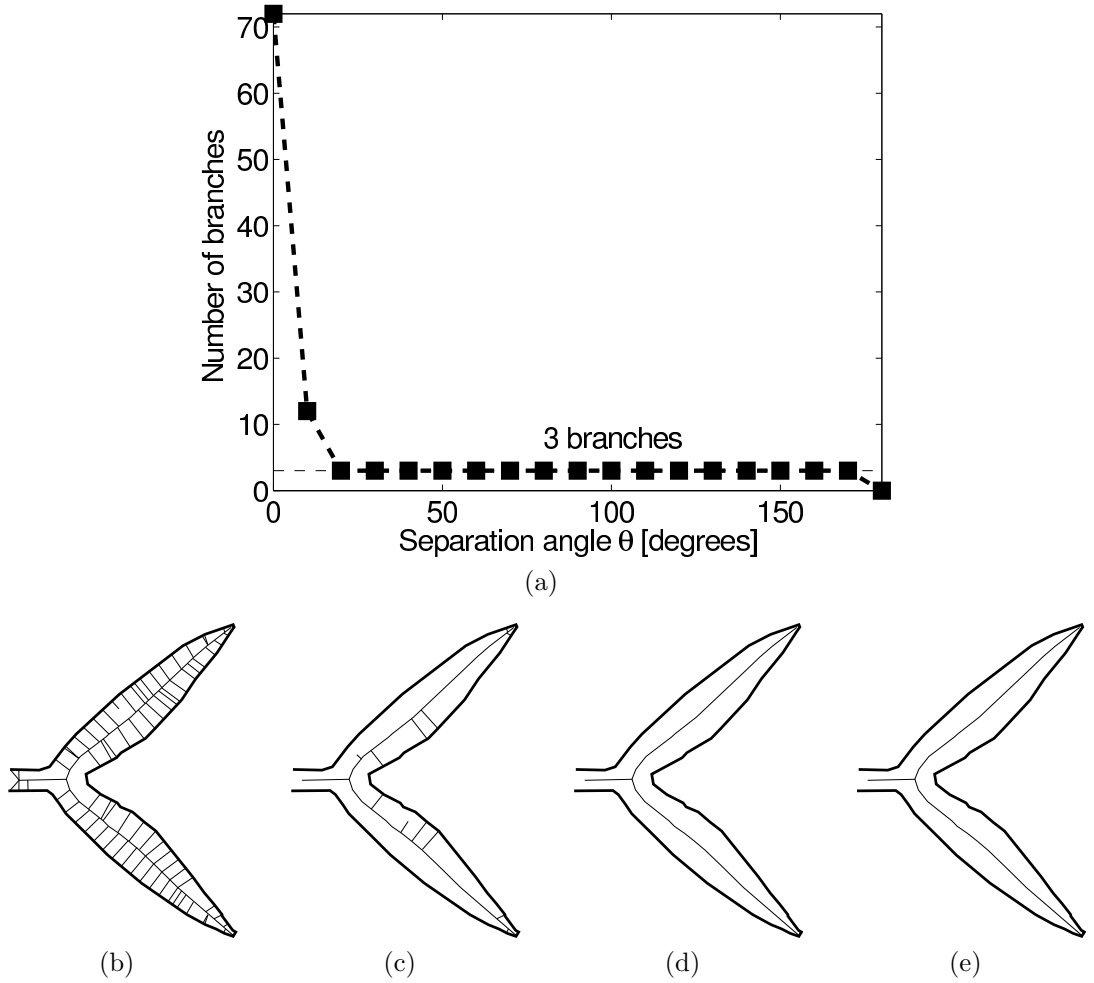

Figure 4.9: Square plate under mode I loading conditions. (a) Number of obtained branches with the $\theta-$SMA as a function of the value of θ and $\theta-$simplified medial axis obtained with (b) $\theta = 0°$, (c) $\theta = 10°$, (d) $\theta = 50°$ and (e) $\theta = 100°$.

Setting the value of the isoline (or the isosurface) $D(\boldsymbol{x}) = D^*$. To compute the $\theta-$SMA, the domain $D(\boldsymbol{x}) = D^*$ has to be determined. Since damage is a smoothed field, little differences are expected for different values of D^*. This behaviour is assessed by carrying out the $\theta-$SMA computation of the two previous examples. Both for the square plate under mode I loading conditions and the single-edge notched beam, a fixed separation angle $\theta = 100°$ and three different values of D^* are considered.

As seen in Figure 4.11, the crack-path obtained with a higher value of D^* overlaps the predicted crack-path with a lower D^*. The only difference concerns the length

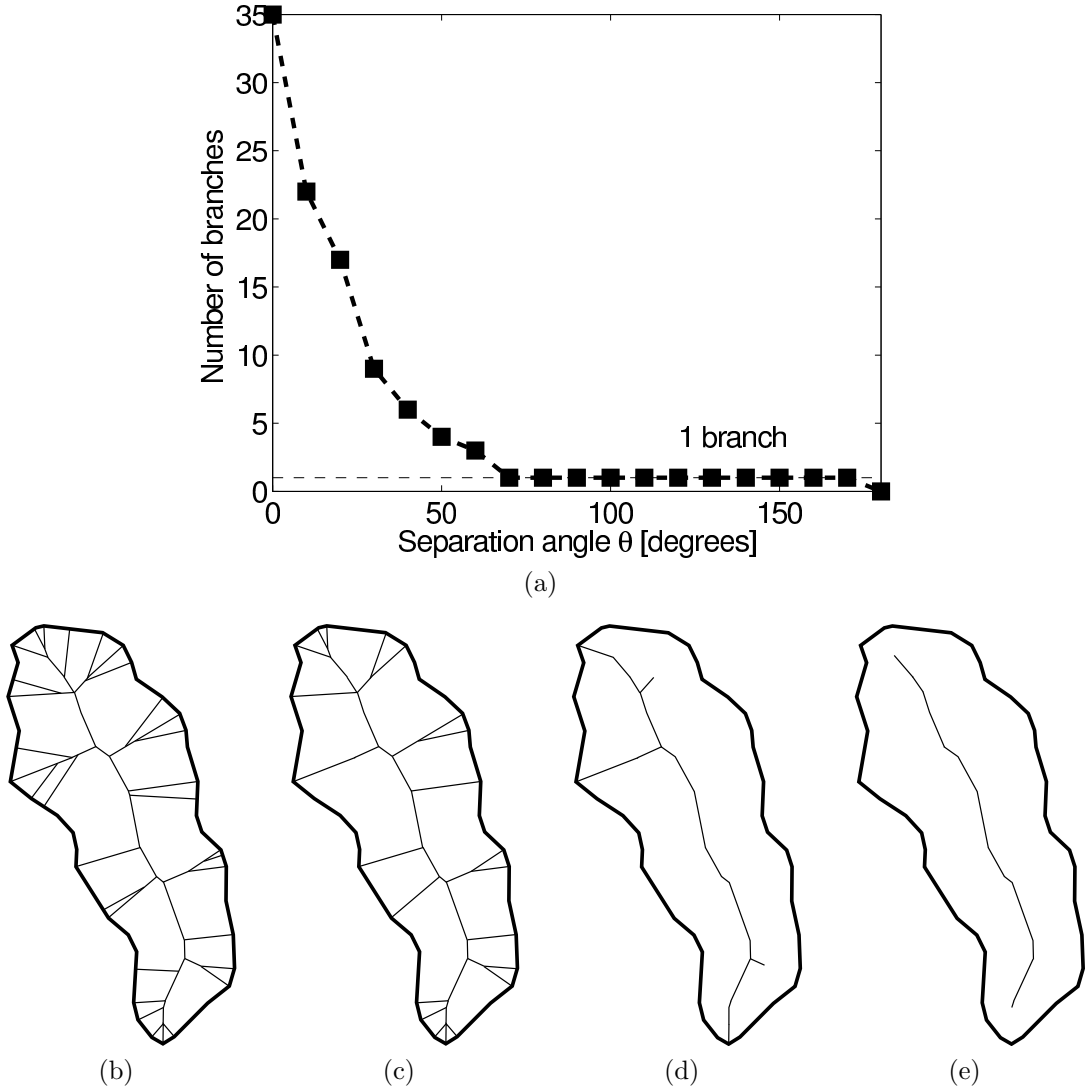

Figure 4.10: Single-edge notched beam. (a) Number of obtained branches with the $\theta-$SMA as a function of the value of θ and $\theta-$simplified medial axis obtained with (b) $\theta = 0°$, (c) $\theta = 10°$, (d) $\theta = 50°$ and (e) $\theta = 100°$.

of the predicted crack-path. Indeed, if a higher value of D^* is considered, a shorter crack-path is obtained, see for instance Figure 4.11(a). Hence, in such a case, the θ-SMA computation needs to be repeated more often during the numerical simulation.

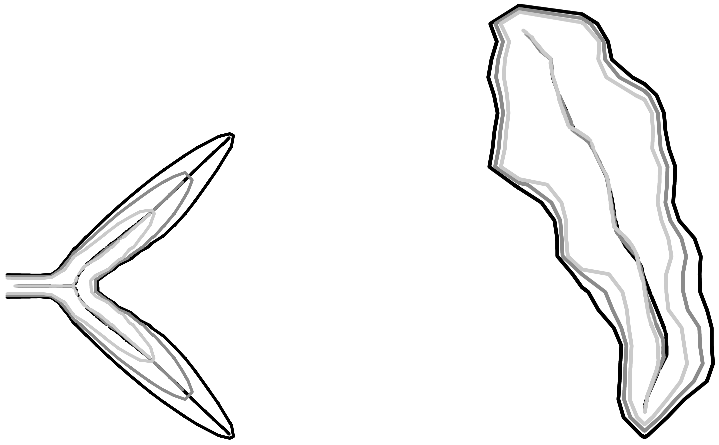

(a) (b)

Figure 4.11: Crack-path obtained with $D^* = 0.6$ (black), $D^* = 0.7$ (grey) and $D^* = 0.8$ (light grey) for (a) a square plate under mode I loading conditions and (b) a single-edge notched beam.

4.4 Numerical examples

In this section we present some numerical examples to illustrate the capabilities of the new continuous-discontinuous method. Both two- and three-dimensional examples are carried out.

Two-dimensional three-point bending test. To begin with, a two-dimensional three-point bending test is considered, see Figure 4.12. A uniform mesh of 1 640 (41×40) quadrilateral elements has been used. The main goal of this first analysis is to check whether the medial axis allows to predict the expected crack path.

The geometric and material parameters are summarised in Table 4.1. Here, the simplified Mazars damage model, see Equation (3.14), is considered. The exponential damage evolution law

$$D(Y) = 1 - \frac{Y_0}{Y} \exp\Big(-\beta(Y - Y_0)\Big) \tag{4.12}$$

with Y_0 the damage initiation state variable and β the slope of the stress-strain relation at the peak, is used.

The damage patterns and the force-displacement curves are shown in Figure 4.13. On the one hand, in Figure 4.13(a), both the force-displacement curves obtained with a continuous and with a combined strategy are plotted. As expected, since the crack

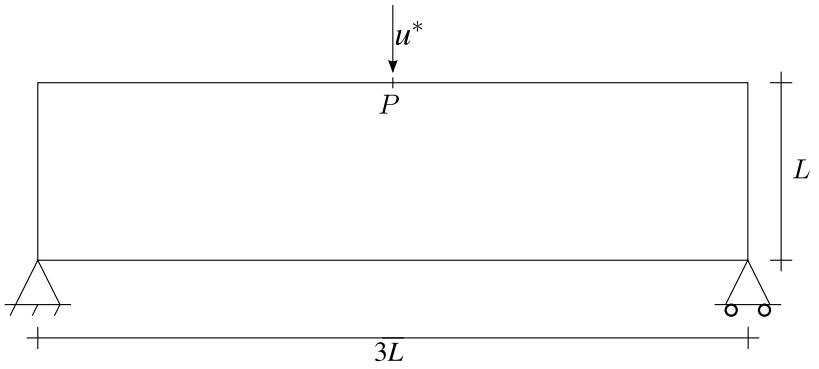

Figure 4.12: Three-point bending test: problem statement.

Table 4.1: Three-point bending test: geometrical and material parameters.

Meaning	**Symbol**	**Value**
Length of the beam	L	300 mm
Height of the beam	h	100 mm
Young's modulus	E	30 000 MPa
Damage initiation state variable	Y_0	10^{-4}
Slope of the stress-strain relation	β	121.93
Poisson's ratio	ν	0.00

is introduced when damage is close to one, the energy dissipated by a continuous-discontinuous approach with a traction-free crack is similar to the energy dissipated by a continuous model. On the other hand, Figures 4.13(b)-4.13(g) show the obtained results in terms of damage and deformation patterns (amplified by a factor of 100) for some increasing imposed displacements u^*. Firstly, the continuous gradient-enhanced damage model with smoothed displacements is used. A characteristic length $\ell = 0.01$ mm is considered. As seen in Figures 4.13(b)-4.13(c), the non-local regularisation technique allows to obtain physically realistic results. Secondly, as soon as a critical situation is achieved —the damage parameter at all the integration points in a finite element is larger than $D_{\text{crit}} = 0.9999$— a traction-free discontinuity is introduced. As expected, see Figure 4.13(d), the crack is introduced in the middle of the beam. Then, the continuous-discontinuous approach is employed. In order to know the direction along which the traction-free crack propagates, the $\theta-$SMA is computed. As expected, see Figures 4.13(e)-4.13(g), by means of this geometric tool, a straight

crack propagating upwards is predicted.

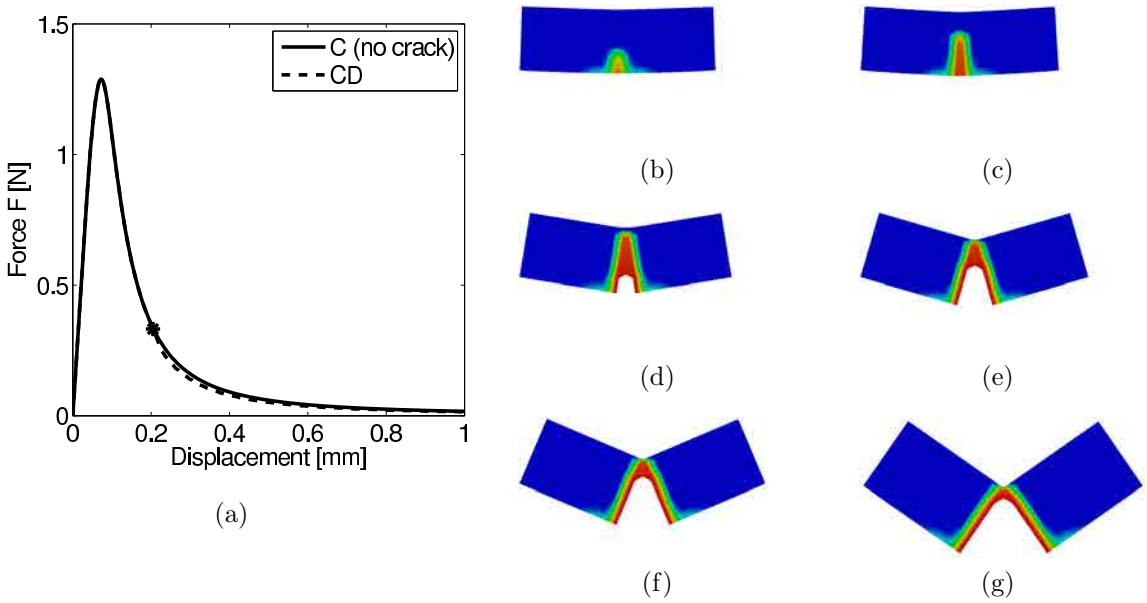

Figure 4.13: 2D three-point bending test, CD approach: for increasing imposed displacements u^*, damage and deformed patterns ($\times$ 100).

Three-dimensional three-point bending test. As a second test, the previous example with a three-dimensional geometry, see Figure 4.14, is considered. A uniform mesh of 4 920 ($41 \times 40 \times 3$) eight-noded hexahedral elements has been used. The geometric and material parameters summarised in Table 4.1 are employed. Again, the simplified Mazars damage model, Equation (3.14), with an exponential evolution law, Equation (4.12), are used.

Figure 4.15 shows the obtained results in terms of force-displacement curves, damage and deformation patterns (amplified by a factor of 100) for some increasing imposed displacements u^*. As shown, analogous results to the two-dimensional ones are obtained: the simplified medial surface allows to locate the crack where expected.

Four-point bending beam. As a third example, the four-point bending beam numerically analysed in Cervera et al. (2011) is reproduced, see Figure 4.16. In view of the central symmetry of the problem, only one half of the specimen has been discretised. A non-uniform mesh of 4 888 quadrilateral elements has been used. The material parameters are summarised in Table 4.2.

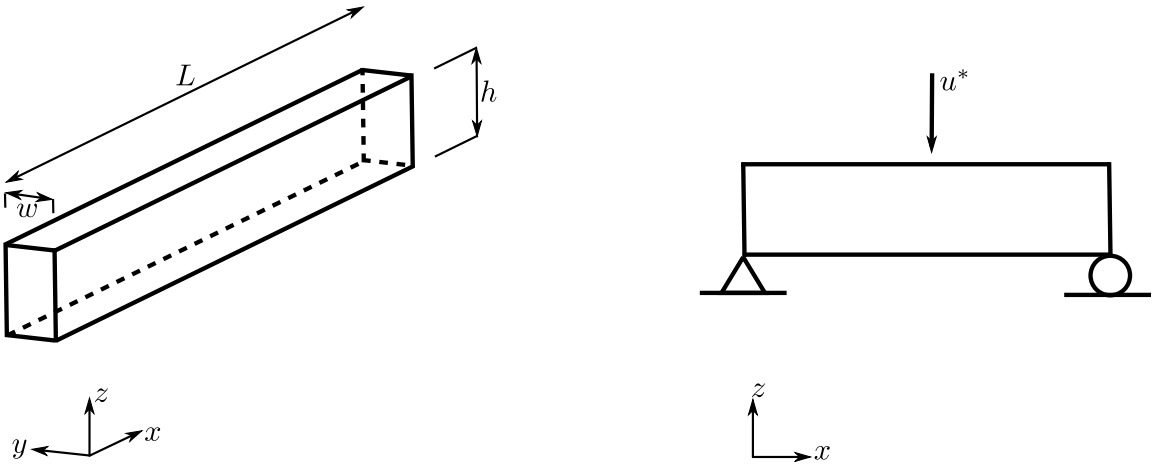

Figure 4.14: Three-point bending test: problem statement.

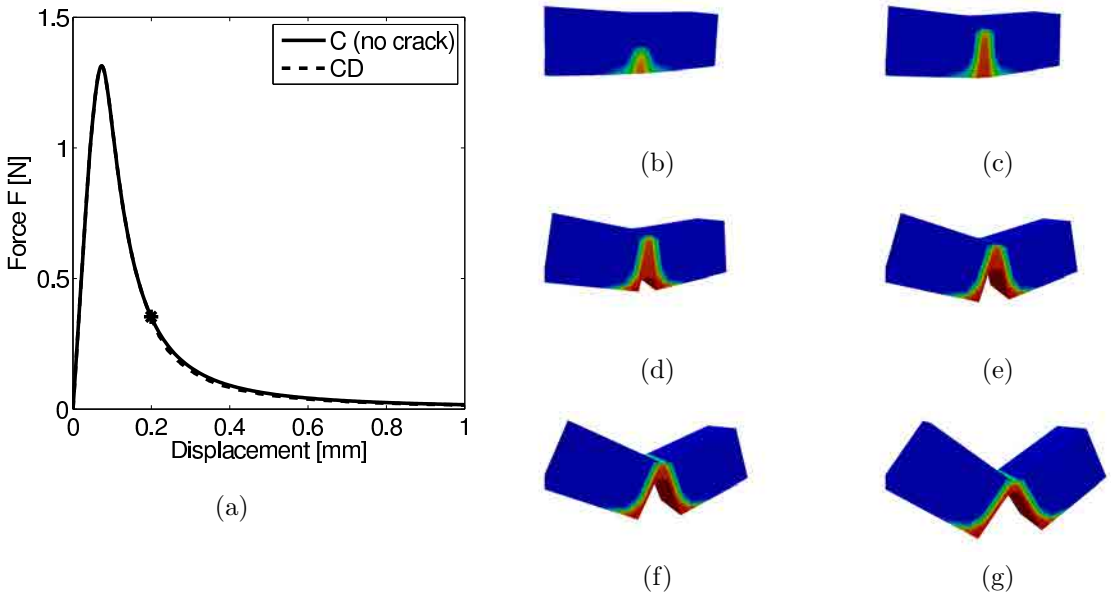

Figure 4.15: 3D three-point bending test, CD approach: for increasing imposed displacements u^*, damage profiles and deformed patterns ($\times$ 100).

Here, the truncated Rankine damage model, see Equation (3.16), and an exponential damage evolution law, see Equation (3.17), are considered.

For some increasing imposed displacements u^*, force-displacement curves, damage and deformation patterns (amplified by a factor of 100) are shown in Figure 4.17. For convenience purposes, a close-up of the central damaged area is depicted. On the one

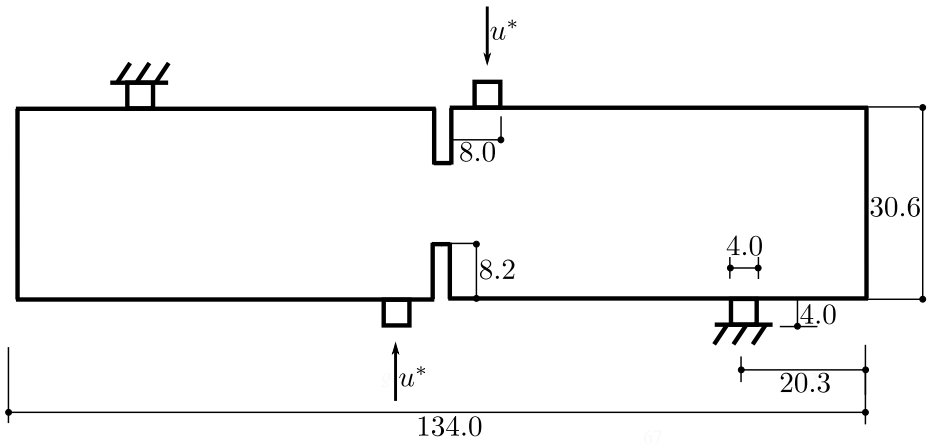

Figure 4.16: Four-point bending beam: problem statement (measures in centimetres).

Table 4.2: Four-point bending beam: material parameters.

Meaning	**Symbol**	**Value**
Young's modulus	E	30 GPa
Damage initiation equivalent effective stress	τ_0	2 MPa
Fracture energy	G	100 J/m^2
Poisson's ratio	ν	0.2
Characteristic length	ℓ	0.3 cm
Softening parameter	β	8.1×10^{-3} MPa^{-1}

hand, Figure 4.17(a) shows the obtained results in terms of force-displacement curves. As shown in the previous examples, since the traction-free crack is introduced when damage reaches a critical value $D_{\text{crit}} = 0.9999$, the energy dissipated by a combined approach is similar to the energy dissipated by a continuous model. On the other hand, as seen in Figures 4.17(b)-4.17(c), the continuous gradient-enhanced damage model with smoothed displacements is used for the first stages of the process. As soon as a critical situation is achieved, a crack that propagates through the middle of the regularised damaged bulk is introduced, see Figures 4.17(d)-4.17(g).

Single-edge notched beam. To finish with, the three-dimensional single-edge notched beam analysed in Section 3.4.2 is retrieved, see Figure 3.12. The same material parameters are used, see Table 3.6. Again, the modified von Mises model,

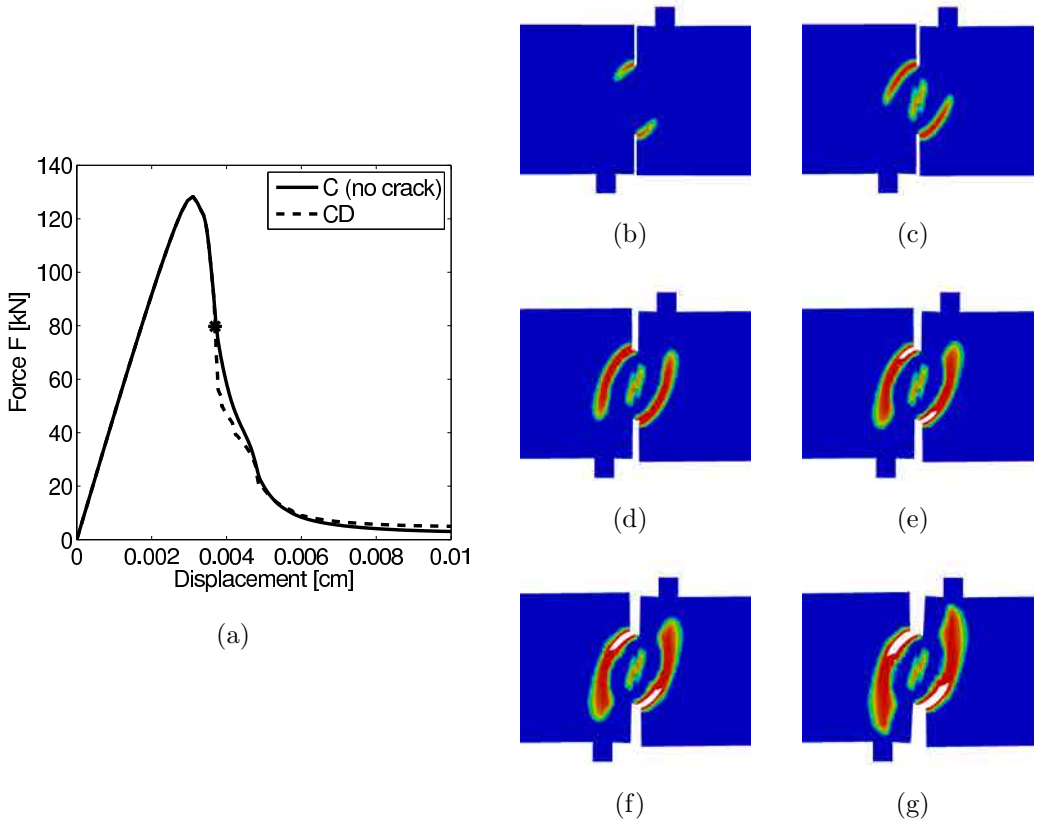

Figure 4.17: Four-point bending test, CD approach: for increasing imposed displacements u^*, damage profiles and deformed patterns ($\times$ 100).

see Equation (3.18), and the exponential damage evolution, see Equation (3.19), are considered. A non-uniform mesh of 407 eight-noded hexahedral elements has been used.

For some increasing imposed forces, force-displacement curves, damage and deformation patterns (amplified by a factor of 50) are shown in Figure 4.18. Here the traction-free crack is introduced when damage reaches a critical value $D_{\text{crit}} = 0.99$. On the one hand, as shown in Figure 4.18(a), the energy dissipated by a combined approach is similar to the energy dissipated by a continuous model. On the other hand, as seen in Figures 4.18(b)-4.18(g), the $\theta-$SMA (with $\theta = \frac{\pi}{2}$) allows to locate the traction-free crack through the middle of the damaged bulk also in a three-dimensional setting.

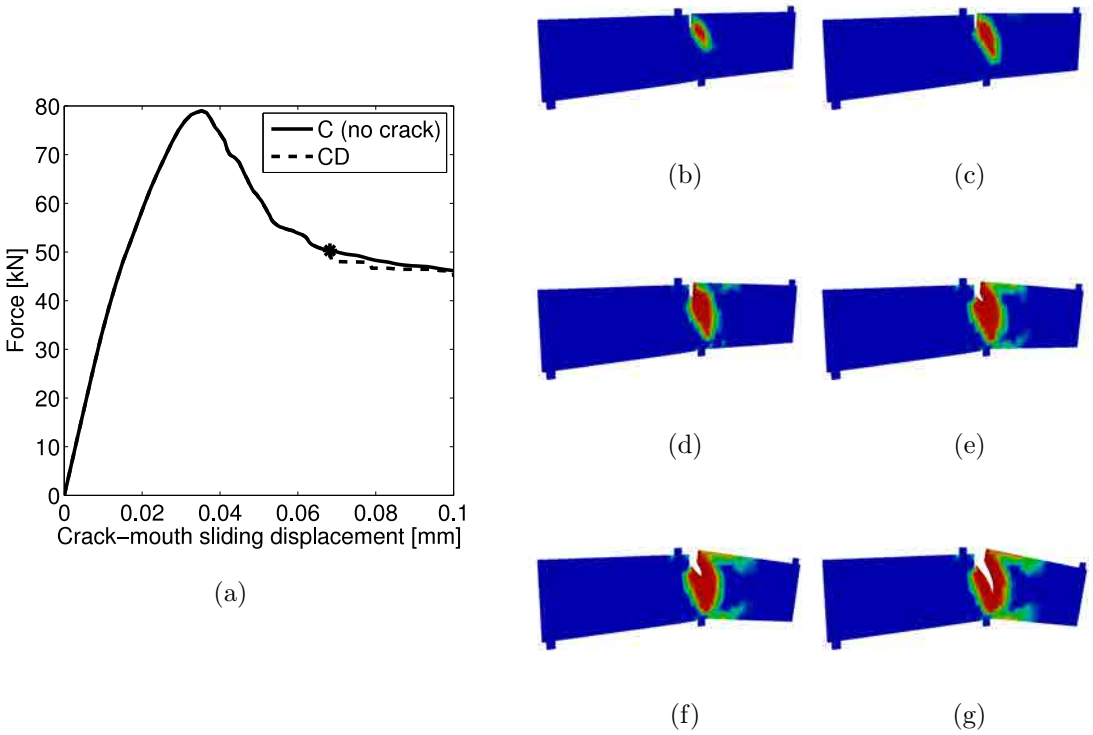

Figure 4.18: Single-edge notched beam, CD approach: for increasing imposed forces, damage profiles and deformed patterns ($\times$ 50).

4.5 Concluding remarks

In this chapter, a new continuous-discontinuous damage model is presented, see Figure 4.19. The key idea of this new approach is to couple a gradient-enriched formulation with an extended finite element approach thus enabling to simulate the entire fracture process —from formation of micro-cracks to the possible development of macro-cracks. This new combined strategy is characterised by the following features:

- In order to describe the first stages of the failure process, a gradient-enriched continuous formulation is used. Here, smoothed displacements are used to regularise the continuous bulk, see Chapter 3.

- At the end of each time step, the approach checks if the damage parameter is equal to a critical value $D_{\text{crit}} \simeq 1$ in an element located on the boundary of the mesh. In such a case, a traction-free crack is introduced.

- The discrete crack is introduced into the model according to the eXtended Finite Element Method (X-FEM). Hence, both the standard displacement field $\boldsymbol{u}$ and the gradient-enhanced displacement field $\widetilde{\boldsymbol{u}}$ are enriched with discontinuous functions satisfying the partition of unity concept. In particular, the sign function is used.

- The direction of propagation is determined by means of the already formed damage field. In particular, the traction-free crack propagates following the direction dictated by the $\theta-$ simplified medial axis (in 2D) or the $\theta-$simplified medial surface (in 3D) of the domain $D(\boldsymbol{x}) = D^*$. Neither choosing the value of the separation angle θ nor the value of the isoline $D(\boldsymbol{x}) = D^*$ are critical issues. Indeed:

  - In this thesis, the $\theta-$simplified medial axis and the $\theta-$simplified medial surface are used to locate the crack through the middle of the damaged bulk. That is, their main goal is not to allow shape recognition or image reconstruction —their usual applications— but to avoid the spurious cracks emanating from the main crack. Hence, θ should be large enough to capture only the main discontinuity. In the presented examples, with $\theta > \frac{\pi}{2}$, the main crack is obtained.
  - As seen in the presented numerical tests, if the damage field is smooth enough, the same qualitative results are obtained with different values of D^*.

  It is noted that, since the damaged bulk is regularised, the damage band —and thus the crack path— do not depend on the finite element mesh. Nevertheless, for computational convenience, the crack is let to propagate so that the tip always belongs to an element side.

- Analogously to the continuous model, smoothed displacements are attractive from a computational viewpoint in the combined formulation. Indeed, linearisation of the regularisation equations leads to a tangent block matrix, see Equation (4.9). In order to compute it, different matrices are needed: the standard $\mathbf{M}$ and the enhanced $\mathbf{M}_\psi$ mass matrices and the standard $\mathbf{D}$ and the enhanced $\mathbf{D}_\psi$ diffusivity matrices. The standard $\mathbf{M}$ and $\mathbf{D}$ matrices, already obtained

in Rodríguez-Ferran et al. (2005) are constant. However, the enhanced matrices may change during the numerical simulation, since the crack propagates through the continuous bulk.

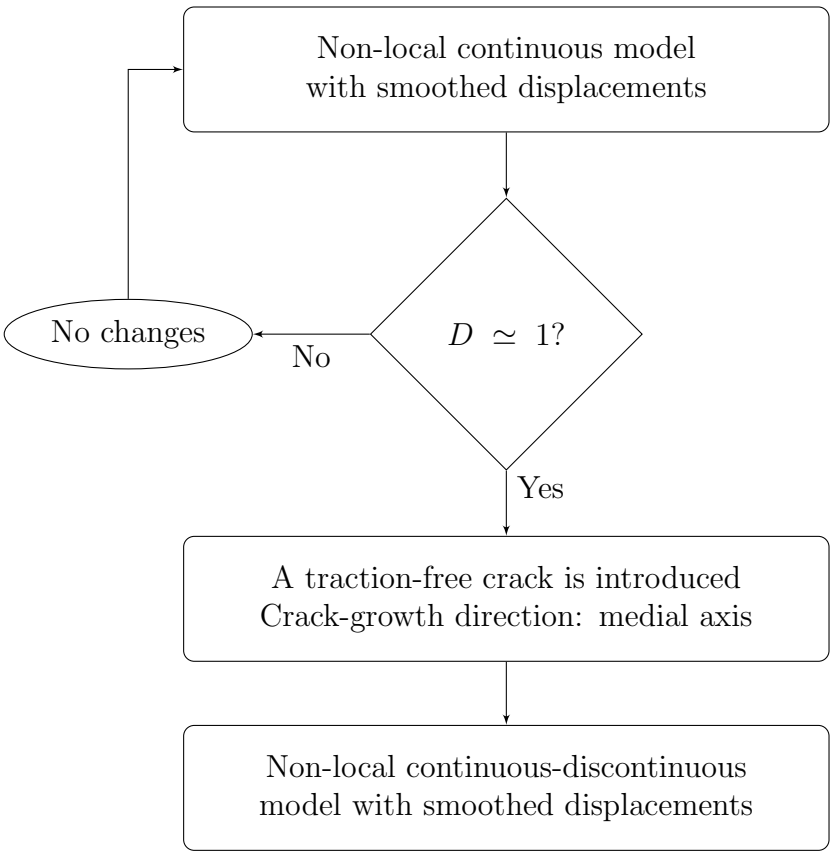

Figure 4.19: Proposed continuous-discontinuous model.

The proposed approach is tested on different two- and three-dimensional examples that illustrate that this combined methodology is able to deal with damage growth and material separation. The main results are:

- Both the medial axis and the medial surface allow to determine the direction of crack growth.
- The transition from a continuous to a continuous-discontinuous failure description with traction-free cracks is energetically consistent if it takes place when damage reaches a critical value $D_{\text{crit}} \simeq 1$. Therefore, the force-displacement

curves obtained with the proposed continuous-discontinuous strategy are similar to the curves obtained with a fully continuous description.

- Nevertheless, introducing a crack when $D_{\text{crit}} \simeq 1$ may be very restrictive, since the elements with high damage —but lower than D_{crit}— are not cracked. Therefore, a continuous-discontinuous description with $D_{\text{crit}} < 1$ may be suitable for many applications thus leading to the need of introducing cohesive cracks, see Chapter 5.

4.6 Future work

The work carried out in this chapter leaves some open research lines that need to be addressed in the near future.

Extension of the existing code to include multiple non-intersecting cracks. In this thesis, problems involving one single crack propagating through the continuous bulk are analysed. Nevertheless, for some numerical tests (see for instance the four-point bending beam of Section 4.4 if no central symmetry is assumed), it is necessary to deal with n non-intersecting discontinuities ($n > 1$).

Since the medial axis is able to locate n cracks when the condition $D(\boldsymbol{x}) = D^*$ results in n isolines, see Figure 4.20, the only change needed in the proposed strategy is the further extension of the finite element approximation. Indeed, if a body $\bar{\Omega}$ is crossed by n non-intersecting cracks, both the standard $\boldsymbol{u}$ and the enhanced $\widetilde{\boldsymbol{u}}$ displacement fields can be decomposed as

$$\boldsymbol{u}(\boldsymbol{x}) \simeq \boldsymbol{u}^h(\boldsymbol{x}) = \mathbf{N}(\boldsymbol{x})\mathbf{u}^1 + \sum_{i=2}^{n+1} \psi_i(\boldsymbol{x})\,\mathbf{u}^i \tag{4.13a}$$

$$\widetilde{\boldsymbol{u}}(\boldsymbol{x}) \simeq \widetilde{\boldsymbol{u}}^h(\boldsymbol{x}) = \mathbf{N}(\boldsymbol{x})\widetilde{\mathbf{u}}^1 + \sum_{i=2}^{n+1} \psi_i(\boldsymbol{x})\,\widetilde{\mathbf{u}}^i \tag{4.13b}$$

where $\mathbf{u}^i$ and $\widetilde{\mathbf{u}}^i$, $\forall\, i = 1 \div n+1$, are continuous functions on $\bar{\Omega}$ and ψ_i are sign functions centred at the discontinuity surface Γ_i.

Crack branching. As discussed in Section 4.3.1, see Figure 4.7, the medial axis allows to capture crack branching. Nevertheless, in order to take into account branched and intersecting discontinuities, the X-FEM should be further enhanced.

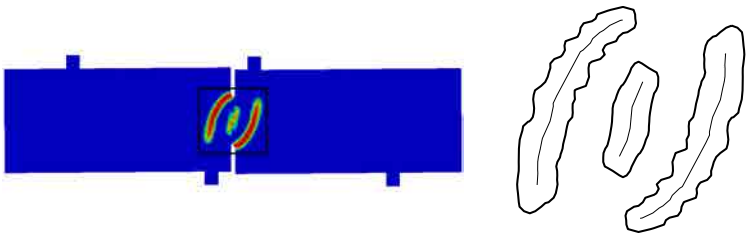

(a) (b)

Figure 4.20: Four point bending test: (a) given a damage profile where the condition $D(\boldsymbol{x}) = D^*$ ($D^* = 0.2$) results in three isolines, (b) the $\theta-$simplified medial axis allows to locate three cracks (close-up of the central zone).

Different enrichments may be used. On the one hand, Daux et al. (2000) propose a new discontinuous *junction* function that allows to account for a branched crack. On the other hand, as discussed by Zlotnik and Díez (2009) in the context of a $n-$phase flow problem, a hierarchical enrichment can be introduced.

Addition of crack tip functions to the finite element approximation. For the sake of simplicity, the crack tip has been assumed to belong to an element edge. Nevertheless, in a more general case, see Figure 4.21, the crack tip may lie within an element.

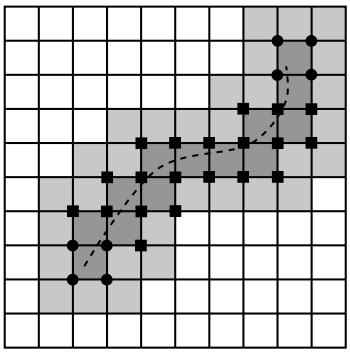

Figure 4.21: A crack line (dashed line) in a structured mesh with standard elements (white), elements whose nodes are all enriched (dark grey) and blending elements (light grey). Nodes enriched with the asymptotic crack tip functions and the sign function are indicated by circles and squares respectively. Adapted from Moës et al. (1999).

In such a case, the sign function ψ cannot adequately describe the discontinuity and asymptotic crack tip functions should be used to enrich the finite element

approximation, see Belytschko and Black (1999) and Stolarska et al. (2001).

Extension of the proposed method to simulate fracking. As discussed in Section 4.1, the explicit modelling of cracks allows to simulate different phenomena such as hydrofracturing, commonly known as fracking. By means of this technique, a mixture of water, sand and chemicals is injected at high pressure into a drill hole to create fractures thus allowing the extraction of fluids such as gas or petroleum. Hence, it would be interesting to use the proposed continuous-discontinuous strategy to model this phenomenon. In order to do it, we believe that few changes are needed, since the only extra term that needs to be accounted for is the fluid pressure.

Chapter 5

Continuous-discontinuous damage model: cohesive cracks via an energy-transfer process

---

In this chapter we extend the applicability of the combined strategy presented in Chapter 4 to cohesive cracks. For the early stages of the failure process, a gradient-enhanced model based on smoothed displacements is employed. As soon as the damage parameter exceeds a critical value ($D_{\text{crit}} < 1$) a cohesive crack is introduced. Our main concern is to define the cohesive law in such a way that the continuous and the continuous-discontinuous approaches are energetically equivalent. More specifically, a new criterion to determine the fracture energy not yet dissipated in the damaged bulk is proposed. This energy balance is tested on different examples to show that by means of this new criterion, a better approximation of the energy that has to be transferred to the cohesive crack is computed.

5.1 Introduction

Numerical simulation of failure of quasi-brittle materials is traditionally tackled from two different points of view: damage and fracture mechanics. As discussed in Chapter 4, reconciling these two theories is a way to achieve a better characterisation of the whole failure process.

An important issue concerning the switching from the continuum to the discrete approach to fracture is deciding when this transition takes place. In Chapter 4, the model switching occurs when the damage parameter in a finite element reaches a critical value $D_{\text{crit}} \simeq 1$. However, as discussed in Comi et al. (2007), if the damage parameter reaches values close to one, non-local interaction remains active even when the local strength tends to zero. Hence, an unrealistic spread of damage may occur.

In order to avoid this behaviour, model switching can be driven by a critical damage value D_{crit} less than 1. Nevertheless, this poses another problem: if a traction-free crack is introduced, see Chapter 4, conservation of energy is not ensured. Indeed, if $D_{\text{crit}} < 1$, the transition takes place when the material is not fully degraded and thus, some residual energy remains to be dissipated by the continuous strategy. Therefore, this remaining energy is not transferred to the combined strategy and the continuous and the continuous-discontinuous approaches are not energetically consistent.

One possible solution to this problem consists of introducing cohesive cracks. If cohesive discontinuities are introduced, see the pioneering works of Dugdale (1960) and Barenblatt (1962), separation occurs across an extended crack tip or a cohesive zone, see Figure 5.1(a). Thus, they are suitable to model any existing interaction between the two faces of the macroscopic crack. Such a situation occurs, for instance, in fibre-reinforced concrete structures, see Figure 5.1(b).

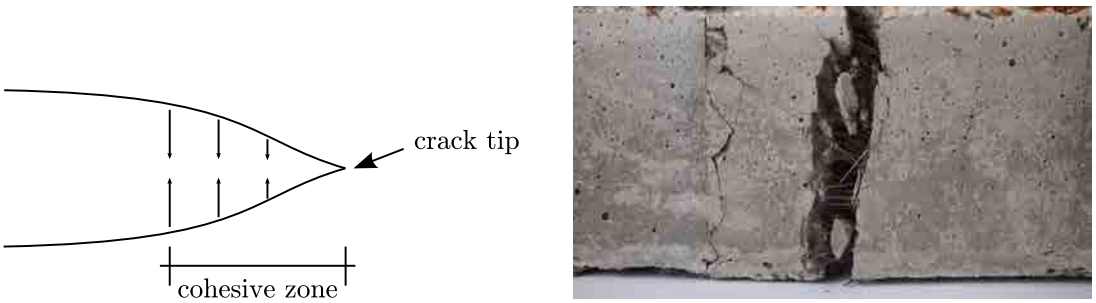

Figure 5.1: (a) A cohesive crack can be used to model (b) steel-fibre reinforced concrete beams (courtesy of Climent Molins, UPC).

In this chapter, we extend the applicability of the continuous-discontinuous strategy with traction-free cracks, see Chapter 4, to energetically equivalent cohesive cracks. Specifically, the main contributions of this chapter are:

1. **To propose a new combined formulation with cohesive cracks**. The

continuous-discontinuous strategy presented in Chapter 4 is extended to include cohesive cracks. In this new formulation, an implicit gradient-enhanced damage model based on smoothed displacements is used to simulate the initial stages of failure. As soon as a critical situation is achieved —damage parameter at all the integration points of a finite element exceeds a critical damage value $D_{\text{crit}} < 1$— a cohesive crack is introduced.

2. **To propose a new criterion to estimate the energy not yet dissipated by the bulk**. One important issue concerning the switching from damage to fracture —if cohesive cracks are introduced— is the definition of the cohesive law. One means of obtaining the properties of this law is by transferring to the cohesive crack the energy not yet dissipated by the bulk. Nevertheless, this poses a substantial difficulty: after the switching —from the continuous to the continuous-discontinuous strategy— the continuous model is no longer used. Hence, the energy that needs to be transferred is not known at model switching and needs to be estimated. In order to do it, different strategies may be used. Here, a new criterion is proposed. The actual unloading behaviour —either softening or secant-elastic— of each point in the continuous bulk is estimated. Thus, compared to other strategies where all the points in the damaged bulk are assumed to unload following the softening branch, the energy to be transferred is more accurately computed.

The structure of the chapter is as follows. In Section 5.2 the combined damage model with cohesive cracks is presented. Section 5.3 deals with the new criterion to determine the energy to be transferred to the cohesive crack. The capabilities of this new combined approach are illustrated by means of some numerical examples in two dimensions. Finally, the concluding remarks in Section 5.4 and the future directions in Section 5.5 close this chapter.

5.2 Gradient-enhanced damage model

As discussed in the previous chapter, see Section 4.2, as soon as a discontinuity is introduced, the bulk Ω is bounded by $\Gamma = \Gamma_u \cup \Gamma_t \cup \Gamma_d$, see Figure 5.2(a) and the problem fields are characterised by means of the X-FEM, see Equation (4.1).

In this chapter, the discontinuity is a cohesive crack. Its orientation is given by a unit vector $\boldsymbol{n}$ perpendicular to the discontinuity surface. By means of this vector, the two faces of the discontinuity Γ_d^+ and Γ_d^- can be distinguished, see Figure 5.2(b).

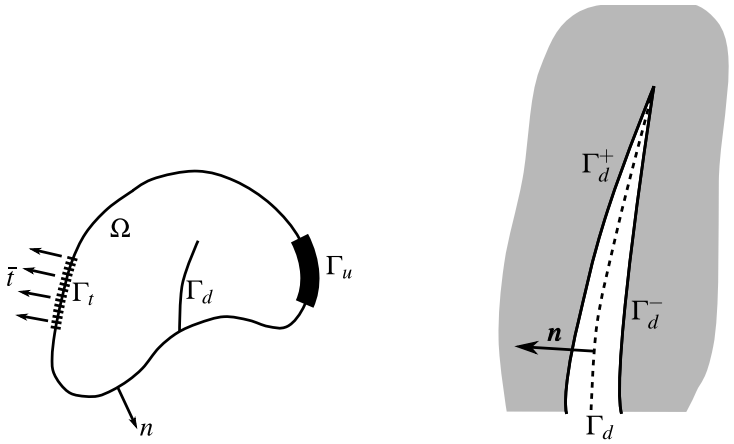

Figure 5.2: (a) Notations for a body with a crack subjected to loads and imposed displacements. (b) Notations for the cohesive crack.

5.2.1 Governing equations

The strong form of the equilibrium equation and boundary conditions for the body $\bar{\Omega} = \Omega \cup \Gamma$ without body forces and a cohesive discontinuity Γ_d is given by

$$\nabla \cdot \boldsymbol{\sigma} = \mathbf{0} \quad \text{in } \Omega \tag{5.1a}$$

$$\boldsymbol{\sigma} \cdot \boldsymbol{n} = \bar{\boldsymbol{t}} \quad \text{on } \Gamma_t \tag{5.1b}$$

$$\boldsymbol{\sigma} \cdot \boldsymbol{n} = \bar{\boldsymbol{t}}_d \quad \text{on } \Gamma_d \tag{5.1c}$$

$$\boldsymbol{u} = \boldsymbol{u}^* \quad \text{on } \Gamma_u \tag{5.1d}$$

where $\boldsymbol{\sigma}$ is the Cauchy stress tensor, $\boldsymbol{u}^*$ is a prescribed displacement on the Dirichlet boundary, $\bar{\boldsymbol{t}}$ is the traction on the Neumann boundary, $\bar{\boldsymbol{t}}_d$ is the traction on the discontinuity surface and $\boldsymbol{n}$ is the outward unit normal to the body. Note that equation (5.1c) represents traction continuity at the discontinuity surface Γ_d.

The cohesive tractions are considered to be a function of the crack opening $[\![\boldsymbol{u}]\!]$, defined as the difference between $\boldsymbol{u}^+$ and $\boldsymbol{u}^-$, where $\boldsymbol{u}^+ = \boldsymbol{u}_{\Gamma_d^+}$ and $\boldsymbol{u}^- = \boldsymbol{u}_{\Gamma_d^-}$. That is

$$[\![\boldsymbol{u}]\!] = \boldsymbol{u}^+ - \boldsymbol{u}^- \qquad \text{on } \Gamma_d \tag{5.2}$$

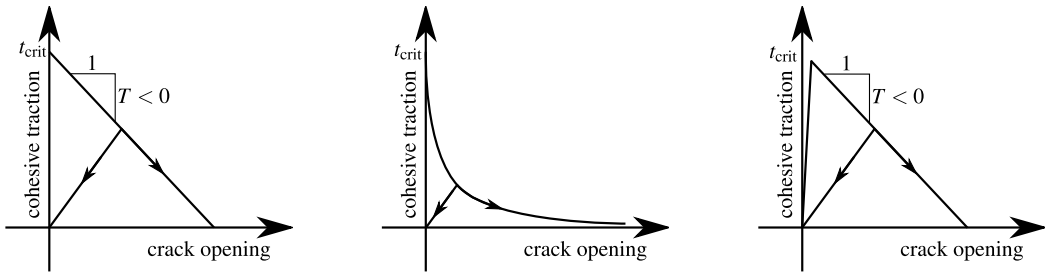

Figure 5.3: Typical one-dimensional cohesive models: (a) initially rigid linear cohesive model, (b) initially rigid exponential cohesive model, (c) initially elastic linear cohesive model. Adapted from Rabczuk (2013).

Different cohesive models can be found in the literature. As reviewed by Rabczuk (2013), both initially rigid and initially elastic models can be considered. On the one hand, initially rigid models are based on a monotonic decrease in the cohesive traction, see Figures 5.3(a) and 5.3(b). On the other hand, initially elastic models are characterised by an initial positive slope, see Figure 5.3(c). In this chapter, only initially rigid models are considered, since the increase in the cohesive traction of initially elastic models may lead to an increase of the neighbouring stresses and thus, to spurious cracking.

The equilibrium equation is first cast in a weak form to be subsequently linearised. Following standard procedures, see Appendix A for details, equation (5.1) leads to

$$\int_{\Omega} \nabla^s \boldsymbol{\omega}^1 : \boldsymbol{\sigma} \, \mathrm{d}\Omega = \int_{\Gamma_t} \boldsymbol{\omega}^1 \cdot \bar{\boldsymbol{t}} \, \mathrm{d}\Gamma \qquad \forall \boldsymbol{\omega}^1 \in H^1(\Omega) \quad (5.3a)$$

$$\int_{\Omega} \psi \nabla^s \boldsymbol{\omega}^2 : \boldsymbol{\sigma} \, \mathrm{d}\Omega + 2 \int_{\Gamma_d} \boldsymbol{\omega}^2 \cdot \bar{\boldsymbol{t}}_d \, \mathrm{d}\Gamma = \int_{\Gamma_t} \psi \boldsymbol{\omega}^2 \cdot \bar{\boldsymbol{t}} \, \mathrm{d}\Gamma \qquad \forall \boldsymbol{\omega}^2 \in H^1(\Omega) \quad (5.3b)$$

It is noted that equation (5.3a) was already obtained in Chapter 4 when dealing with traction-free cracks, while in equation (5.3b) an extra term regarding the cohesive forces appears.

Regarding the regularisation of the bulk, smoothed displacements are employed. Hence, combined boundary conditions are prescribed for the continuous displacement fields $\widetilde{\boldsymbol{u}}^1$ and $\widetilde{\boldsymbol{u}}^2$, see Equation (4.3), thus leading to the same two weak statements of Chapter 4, see Equation (4.5).

5.2.2 Linearisation and consistent tangent matrix

The discrete format of the equilibrium equation, see Equations (5.3), leads to the governing equations

$$\int_\Omega \mathbf{B}^T \boldsymbol{\sigma}\, \mathrm{d}\Omega = \int_{\Gamma_t} \mathbf{N}^T \bar{\boldsymbol{t}}\, \mathrm{d}\Gamma \tag{5.4a}$$

$$\int_\Omega \psi \mathbf{B}^T \boldsymbol{\sigma}\, \mathrm{d}\Omega + 2\int_{\Gamma_d} \mathbf{N}^T \bar{\boldsymbol{t}}_d\, \mathrm{d}\Gamma = \int_{\Gamma_t} \psi \mathbf{N}^T \bar{\boldsymbol{t}}\, \mathrm{d}\Gamma \tag{5.4b}$$

As discussed in Section 4.2.2, the regularisation equation leads to the governing equations (4.8).

Therefore, the only difference between introducing a traction-free crack and a cohesive crack is the second term in the LHS of Equation (5.4b). Indeed, if traction-free cracks are introduced, $\bar{\boldsymbol{t}}_d = \mathbf{0}$. Nevertheless, if a cohesive crack is considered,

$$\dot{\bar{\boldsymbol{t}}}_d = \boldsymbol{f}\left(\llbracket \dot{\boldsymbol{u}} \rrbracket\right) \tag{5.5}$$

with $\boldsymbol{f}$ relating traction rate $\dot{\bar{\boldsymbol{t}}}_d$ and displacement jump rate $\llbracket \dot{\boldsymbol{u}} \rrbracket$.

Linearisation of Equations (5.4) and (4.8) leads to the consistent tangent matrix

$$\mathbf{K}_{\tan} = \begin{bmatrix} \mathbf{K}_{\mathrm{sec}} & \mathbf{K}_{\psi,\mathrm{sec}} & \mathbf{K}_{\mathrm{loc}} & \mathbf{K}_{\psi,\mathrm{loc}} \\ \mathbf{K}_{\psi,\mathrm{sec}} & \mathbf{K}_{\mathrm{sec}} + \mathbf{K}_{\mathrm{cohesion}} & \mathbf{K}_{\psi,\mathrm{loc}} & \mathbf{K}_{\mathrm{loc}} \\ -(\mathbf{M} + \ell^2 \mathbf{K}_{\mathrm{BC}}) & -(\mathbf{M}_\psi + \ell^2 \mathbf{K}_{\psi,\mathrm{BC}}) & \mathbf{M} + \ell^2 \mathbf{D} & \mathbf{M}_\psi + \ell^2 \mathbf{D}_\psi \\ -(\mathbf{M}_\psi + \ell^2 \mathbf{K}_{\psi,\mathrm{BC}}) & -(\mathbf{M} + \ell^2 \mathbf{K}_{\mathrm{BC}}) & \mathbf{M}_\psi + \ell^2 \mathbf{D}_\psi & \mathbf{M} + \ell^2 \mathbf{D} \end{bmatrix}, \tag{5.6}$$

with matrices defined in Section 4.2.2. That is, the only difference between introducing a traction-free crack and a cohesive crack is the cohesive matrix $\mathbf{K}_{\mathrm{cohesion}}$. Indeed, if traction-free cracks are considered, $\mathbf{K}_{\mathrm{cohesion}} = \mathbf{0}$ whereas if cohesive cracks are introduced,

$$\mathbf{K}_{\mathrm{cohesion}} = 2\int_\Omega \mathbf{N}^T \frac{\partial \bar{\boldsymbol{t}}_d}{\partial \mathbf{u}^2} \mathrm{d}\Omega \tag{5.7}$$

5.3 Energy balance to determine the cohesive law

One important issue concerning the transition from a continuous approach to cohesive cracks is the description of the cohesive law. One means of obtaining the properties of this traction-displacement relation is by enforcing that the energy not yet dissipated by the bulk when switching models is transferred to the cohesive crack. This idea

inspired the *equivalent crack concept*, see Mazars and Pijaudier-Cabot (1996), and has been used in some combined approaches, see Comi et al. (2007), Cazes et al. (2009) and Cuvilliez et al. (2012).

The strategy here proposed is based on the same idea. That is, the energy dissipated with a continuous model, Ψ_C, and with a continuous-discontinuous model, Ψ_{CD}, are prescribed to be equal:

$$\Psi_C = \Psi_{CD} \tag{5.8}$$

It is noted that, at model switching, the analysis with the continuous model is interrupted and replaced by the continuous-discontinuous strategy. Therefore, without a reference continuous simulation, Ψ_C is not known and needs to be estimated.

The key idea of our new strategy is the way the energy dissipated by the continuous model Ψ_C is computed. For the sake of clarity, this new proposal is first discussed by means of a one-dimensional problem, see Section 5.3.1. Then, the extension to multidimensional settings is considered, see Section 5.3.2.

5.3.1 Energy balance for a uniaxial tension test

The proposed energy balance is first discussed by means of a uniaxial tension test, see Figure 5.4(a).

The one-dimensional particularisations of the damage model with smoothed displacements, see Table 3.1, with $Y(\varepsilon) = \varepsilon$ and a linear softening law, see Equation (3.15) and Figure 5.4(b), are used.

A central part of the bar is weakened (10% reduction in Young's modulus) to trigger localisation. A uniform mesh of 105 elements is considered and the geometric and material parameters are summarised in Table 5.1. The numerical tests are displacement-controlled.

Local continuum damage model. To begin with, a local damage model is considered. First, a continuous simulation is carried out. The results are shown in Figure 5.5.

On the one hand, Figure 5.5(a) shows the force-displacement curve. It is noted that it exhibits the two expected branches. Indeed, since in the first load increments

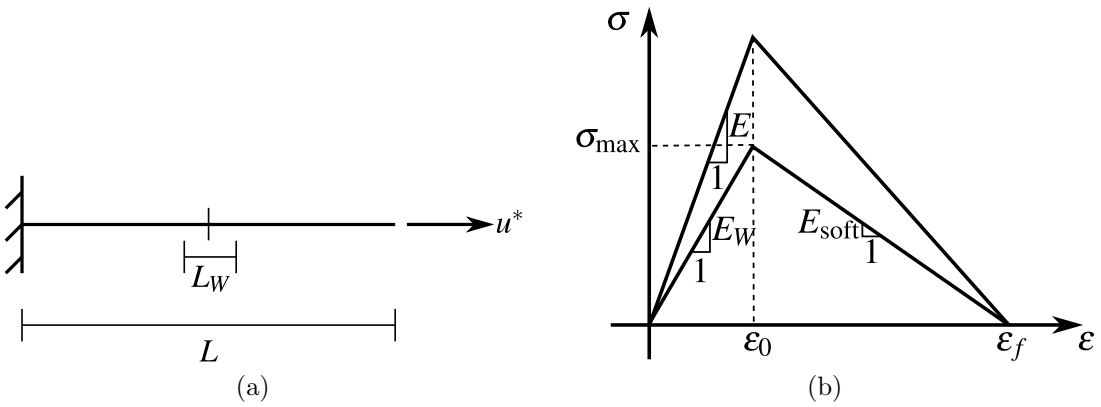

Figure 5.4: Uniaxial tension test: (a) problem statement; (b) linear softening law.

Table 5.1: Uniaxial tension test: geometrical and material parameters.

Meaning	**Symbol**	**Value**
Length of the bar	L	100 mm
Length of the weaker part	L_W	14 mm
Cross-section of bar	A	1 mm^2
Young's modulus	E	20 000 MPa
Young's modulus of the weaker part	E_W	18 000 MPa
Damage initiation state variable	ε_0	10^{-4}
Final state variable	ε_f	1.25×10^{-2}

the strain is lower than ε_0 in all the bar, a first elastic branch with positive slope

$$\frac{\Delta F}{\Delta u} = \frac{1}{\frac{L-L_W}{E} + \frac{L_W}{E_W}} = 196.88 \text{ N/mm} \tag{5.9}$$

is observed. Once the strain reaches the damage initiation threshold in the weakened part, all points in L_W unload following the softening branch. Due to equilibrium, the rest of the bar unloads following the elastic branch thus leading to a force-displacement curve with negative slope

$$\frac{\Delta F}{\Delta u} = \frac{1}{\frac{L-L_W}{E} + \frac{L_W}{E_{\text{soft}}}} = -10.62 \text{ N/mm} \tag{5.10}$$

where $E_{\text{soft}} = \frac{\sigma_{\max}}{\varepsilon_0 - \varepsilon_f}$, with $\sigma_{\max} = E_W \varepsilon_0$.

On the other hand, Figure 5.5(b) shows the damage profiles D. Due to locality, the width of the damage profile λ_D is equal to the length of the weakened part L_W. In

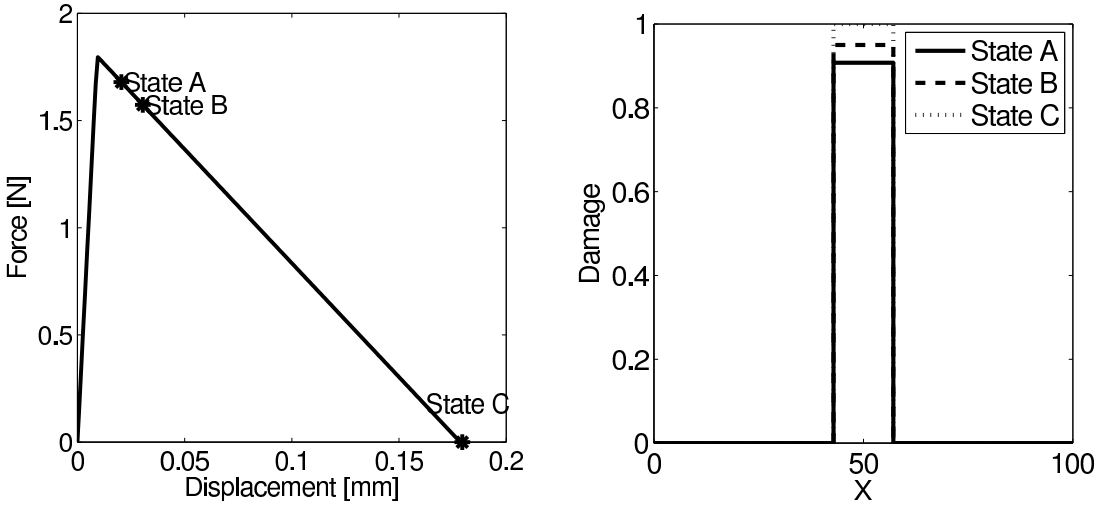

(a) (b)

Figure 5.5: Uniaxial tension test (continuous strategy with a local damage model): (a) force-displacement curves; (b) damage profiles.

addition, since a continuous strategy is used from the beginning to the end of failure, the damage parameter reaches a maximum value equal to 1, see the State C in Figure 5.5(b).

Let us now consider that as soon as damage reaches a critical value $D_{\text{crit}} = 0.9$ (the state A shown in Figure 5.5), a cohesive crack is introduced at $x = \frac{L}{2}$ and the proposed continuous-discontinuous strategy is used. This model switching —from the continuous to the combined strategy— entails two main changes.

First, damage is fixed to D_{crit} in all points in L_W. Hence, from that moment on, all these points unload following the secant unloading branch with slope $E_W\,(1 - D_{\text{crit}})$, see Figure 5.6(a), while the rest of the bar unloads following the elastic branch with slope E, see Figure 5.6(b).

Second, after the switching, no more energy dissipation in the bulk occurs, since all points unload elastically. In other words, the energy dissipated by the bulk if a combined technique is used is the energy already dissipated in the bulk at model switching. Therefore, in order to ensure energy consistency —that is, continuous and continuous-discontinuous strategy should dissipate the same amount of energy— the energy not yet dissipated by the bulk (when switching models) needs to be transferred to the cohesive crack. If a local damage model is employed, this quantity, see Figure 5.7(a), can be exactly computed. Indeed, recalling first that the cross-section of the

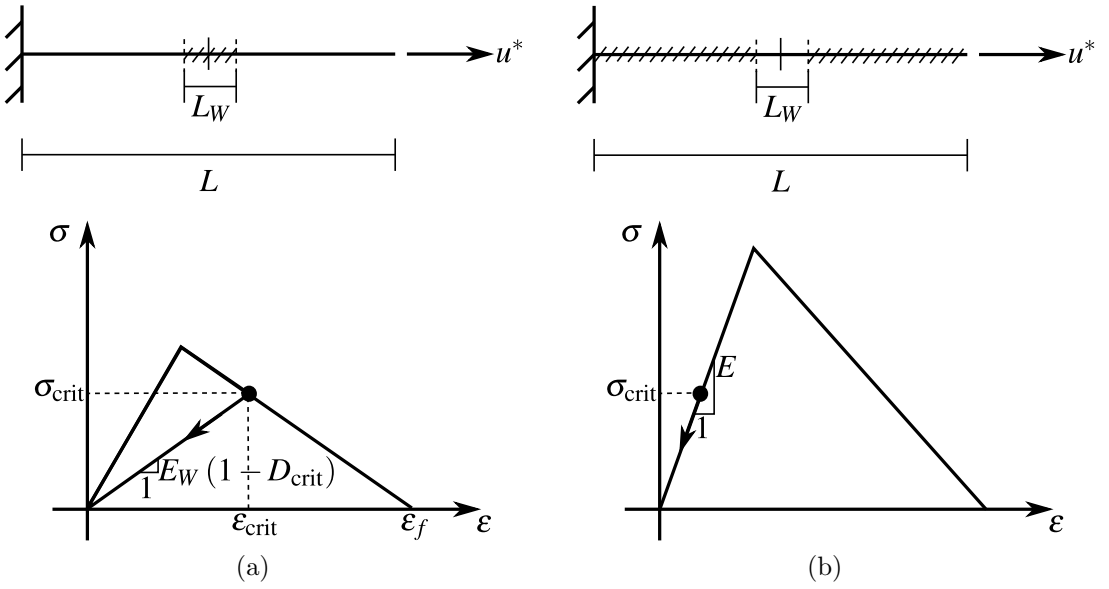

Figure 5.6: Once damage reaches a critical value, the model switching is carried out. Hence, (a) points in L_W unload following the secant unloading branch with slope $E_W\,(1 - D_{\text{crit}})$ while (b) the rest of the bar unloads following the elastic branch with slope E.

bar is $A = 1$ mm^2, the equivalence $\sigma \equiv F$ holds. Thus, for each point of the bar, the energy not yet dissipated is (at model switching) a known quantity. First, due to the elastic response, outside the damaged zone, this quantity is

$$\psi_C = 0 \tag{5.11}$$

Second, for each point in L_W, the energy not yet dissipated is equal to

$$\psi_C = \frac{1}{2}\sigma_{\text{crit}}\varepsilon_{\text{crit}} + \frac{1}{2}\sigma_{\text{crit}}\left(\varepsilon_f - \varepsilon_{\text{crit}}\right) = \frac{1}{2}\sigma_{\text{crit}}\varepsilon_f, \tag{5.12}$$

see Figure 5.7(b). Therefore the total amount of energy that needs to be transferred to the cohesive crack is

$$\Psi_{\text{transfer}} = L_W \frac{1}{2}\sigma_{\text{crit}}\varepsilon_f. \tag{5.13}$$

Since the unloading behaviour of the damage model is linear, it is natural to enforce the same behaviour for the cohesive law. Therefore, a linear traction-separation law with slope T is considered, see Figure 5.8. Then, the exact value of T is obtained by prescribing that the energy not yet dissipated by the bulk at model switching, see

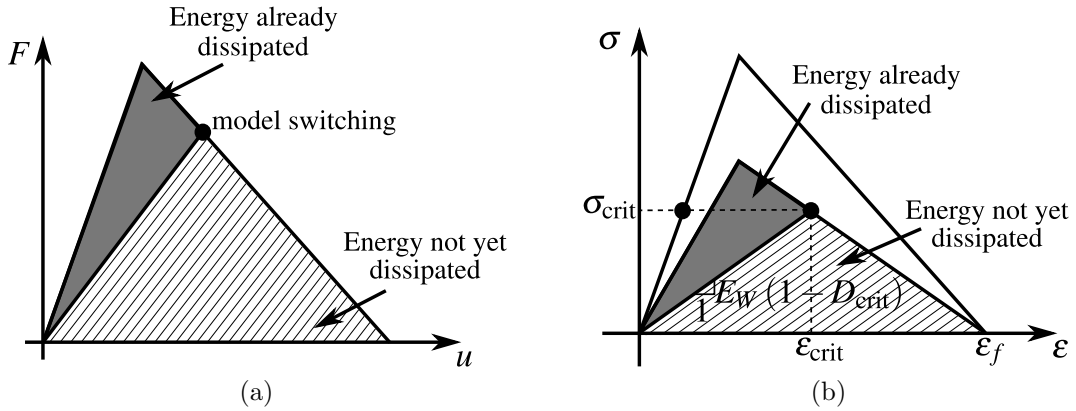

Figure 5.7: (a) The energy that needs to be transferred to the crack (striped area) can be exactly computed due to the local behaviour of the solution. (b) Outside the damaged zone, this quantity is 0, while for each point inside L_W, this quantity is $\frac{1}{2}\sigma_{\text{crit}}\varepsilon_f$.

Equation (5.13), is transferred to the crack. Thus,

$$T = -\frac{\sigma_{\text{crit}}}{L_W \varepsilon_f} = -9.40 \text{ N/mm}^3 \tag{5.14}$$

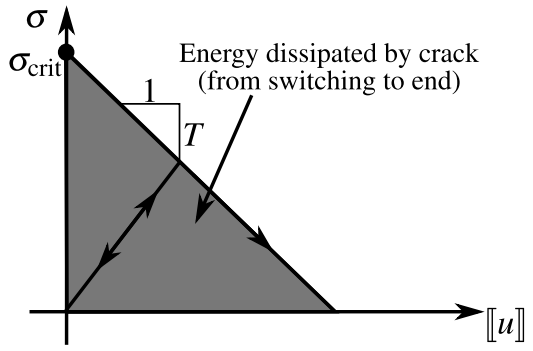

Figure 5.8: If a linear traction-separation law is considered, the energy dissipated by the crack (area under the $\sigma - [\![u]\!]$ curve) is $-\frac{\sigma^2_{\text{crit}}}{2T}$.

The results for the continuous and the combined strategies are shown in Figure 5.9. As shown in Figure 5.9(a), the two strategies are energetically equivalent. Indeed, the force-displacement curve obtained with the combined strategy overlaps the curve obtained with the continuous approach. The difference between these two strategies can be seen in Figure 5.9(b). On the one hand, if a continuous strategy is employed,

the damage profile reaches a maximum value equal to 1. On the other hand, if a combined strategy is used, damage is fixed to $D_{\text{crit}} = 0.9$ in all points of L_W. That is, after switching, all energy dissipation is due to crack opening and there is no more energy dissipation due to bulk degradation.

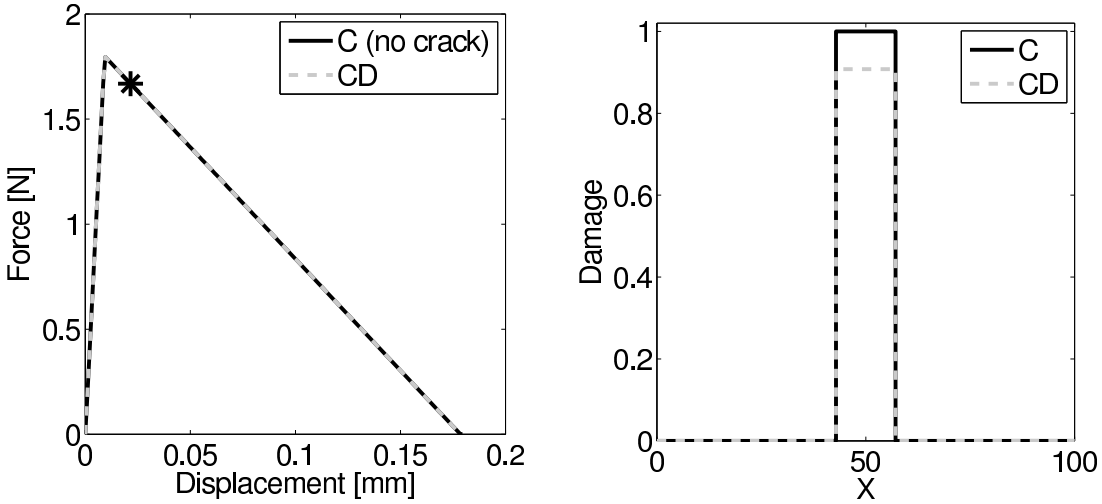

(a) (b)

Figure 5.9: Uniaxial tension test (continuous and continuous-discontinuous approaches with a local damage model): (a) force-displacement curves; (b) damage profiles.

Non-local continuum damage model. The uniaxial tension test is simulated now with a non-local damage model. A characteristic length $\ell = \sqrt{5}$ mm is chosen. First, the continuous strategy is employed. Results are shown in Figure 5.10.

Figure 5.10(a) shows the force-displacement curve. Analogous to local results, a first elastic branch, whose slope is given by Equation (5.9), is observed. Nevertheless, due to non-locality, the force-displacement behaviour after the peak force is reached is qualitatively different. If a local model is used, all points in L_W reach the damage initiation strain ε_0 at the same time and all points start to unload following the softening branch simultaneously. Thus, the stiffness of the bar is piecewise constant: E, E_{soft}, E. However, if a non-local model is employed, the non-homogeneous behaviour leads to a stiffness that is not piecewise constant.

Damage profiles are shown in Figure 5.10(b). Analogous to local results, see Figure 5.5(b), if a continuous strategy is employed from the beginning to the end of

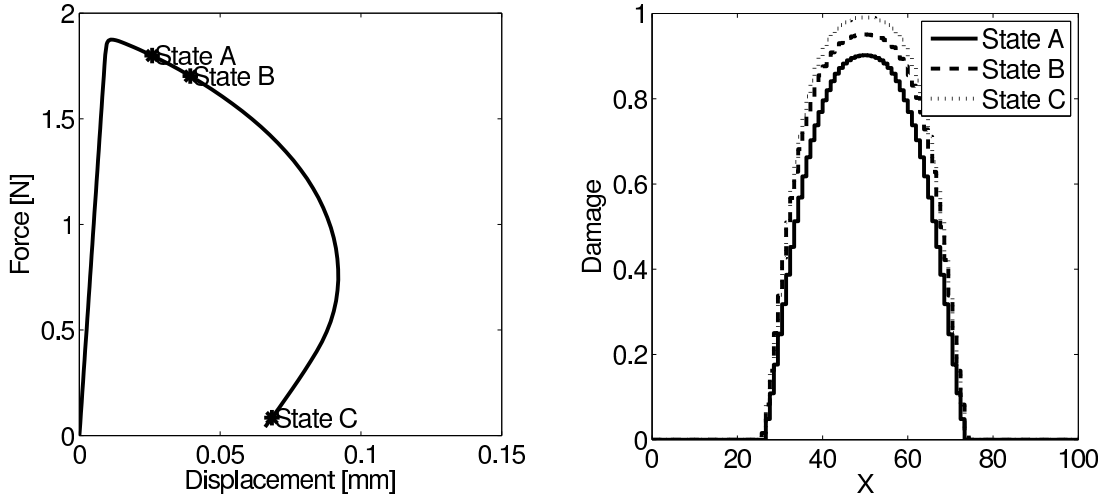

(a) (b)

Figure 5.10: Uniaxial tension test (continuous strategy with a non-local damage model): (a) force-displacement curves; (b) damage profiles.

failure, the damage parameter reaches a maximum value equal to 1, see the State C in Figure 5.10(b). Nevertheless, compared to local damage results, two main differences arise. First, the damage profile is not piecewise constant. Second, the width of damage profile λ_D is not equal to the length of the weakened part. In fact, it does not depend on L_W but on the characteristic length ℓ. These two key differences result from non-locality.

As discussed for the local model, let us consider now that as soon as damage reaches a critical value $D_{\text{crit}} = 0.9$ (the state A shown in Figure 5.10), a cohesive crack (with a linear traction-separation law, see Figure 5.8) is introduced at $x = \frac{L}{2}$ and the proposed continuous-discontinuous strategy is used. As discussed above, this model switching has two main consequences.

First, due to the cohesive law, all points in λ_D unload following the secant unloading branch with slope

$$E(x)\Big(1 - D(x)\Big) = \begin{cases} E_W\Big(1 - D(x)\Big) & \text{if } x \in L_W \\ E\Big(1 - D(x)\Big) & \text{otherwise} \end{cases} \tag{5.15}$$

Note that, compared to the local framework, only the point located at $x = \frac{L}{2}$, see Figure 5.11(b), unloads following the branch with slope $E_W\,(1 - D_{\text{crit}})$. Indeed, the rest of the points in λ_D unload following the secant unloading branch with the stiffness

at model switching, see Figure 5.11(a) while the rest of the bar unloads following the elastic branch with slope E, see Figure 5.11(c).

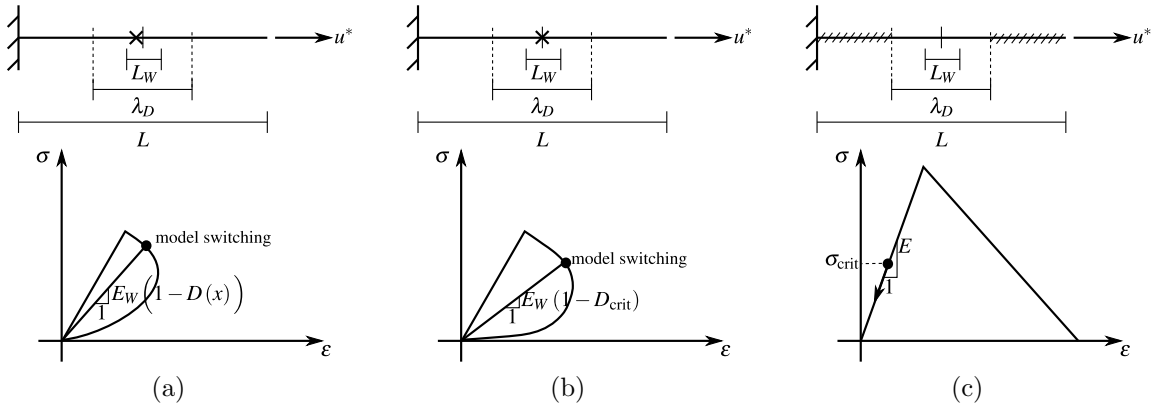

Figure 5.11: Once damage reaches a critical value, the model switching is carried out. Hence, (a) points in λ_D unload following the secant unloading branch with slope $E\,(x)\left(1-D\,(x)\right)$. In contrast to local models, (b) here only the point $x=\frac{L}{2}$ unloads following the branch with slope $E_W\,(1-D_{\text{crit}})$. (c) All points outside the damaged zone λ_D unload following the elastic branch with slope E.

Second, analogous to the local model, no more energy dissipation in the bulk occurs after switching strategies. Therefore, in order to ensure energy consistency, the energy not yet dissipated by the bulk needs to be transferred to the cohesive crack. If a non-local damage model is employed, this quantity, see Figure 5.12(a), cannot be exactly computed (without a reference continuous simulation). Indeed, for each point of the bar, the energy not yet dissipated depends on the unloading branch, which is not known at model switching, see Figure 5.12(b). Therefore, it needs to be estimated as accurately as possible.

One possible way to estimate this energy consists of assuming that all points in λ_D unload following the local softening branch (from switching to zero stress). This assumption, shown schematically in Figure 5.13 and made by Comi et al. (2007), is quite crude if a non-local model is used: due to non-locality, only the point $x=\frac{L}{2}$ unloads following this softening branch, while all the other points in λ_D unload secantly to the origin. Hence, this leads to an overestimation of the energy to be transferred to the cohesive crack.

A more accurate estimation may be obtained if the unloading behaviour —either secant or softening— is taken into account. The key idea of our method is to estimate

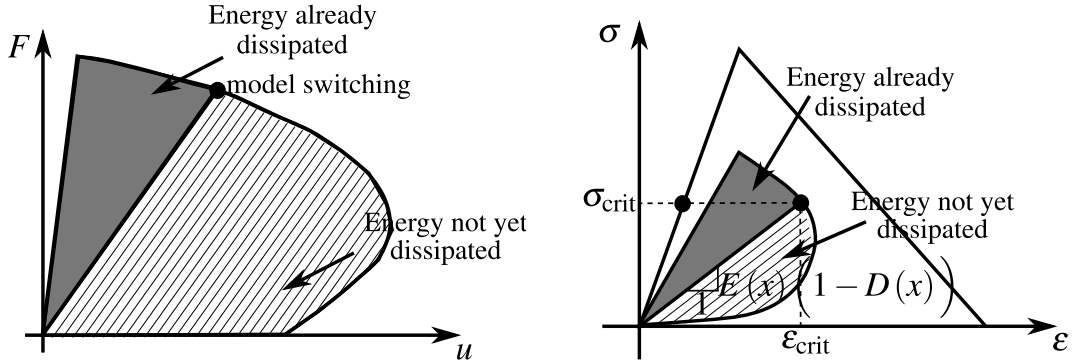

Figure 5.12: (a) In contrast to local models, the energy that needs to be transferred to the crack (the energy not yet dissipated by the bulk at model switching) cannot be exactly computed, since (b) for each point in λ_D, the energy not yet dissipated depends on an unloading behaviour, which is not known at model switching.

the energy to be transferred by means of the tangent line to $\sigma(\varepsilon)$ at model switching, see Figure 5.14.

It must be stressed that a better approximation of the energy to be transferred may be obtained if, after switching models, some load increments with the continuous approach are carried out, see Figure 5.15. Indeed, once the model switching is determined, some extra load steps with the continuous model can be carried out to estimate the energy not yet dissipated by the bulk with more accuracy and hence, the cohesive crack law. Then, back to the switching point, the simulation is resumed with the continuous-discontinuous strategy. The computational cost of this refinement is marginal, because only a few load steps are computed twice (first with the continuous approach and then with the continuous-discontinuous one).

The results for the combined strategy (with the cohesive slope obtained by prescribing the proposed energy balance) are shown in Figure 5.16. Both the continuous and continuous-discontinuous results are plotted.

In Figure 5.16(b), the profiles D are shown. As discussed for the local model, the damage profile reaches a maximum value equal to 1 if a continuous strategy is used. If a combined technique is employed, damage is fixed to D_{crit} at $x = \frac{L}{2}$ and, after switching, there is no more energy dissipation due to bulk deformation.

Figure 5.16(a) shows the force-displacement curves. Here, the cohesive parameter T computed by means of the tangent line to $\sigma(\varepsilon)$ at switching point is used. As seen,

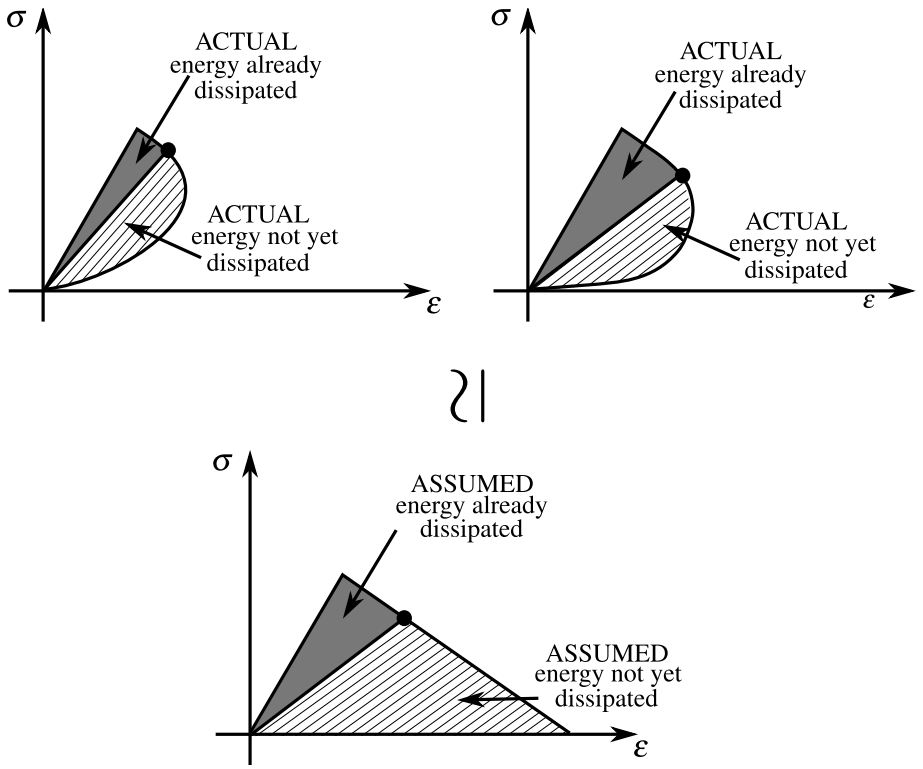

Figure 5.13: If all points in λ_D are considered to unload following the softening branch, the energy to be transferred is overestimated.

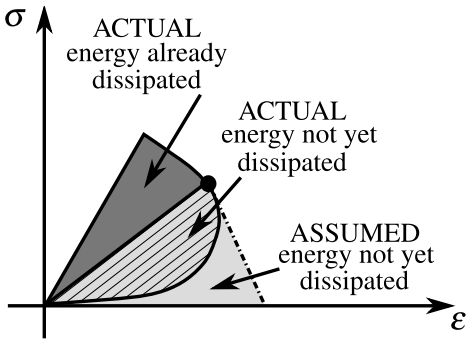

Figure 5.14: For a given point in λ_D, the energy not yet dissipated by the bulk (striped area) is estimated with the tangent line to $\sigma(\varepsilon)$ (dash-dot line). Hence, an approximation (light grey area) of the actual remaining energy is computed.

the area under the combined force-displacement curve ($Area = 2.88$ mJ) is larger than twice the area under the continuous curve ($Area = 1.29$ mJ). This is due to the fact that the energy to be transferred to the cohesive crack has been overestimated. In order to obtain a better approximation of this energy, and suggested by the above

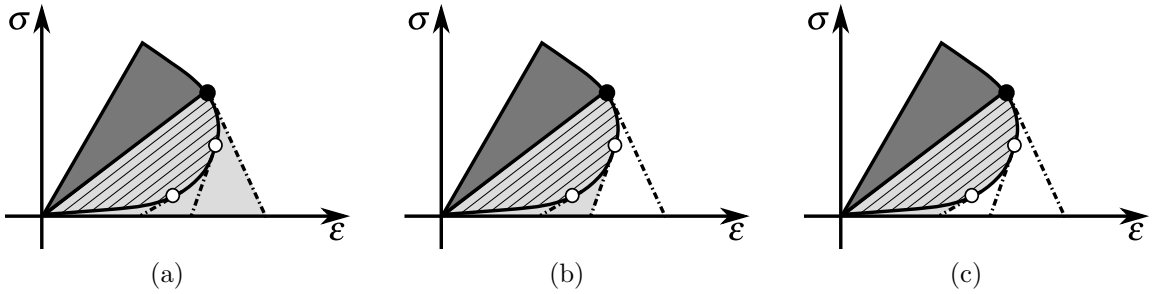

(a) (b) (c)

Figure 5.15: (a) If the energy to be transferred is estimated by means of the tangent line to $\sigma(\varepsilon)$ at model switching (black circle), a worse approximation is obtained than (b) if the tangent to $\sigma(\varepsilon)$ with some more load steps (white circle) is used. (c) The more load steps, the more accurate estimation of the energy not yet dissipated is obtained.

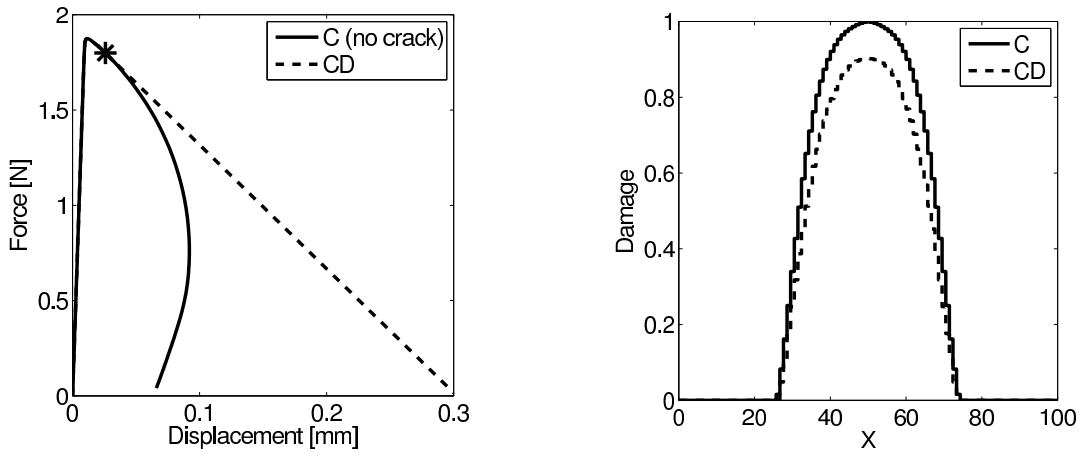

(a) (b)

Figure 5.16: Uniaxial tension test (continuous and continuous-discontinuous approaches with a non-local damage model): (a) force displacement curves; (b) damage profiles.

discussion, some extra load steps with the continuous technique are carried out. Thus, a better solution, see Figure 5.17(a), is obtained. It is observed that the more extra steps we use, the more accurate the energy to be transferred is, see Figure 5.17(b).

It is noted that the linear behaviour of the force-displacement curve obtained with the combined approach is due to two reasons. First, a linear cohesive law is considered. Second, once the crack is introduced, the stiffness of the bar is constant. Indeed, since damage is *frozen* in all the damaged bulk, each point of the damaged

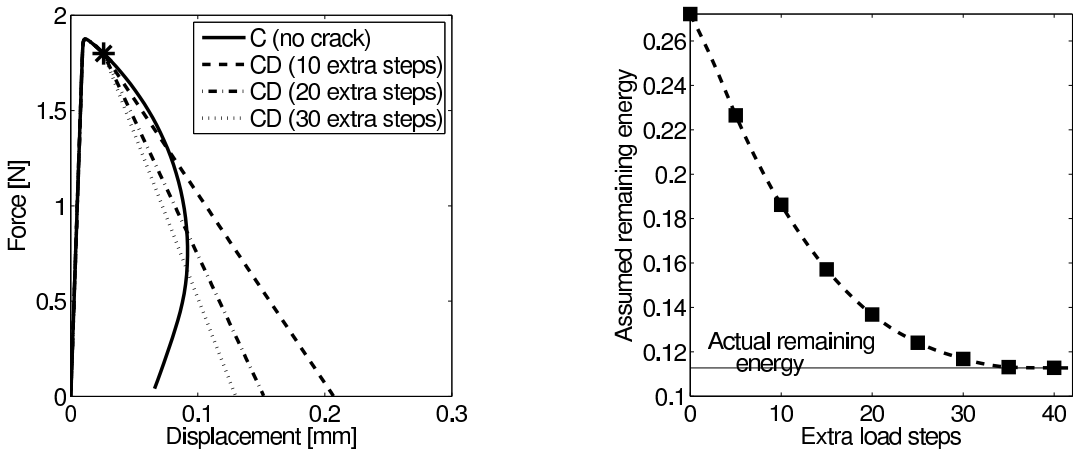

(a) (b)

Figure 5.17: The more extra load steps are carried out with the continuous approach, the more accurate the energy to be transferred is estimated.

band unloads with a constant elastic stiffness $E(x) \cdot \Big(1 - D(x)\Big)$.

5.3.2 Energy balance for a multidimensional problem

The extension of the proposed energy balance to a multidimensional setting is discussed in this section by means of a two-dimensional three-point bending test. Here, the simplified Mazars damage model, see Equation (3.14), and a bilinear damage evolution law, see Equation (3.15), are considered. A uniform mesh of 1 640 (41×40) bilinear quadrilateral elements is used and the geometric and material parameters are summarised in Table 5.2.

Table 5.2: Three-point bending test: geometrical and material parameters.

Meaning	**Symbol**	**Value**
Length of the beam	L	300 mm
Height of the beam	h	100 mm
Young's modulus	E	30 000 MPa
Damage initiation state variable	Y_0	10^{-4}
Final state variable	Y_f	1.25×10^{-2}
Poisson's ratio	ν	0.00

To begin with, a continuous simulation is carried out. A characteristic length $\ell = 1$ mm is considered. Results are shown in Figure 5.18.

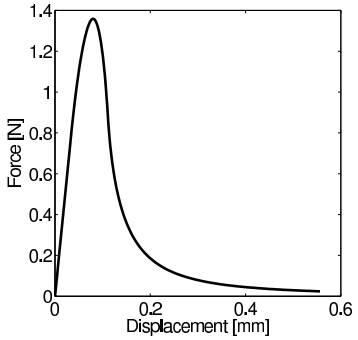

(a)

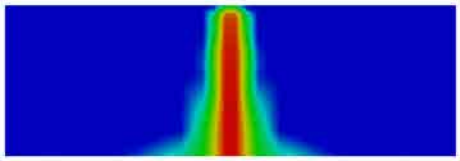

(b)

Figure 5.18: Three-point bending test (continuous approach): (a) force-displacement curve; (b) damage pattern.

Let us now consider that as soon as damage reaches a critical value $D_{\text{crit}} = 0.995$ in a finite element located on the boundary of the mesh, a cohesive crack is introduced in that element and the proposed combined strategy is used. Due to the mode I behaviour of the three point bending test, the traction-separation law

$$\bar{\mathbf{t}}_d = \left\{ \begin{array}{c} \bar{t}_n \\ \bar{t}_s \end{array} \right\} = \mathbf{T} \left\{ \begin{array}{c} [\![\boldsymbol{u}]\!]_n \\ [\![\boldsymbol{u}]\!]_s \end{array} \right\} + \left\{ \begin{array}{c} t_{\text{crit}} \\ 0 \end{array} \right\} = \left(\begin{array}{cc} T & 0 \\ 0 & 0 \end{array} \right) \left\{ \begin{array}{c} [\![\boldsymbol{u}]\!]_n \\ [\![\boldsymbol{u}]\!]_s \end{array} \right\} + \left\{ \begin{array}{c} t_{\text{crit}} \\ 0 \end{array} \right\} \quad (5.16)$$

is employed, where $[\![\boldsymbol{u}]\!]_n$ and $[\![\boldsymbol{u}]\!]_s$ are the normal and sliding components of the crack opening $[\![\boldsymbol{u}]\!]$ respectively and t_{crit} is the critical normal component of the traction vector.

This model switching —from the continuous to the combined strategy— entails one main consequence: damage in the cracked element is fixed to D_{crit} and all points of this element start to unload following the branch with slope $E\,(1 - D_{\text{crit}})$. In addition, points located near the crack faces unload following the secant branch with the stiffness at model switching.

Nevertheless, in contrast to the one-dimensional framework, ahead of the crack tip, damage keeps growing. In other words, the energy dissipated by the bulk if a combined technique is used is not the energy already dissipated in the bulk at model switching. This difference —between the one- and the multi-dimensional settings— is crucial when prescribing the energy balance. Indeed, in the uniaxial tension test discussed above, the energy balance is prescribed in all points of the bar, since all

points unload secantly once the crack is introduced. However, if two- and three-dimensional problems are considered, the energy balance should be only prescribed in the area where points unload secantly.

In order to define this zone, that we have called *crack influence zone*, the following technique is used. First, the perpendicular to the direction of crack growth at the crack tip is considered. Then, the crack influence zone is defined as the area behind the crack tip, see Figure 5.19.

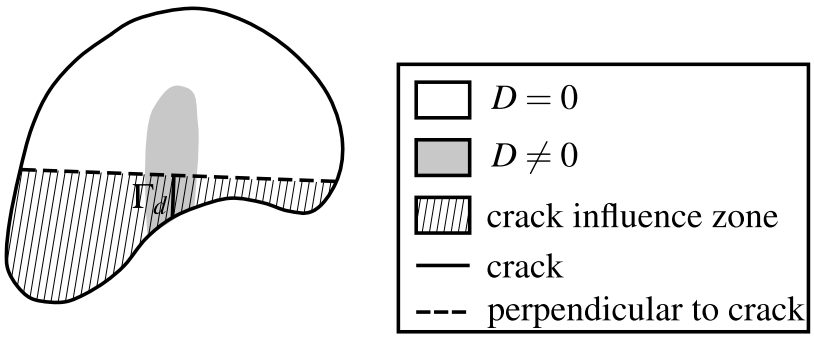

Figure 5.19: The perpendicular to the direction of crack growth allows to define the crack influence zone (striped area).

Once this area is defined, the energy balance presented by means of the uniaxial tension test can be used. That is, for each point in the *crack influence zone*, the energy not yet dissipated by the bulk is transferred to the crack. In order to estimate it, the tangent line to each component of $\boldsymbol{\sigma}(Y)$, with Y the state variable of the damage model, is used.

The results for the the continuous and combined strategies are shown in Figure 5.20. Both the force-displacement curves, see Figure 5.20(a), and the damage pattern, see Figure 5.20(b) are shown. For comparison purposes, two different values of the cohesive parameter T are considered. First, the energy balance proposed by Comi et al. (2007) is employed. That is, an energy balance considering that all points unload following a softening branch is enforced. Second, our energy balance is prescribed. It is noted that considering the unloading behaviour of each point in the crack influence zone —either softening or secant— the energy to be transferred is more accurately estimated.

As discussed, the main difference between the one- and the multidimensional setting is the domain where the energy balance is prescribed. Indeed, in 1D, the energy equilibrium is prescribed in all the damaged band. However, in 2D or 3D, the

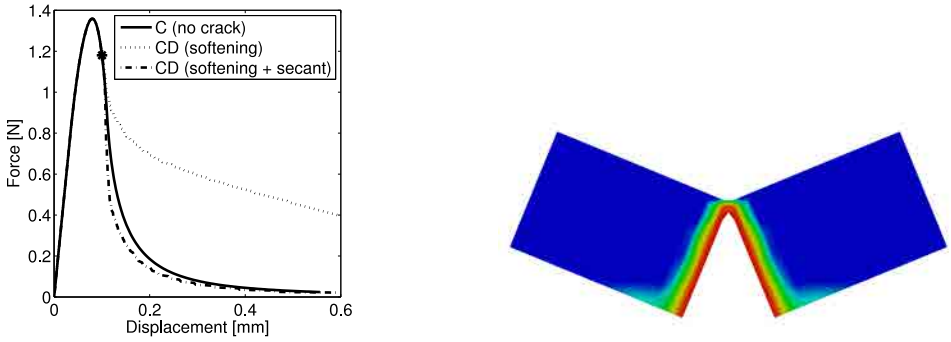

(a) (b)

Figure 5.20: Three-point bending test (continuous and continuous-discontinuous approaches): (a) force-displacement curves; (b) damage pattern.

so-called *crack influence zone* must be defined. One means of avoiding the definition of this zone is to use a one-dimensional reference continuous simulation to extract the cohesive parameter T. In other words, as soon as the model switching is determined, an *equivalent* uniaxial tension test —that is, a uniaxial test with the same geometrical and material parameters of the multidimensional test— is carried out to compute the cohesive parameter T.

The capabilities of this new approximation are illustrated here by means of the previous three-point bending test. Indeed, as soon as damage reaches a critical value $D_{\text{crit}} = 0.995$ in a finite element located on the boundary of the mesh, a cohesive crack, whose law is given by the softening parameter T in Equation (5.16), is introduced. To compute the cohesive parameter, the one-dimensional energy balance discussed in Section 5.3.1 —with the material and geometrical parameters of the three-point bending test— is prescribed. Results are shown in Figure 5.21. As seen, little differences are observed if the energy balance is prescribed by means of the one-dimensional uniaxial test or with the two-dimensional setting. However, regarding the computational cost, this alternative way to define T is very appealing.

5.4 Concluding remarks

The continuous-discontinuous damage model presented in Chapter 4 has been extended to cohesive cracks. In order to describe the first stages of failure, a non-local continuous formulation with smoothed displacements is proposed. At the end of each

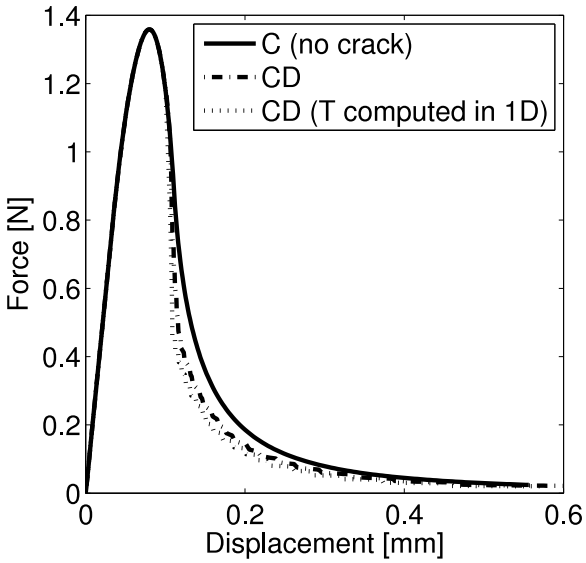

Figure 5.21: Three-point bending test (continuous and continuous-discontinuous approaches).

time step, the approach checks if the damage parameter is equal to a critical value $D_{\text{crit}} < 1$ in an element located on the boundary of the mesh. In such a case, a crack is introduced and the X-FEM is used to enrich the standard and the gradient-enhanced displacement fields, see Figure 5.22.

As suggested by *the equivalent crack concept*, the cohesive crack law is defined in such a way that the energy dissipated with a continuous model and with a continuous-discontinuous model are equal. The main difficulty of this energy balance is that after the switching —from the continuum to the discrete strategy— the continuous model is interrupted. Hence, without a reference continuous simulation, the energy to be transferred is not known and needs to be estimated.

Regarding this energy balance, the main results are:

- In order to estimate the energy to be transferred, a uniaxial tension test is first considered. In such a case, the model switching entails two main consequences. First, damage is fixed in all the damaged part. Hence, after changing models, all points start to unload elastically with the secant stiffness at model switching. Second, no more energy dissipation in the bulk occurs. Therefore, in order to ensure energy consistency, the energy not yet dissipated by the bulk (when switching models) needs to be transferred to the cohesive crack.

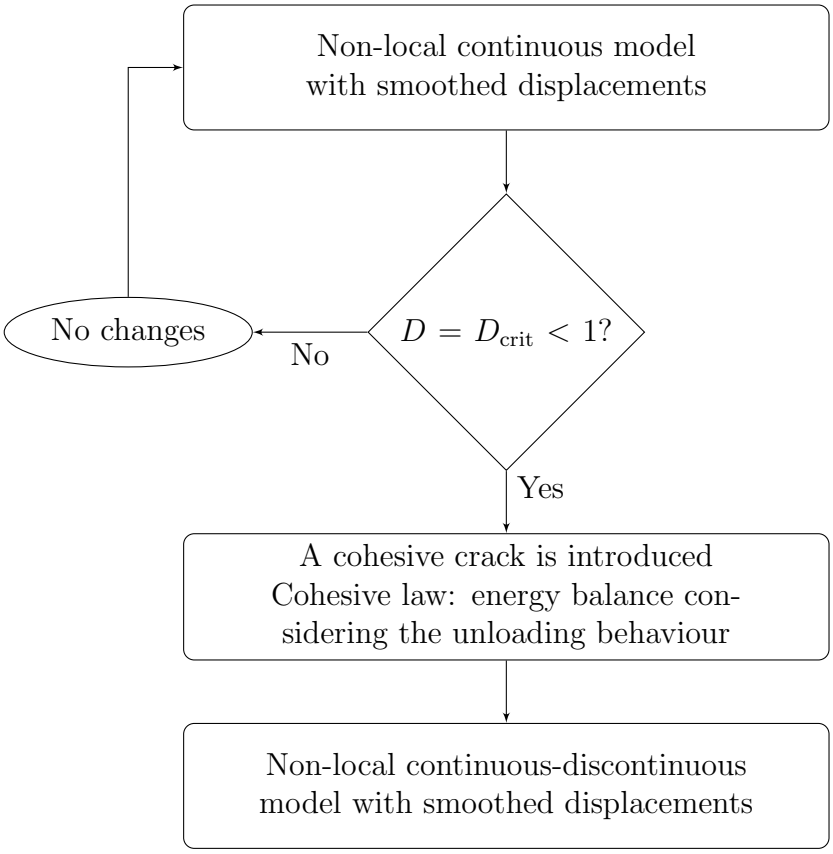

Figure 5.22: Proposed continuous-discontinuous model.

  - If a local damage model is considered, this quantity can be exactly computed.
  - With a non-local damage model, the energy to be transferred depends on the unloading branch, which is not known at model switching. In order to approximate it, we propose to use the tangent line to $\sigma(\varepsilon)$ at model switching. Thus, an accurate estimation of the energy to be transferred is obtained. As discussed, if more accuracy is needed, some extra load steps with the continuous model can be carried out. Indeed, once the model switching is determined, some extra load steps with the continuous model can be performed. Then, back to the switching point, the simulation is resumed with the continuous-discontinuous strategy.

- In order to extend to a two- and three-dimensional setting the proposed strategy, a main difficulty arises. Indeed, in contrast to the one-dimensional framework,

ahead of the crack tip, damage keeps growing. Hence, the energy balance cannot be prescribed in all the damaged bulk but only in the *crack influence zone*. In other words, it should be prescribed in those points that unload following the secant branch.

Regarding the linearisation and the consistent tangent matrix needed to attain quadratic convergence in the Newton-Raphson method, little changes are needed compared to the strategy of Chapter 4. Indeed, the only difference between introducing a traction-free crack and a cohesive crack is an extra term where the cohesive forces appear thus leading to an extra block matrix in the tangent matrix.

5.5 Future work

The work carried out in this chapter leaves some open research lines to be addressed in the future.

Extension of the proposed energy balance to mode II and mode III loading conditions. So far the proposed energy balance has been tested by means of a three-point bending test. That is, only mode I loading conditions have been considered. Hence, it would be interesting to retrieve some of the numerical examples carried out in Chapter 4 with a lower critical damage value and include cohesive cracks.

Approximation of the energy to be transferred by means of a uniaxial tension test (even in a two- and three-dimensional setting). As discussed by means of the three-point bending tension test, carrying out a one-dimensional reference continuous simulation to extract the cohesive parameter T is an appealing way to compute the energetically equivalent cohesive crack law. Hence, it would be interesting to analyse the capabilities of this alternative way to define the cohesive slope in a more generalised setting.

Chapter 6

Summary and future work

6.1 Summary

In this dissertation we have developed a new finite element approach for quasi-brittle failure that bridges damage and fracture mechanics. To this end, four main contributions —discussed in detail in the previous three chapters— have been presented. Here, we summarise the principal results:

1. **We have extended the applicability of smoothed displacements to a two- and three-dimensional setting**. In Chapter 3, we have extended the applicability to a multidimensional setting of an alternative gradient-enriched continuous formulation to simulate a failure process. The key idea of this new approach, presented and illustrated with a one-dimensional example by Rodríguez-Ferran et al. (2005), is to use a smoothed displacement field $\widetilde{\boldsymbol{u}}$, which is the solution of a partial differential equation, to drive damage evolution.

   As discussed by Jirásek and Marfia (2005), the extension of this alternative gradient-enhanced formulation to a multidimensional context is not straightforward. Indeed, Dirichlet boundary conditions —prescribed in the one-dimensional setting— do not allow a correct widening of the damage zone at the boundary when dealing with two- and three-dimensional problems; homogeneous Neumann conditions —prescribed for the standard gradient model— do not guarantee that a constant strain field leads to constant stresses and non-homogeneous Neumann conditions do not ensure conservation of volume.

Hence, in order to overcome these limitations, combined boundary conditions are proposed in this dissertation. They consist of prescribing Dirichlet boundary conditions for the normal component of the displacement field and non-homogeneous Neumann boundary conditions for the tangential ones. As illustrated by means of different numerical simulations, regularisation via smoothed displacement —if combined boundary conditions are prescribed for $\widetilde{\boldsymbol{u}}$— precludes mesh dependence also in a multidimensional setting.

2. **We have proposed a new continuous-discontinuous formulation based on smoothed displacements**. A new continuous-discontinuous damage model is presented in Chapters 4 and 5. The key idea of this new strategy is to combine the gradient-enriched formulation discussed in Chapter 3 with an extended finite element approach. Thus, the entire failure process —from formation of micro-cracks to the possible development of macro-cracks— may be described. The switching from the continuum to the discrete approach occurs when the damage parameter in a finite element located on the boundary of the mesh reaches a critical value D_{crit}. Firstly, in Chapter 4, $D_{\text{crit}} \simeq 1$. Thus, we focus on the coupling between smoothed displacements and traction-free cracks. Secondly, in Chapter 5, $D_{\text{crit}} < 1$ thus introducing a cohesive crack.

   As discussed in these chapters and in the three appendices, smoothed displacements are attractive from a computational viewpoint. Indeed, in order to calculate the tangent block matrix obtained after the linearisation of the regularisation equation, we need to compute the standard mass $\mathbf{M}$ and diffusivity $\mathbf{D}$ matrices, which are constant through all the simulation, and the enriched mass $\mathbf{M}_\psi$ and diffusivity $\mathbf{D}_\psi$ matrices, which only change when the crack propagates. Regarding the combined boundary conditions, matrix $\mathbf{K}_{\text{BC}}$ is also constant through all the simulation, while $\mathbf{K}_{\psi,\text{BC}}$ only changes when the crack grows.

3. **We have proposed a new criterion (based on geometrical assumptions) to track the crack path**. Chapter 4 focuses on one of the main issues concerning the switching from a continuous approach to discrete cracks: the definition of the crack path. Indeed, in a regularised continuum, the direction along which the crack propagates cannot be analytically derived and hence, other criteria should be used. In this dissertation, instead of the classical mechanical criteria, we propose to define the crack-path using a geometrical

criterion. In particular, given a regularised damage field $D(\boldsymbol{x})$, we propose to propagate the crack following the direction dictated by the medial axis of the isoline (or isosurface in 3D) $D(\boldsymbol{x}) = D^*$. In other words, a geometric tool widely used for image analysis, computer vision applications or mesh generation purposes is used here to locate cracks.

As illustrated by means of different two- and three-dimensional examples, since this technique is exclusively based on the shape of the regularised damage field, no mesh sensitivity is observed when determining the crack direction.

4. **We have proposed a new criterion to estimate the energy that needs to be transferred to the cohesive crack**. In Chapter 5, we have introduced a new method to estimate the energy to be transferred at model switching —from the continuous to the continuous-discontinuous strategy. In contrast to other existing techniques, see for instance Cazes et al. (2010), this method allows to estimate the amount of energy to be transferred without knowing a solution of a continuous reference model in advance. The main idea of this new technique consists of predicting the unloading behaviour —either softening or secant— of each point in the continuous bulk. Thus, compared to other strategies where all the points in the damaged bulk are considered to unload following the softening branch, see Comi et al. (2007), the energy to be transferred is more accurately computed.

   Firstly, the proposed method is illustrated with a uniaxial tension test. As seen, approximating the unloading branch by means of the tangent line to $\sigma(\varepsilon)$ at model switching provides a better approximation of the energy to be transferred than other exiting techniques. Secondly, the strategy is extended to a two- and three-dimensional setting. In such a case, the energy balance must be only prescribed in the *crack influence zone* and not in all points of the damaged bulk.

6.2 Future work

The work carried out in this dissertation leaves several topics to be addressed in the near future. These open research lines —discussed in detail in the previous three chapters— are summarised here:

1. **To investigate the capacity of smoothed displacements to describe fundamental problems when dealing with quasi-brittle structures**. In this dissertation, we have analysed the capabilities of smoothed displacements to overcome the pathological mesh dependence exhibited by local approaches. Apart from precluding mesh dependence, it would be also interesting to investigate the capacity of smoothed displacements to tackle other fundamental issues of quasi-brittle failure, such as size effects —the change of behaviour when the spatial dimensions are scaled— or damage initiation when dealing with notched specimens —damage initiation requires that damage starts at the notch tip, not inside the specimen.

2. **To further extend the finite element approximation to simulate more general tests**. In this dissertation, problems involving one single crack propagating through the continuum are analysed. Nevertheless, if the finite element approximation is further extended, more general problems may be tackled. For instance, problems including multiple cracks —either non-intersecting or branched discontinuities— or cracks lying within a finite element —with the crack tip not necessarily coincident with an element edge— can be considered.

3. **To extend the applicability of the proposed energy balance to mode II and mode III loading conditions**. In this dissertation, the proposed energy balance is tested with mode I loading conditions. Therefore, it would be interesting to extend the proposed method to problems involving different modes of fracture.

4. **To take advantage of discrete cracks to save computational time**. On the one hand, regularised continuous formulations provide a reliable description of the first stages of failure processes as long as the finite element mesh employed in the simulations is fine enough. On the other hand, the use of the eXtended Finite Element Method (X-FEM) allows to describe failure on relatively coarse meshes. Thus, it would be interesting to take advantage of this property. Indeed, we would like to explore the consequences of including a local derefiner —after model switching— to obtain a coarser finite element mesh and save computational time.

Appendix A

Variational formulation with smoothed displacements

In this appendix the variational formulation of the proposed model is derived: both the equilibrium and the regularisation equations with combined boundary conditions are cast in a weak form. First, in Section A.1, the continuous model is taken into account. Regarding the regularisation equation, special emphasis is placed on the way combined boundary conditions are prescribed. Second, in Section A.2, the continuous-discontinuous model is considered. Attention is focused on the way discontinuities are introduced.

A.1 Continuous model

A.1.1 Equilibrium equation

In this first section, the equilibrium equation without body forces

$$\nabla \cdot \boldsymbol{\sigma} = \mathbf{0} \quad \text{in } \Omega \tag{A.1a}$$

$$\boldsymbol{\sigma} \cdot \boldsymbol{n} = \bar{\boldsymbol{t}} \quad \text{on } \Gamma_t \tag{A.1b}$$

$$\boldsymbol{u} = \boldsymbol{u}^* \quad \text{on } \Gamma_u \tag{A.1c}$$

where $\boldsymbol{\sigma}$ is the Cauchy stress tensor, $\boldsymbol{u}^*$ is a prescribed displacement on the Dirichlet boundary, $\bar{\boldsymbol{t}}$ is the traction on the Neumann boundary and $\boldsymbol{n}$ is the outward unit normal to the body, is cast in a weak form.

The space of trial local displacements is defined by the function $\boldsymbol{u}(\boldsymbol{x})$, where

$$\boldsymbol{u} \in \mathcal{U}_{\boldsymbol{u}} = \left\{ \boldsymbol{u} \,|\, \boldsymbol{u} \in H^1(\Omega) \text{ and } \boldsymbol{u}_{|\Gamma_u} = \boldsymbol{u}^* \right\} \tag{A.2}$$

with $H^1(\Omega)$ a Sobolev space. Analogously, the space of admissible displacement variations is defined by the test function $\boldsymbol{\omega}(\boldsymbol{x})$ with

$$\boldsymbol{\omega} \in \mathcal{W}_{\boldsymbol{u},\mathbf{0}} = \left\{ \boldsymbol{\omega} \mid \boldsymbol{\omega} \in H^1(\Omega) \text{ and } \boldsymbol{\omega}_{|\Gamma_u} = \mathbf{0} \right\} \tag{A.3}$$

Following standard procedures, Equation (A.1) leads to

$$\int_\Omega \nabla^s \boldsymbol{\omega} : \boldsymbol{\sigma} \, \mathrm{d}\Omega = \int_{\Gamma_t} \boldsymbol{\omega} \cdot \bar{\boldsymbol{t}} \, \mathrm{d}\Gamma \qquad \forall \boldsymbol{\omega} \in H^1(\Omega) \tag{A.4}$$

A.1.2 Regularisation equation

Similarly to the equilibrium equation, the regularisation PDE

$$\widetilde{\boldsymbol{u}}(\boldsymbol{x}) - \ell^2 \nabla^2 \widetilde{\boldsymbol{u}}(\boldsymbol{x}) = \boldsymbol{u}(\boldsymbol{x}) \tag{A.5}$$

with combined boundary conditions is also cast in a weak form.

Analogously to local displacements, the space of trial smoothed displacements is defined by the function $\widetilde{\boldsymbol{u}}(\boldsymbol{x})$ where

$$\widetilde{\boldsymbol{u}} \in \mathcal{U}_{\widetilde{\boldsymbol{u}}} = \left\{ \widetilde{\boldsymbol{u}} \,|\, \widetilde{\boldsymbol{u}} \in H^1(\Omega) \text{ and } \widetilde{\boldsymbol{u}} \cdot \boldsymbol{n} = \boldsymbol{u} \cdot \boldsymbol{n} \text{ on } \Gamma \right\} \tag{A.6}$$

Analogously, the space of admissible smoothed displacement variations is defined by the test function $\widetilde{\boldsymbol{\omega}}(\boldsymbol{x})$ with

$$\widetilde{\boldsymbol{\omega}} \in \mathcal{W}_{\widetilde{\boldsymbol{u}},\mathbf{0}} = \left\{ \widetilde{\boldsymbol{\omega}} \mid \widetilde{\boldsymbol{\omega}} \in H^1(\Omega) \text{ and } \widetilde{\boldsymbol{\omega}} \cdot \boldsymbol{n} = \mathbf{0} \text{ on } \Gamma \right\} \tag{A.7}$$

Following standard procedures, the regularisation equation (A.5) is multiplied by the test function $\widetilde{\boldsymbol{\omega}}(\boldsymbol{x})$ and integrated over the domain Ω thus leading to

$$\int_\Omega \widetilde{\boldsymbol{\omega}} \cdot \widetilde{\boldsymbol{u}} \, \mathrm{d}\Omega + \ell^2 \int_\Omega \nabla \widetilde{\boldsymbol{\omega}} : \nabla \widetilde{\boldsymbol{u}} \, \mathrm{d}\Omega - \ell^2 \int_\Gamma \widetilde{\boldsymbol{\omega}} \cdot \nabla \widetilde{\boldsymbol{u}} \cdot \boldsymbol{n} \, \mathrm{d}\Gamma = \int_\Omega \widetilde{\boldsymbol{\omega}} \cdot \boldsymbol{u} \, \mathrm{d}\Omega \tag{A.8}$$

Considering the orthonormal basis of $\mathbb{R}^3$ formed by the normal vector $\boldsymbol{n}$ and the tangent vectors $\boldsymbol{t}_1$ and $\boldsymbol{t}_2$, and taking into account that $\widetilde{\boldsymbol{\omega}} \cdot \boldsymbol{n} = \mathbf{0}$ on Γ, see Equation (A.7),

$$\begin{aligned} \int_\Gamma \widetilde{\boldsymbol{\omega}} \cdot \nabla \widetilde{\boldsymbol{u}} \cdot \boldsymbol{n} \, \mathrm{d}\Gamma &= \int_\Gamma (\widetilde{\boldsymbol{\omega}} \cdot \boldsymbol{t}_1) \cdot (\nabla (\widetilde{\boldsymbol{u}} \cdot \boldsymbol{t}_1) \cdot \boldsymbol{n}) + (\widetilde{\boldsymbol{\omega}} \cdot \boldsymbol{t}_2) \cdot (\nabla (\widetilde{\boldsymbol{u}} \cdot \boldsymbol{t}_2) \cdot \boldsymbol{n}) \, \mathrm{d}\Gamma \\ &= \int_\Gamma (\widetilde{\boldsymbol{\omega}} \cdot \boldsymbol{t}_1) \cdot (\nabla (\boldsymbol{u} \cdot \boldsymbol{t}_1) \cdot \boldsymbol{n}) + (\widetilde{\boldsymbol{\omega}} \cdot \boldsymbol{t}_2) \cdot (\nabla (\boldsymbol{u} \cdot \boldsymbol{t}_2) \cdot \boldsymbol{n}) \, \mathrm{d}\Gamma \end{aligned} \tag{A.9}$$

where in the last equality, combined boundary conditions are prescribed. Hence, $\forall\widetilde{\boldsymbol{\omega}} \in H^1(\Omega)$, Equation (A.8) leads to

$$\begin{aligned}\int_\Omega \widetilde{\boldsymbol{\omega}} \cdot \widetilde{\boldsymbol{u}}\,\mathrm{d}\Omega \;+\; \ell^2 \int_\Omega \nabla\widetilde{\boldsymbol{\omega}} : \nabla\widetilde{\boldsymbol{u}}\,\mathrm{d}\Omega &= \int_\Omega \widetilde{\boldsymbol{\omega}} \cdot \boldsymbol{u}\,\mathrm{d}\Omega + \\ + \;\ell^2 \int_\Gamma (\widetilde{\boldsymbol{\omega}} \cdot \boldsymbol{t}_1) \cdot (\nabla(\boldsymbol{u} \cdot \boldsymbol{t}_1) \cdot \boldsymbol{n}) + (\widetilde{\boldsymbol{\omega}} \cdot \boldsymbol{t}_2) \cdot (\nabla(\boldsymbol{u} \cdot \boldsymbol{t}_2) \cdot \boldsymbol{n})\,\mathrm{d}\Gamma &\quad \text{(A.10)}\end{aligned}$$

A.2 Continuous-discontinuous model

A.2.1 Equilibrium equation

Here, the weak form of the the equilibrium equation without body forces

$$\nabla \cdot \boldsymbol{\sigma} = \mathbf{0} \quad \text{in } \Omega \tag{A.11a}$$

$$\boldsymbol{\sigma} \cdot \boldsymbol{n} = \bar{\boldsymbol{t}} \quad \text{on } \Gamma_t \tag{A.11b}$$

$$\boldsymbol{\sigma} \cdot \boldsymbol{n} = \bar{\boldsymbol{t}}_d \quad \text{on } \Gamma_d \tag{A.11c}$$

$$\boldsymbol{u} = \boldsymbol{u}^* \quad \text{on } \Gamma_u \tag{A.11d}$$

is derived. On the one hand, if traction-free cracks are considered, see Chapter 4, $\bar{\boldsymbol{t}}_d = \mathbf{0}$. On the other hand, if cohesive cracks are taken into account, see Chapter 5,

$$\dot{\bar{\boldsymbol{t}}}_d = \boldsymbol{f}\left(\llbracket \dot{\boldsymbol{u}} \rrbracket\right) \tag{A.12}$$

with $\boldsymbol{f}$ relating traction rate $\dot{\bar{\boldsymbol{t}}}_d$ and displacement jump rate $\llbracket \dot{\boldsymbol{u}} \rrbracket$.

In a continuous-discontinuous model, the space of trial local displacements is defined by the function

$$\boldsymbol{u}(\boldsymbol{x}) = \boldsymbol{u}^1(\boldsymbol{x}) + \psi(\boldsymbol{x})\,\boldsymbol{u}^2(\boldsymbol{x}) \tag{A.13}$$

where ψ is the sign function centred at the discontinuity Γ_d and

$$\boldsymbol{u}^1 \in \mathcal{U}_{\boldsymbol{u}} = \left\{\boldsymbol{u} \mid \boldsymbol{u} \in H^1(\Omega) \text{ and } \boldsymbol{u}_{|\Gamma_u} = \boldsymbol{u}^*\right\} \tag{A.14a}$$

$$\boldsymbol{u}^2 \in \mathcal{U}_{\boldsymbol{u},\mathbf{0}} = \left\{\boldsymbol{u} \mid \boldsymbol{u} \in H^1(\Omega) \text{ and } \boldsymbol{u}_{|\Gamma_u} = \mathbf{0}\right\} \tag{A.14b}$$

with $H^1(\Omega)$ a Sobolev space. Analogously, the space of admissible displacement variations is defined by the test function $\boldsymbol{\omega}(\boldsymbol{x}) = \boldsymbol{\omega}^1(\boldsymbol{x}) + \psi(\boldsymbol{x})\boldsymbol{\omega}^2(\boldsymbol{x})$ with

$$\boldsymbol{\omega}^1, \boldsymbol{\omega}^2 \in \mathcal{W}_{\boldsymbol{u},\mathbf{0}} = \left\{\boldsymbol{\omega} \mid \boldsymbol{\omega} \in H^1(\Omega) \text{ and } \boldsymbol{\omega}_{|\Gamma_u} = \mathbf{0}\right\} \tag{A.15}$$

Then, following standard procedures, Equation (A.11) leads to

$$\int_\Omega \nabla^s \boldsymbol{\omega}^1 : \boldsymbol{\sigma}\, \mathrm{d}\Omega = \int_{\Gamma_t} \boldsymbol{\omega}^1 \cdot \bar{\boldsymbol{t}}\, \mathrm{d}\Gamma \quad \forall \boldsymbol{\omega}^1 \in H^1(\Omega) \tag{A.16a}$$

$$\int_\Omega \psi \nabla^s \boldsymbol{\omega}^2 : \boldsymbol{\sigma}\, \mathrm{d}\Omega + 2\int_{\Gamma_d} \boldsymbol{\omega}^2 \cdot \bar{\boldsymbol{t}}_d\, \mathrm{d}\Gamma = \int_{\Gamma_t} \psi \boldsymbol{\omega}^2 \cdot \bar{\boldsymbol{t}}\, \mathrm{d}\Gamma \quad \forall \boldsymbol{\omega}^2 \in H^1(\Omega) \tag{A.16b}$$

Note that equation (A.16a) is the standard weak form, see Equation (A.4), while equation (A.16b) takes into account the contribution of the crack.

A.2.2 Regularisation equation

Analogously to local displacements, the space of trial smoothed displacements is defined by the function

$$\widetilde{\boldsymbol{u}}(\boldsymbol{x}) = \widetilde{\boldsymbol{u}}^1(\boldsymbol{x}) + \psi(\boldsymbol{x})\, \widetilde{\boldsymbol{u}}^2(\boldsymbol{x}) \tag{A.17}$$

where ψ is the sign function centred at Γ_d and

$$\widetilde{\boldsymbol{u}}^1, \widetilde{\boldsymbol{u}}^2 \in \mathcal{U}_{\widetilde{\boldsymbol{u}}} = \left\{ \widetilde{\boldsymbol{u}} \mid \widetilde{\boldsymbol{u}} \in H^1(\Omega) \text{ and } \widetilde{\boldsymbol{u}} \cdot \boldsymbol{n} = \boldsymbol{u} \cdot \boldsymbol{n} \text{ on } \Gamma \right\} \tag{A.18}$$

Analogously, the space of admissible smoothed displacement variations is defined by the test function

$$\widetilde{\boldsymbol{\omega}}(\boldsymbol{x}) = \widetilde{\boldsymbol{\omega}}^1(\boldsymbol{x}) + \psi(\boldsymbol{x})\, \widetilde{\boldsymbol{\omega}}^2(\boldsymbol{x}) \tag{A.19}$$

with

$$\widetilde{\boldsymbol{\omega}}^1, \widetilde{\boldsymbol{\omega}}^2 \in \mathcal{W}_{\widetilde{\boldsymbol{u}},\boldsymbol{0}} = \left\{ \widetilde{\boldsymbol{\omega}} \mid \widetilde{\boldsymbol{\omega}} \in H^1(\Omega) \text{ and } \boldsymbol{\omega} \cdot \boldsymbol{n} = \boldsymbol{0} \text{ on } \Gamma \right\} \tag{A.20}$$

Taking first variations $\widetilde{\boldsymbol{\omega}}^1$ ($\widetilde{\boldsymbol{\omega}}^2 = \boldsymbol{0}$) and then variations $\widetilde{\boldsymbol{\omega}}^2$ ($\widetilde{\boldsymbol{\omega}}^1 = \boldsymbol{0}$), the final form of the variational statement yields to

$$\begin{aligned}
\int_\Omega \widetilde{\boldsymbol{\omega}}^1 \cdot \widetilde{\boldsymbol{u}}\, \mathrm{d}\Omega \;+\; & \ell^2 \int_\Omega \nabla \widetilde{\boldsymbol{\omega}}^1 : \left(\nabla \widetilde{\boldsymbol{u}}^1 + \psi \nabla \widetilde{\boldsymbol{u}}^2 \right) \mathrm{d}\Omega = \int_\Omega \widetilde{\boldsymbol{\omega}}^1 \cdot \boldsymbol{u}\, \mathrm{d}\Omega + \\
& + \ell^2 \int_\Gamma \left(\widetilde{\boldsymbol{\omega}}^1 \cdot \boldsymbol{t}_1 \right) \cdot \left[\nabla \left(\boldsymbol{u}^1 \cdot \boldsymbol{t}_1 \right) \cdot \boldsymbol{n} + \psi \nabla \left(\boldsymbol{u}^2 \cdot \boldsymbol{t}_1 \right) \cdot \boldsymbol{n} \right] \mathrm{d}\Gamma \\
& + \ell^2 \int_\Gamma \left(\widetilde{\boldsymbol{\omega}}^1 \cdot \boldsymbol{t}_2 \right) \cdot \left[\nabla \left(\boldsymbol{u}^1 \cdot \boldsymbol{t}_2 \right) \cdot \boldsymbol{n} + \psi \nabla \left(\boldsymbol{u}^2 \cdot \boldsymbol{t}_2 \right) \cdot \boldsymbol{n} \right] \mathrm{d}\Gamma
\end{aligned} \tag{A.21a}$$

$$\begin{aligned}
\int_\Omega \psi \widetilde{\boldsymbol{\omega}}^2 \cdot \widetilde{\boldsymbol{u}}\, \mathrm{d}\Omega \;+\; & \ell^2 \int_\Omega \nabla \widetilde{\boldsymbol{\omega}}^2 : \left(\psi \nabla \widetilde{\boldsymbol{u}}^1 + \nabla \widetilde{\boldsymbol{u}}^2 \right) \mathrm{d}\Omega = \int_\Omega \psi \widetilde{\boldsymbol{\omega}}^2 \cdot \boldsymbol{u}\, \mathrm{d}\Omega + \\
& + \ell^2 \int_\Gamma \left(\widetilde{\boldsymbol{\omega}}^2 \cdot \boldsymbol{t}_1 \right) \cdot \left[\psi \nabla \left(\boldsymbol{u}^1 \cdot \boldsymbol{t}_1 \right) \cdot \boldsymbol{n} + \nabla \left(\boldsymbol{u}^2 \cdot \boldsymbol{t}_1 \right) \cdot \boldsymbol{n} \right] \mathrm{d}\Gamma \\
& + \ell^2 \int_\Gamma \left(\widetilde{\boldsymbol{\omega}}^2 \cdot \boldsymbol{t}_2 \right) \cdot \left[\psi \nabla \left(\boldsymbol{u}^1 \cdot \boldsymbol{t}_2 \right) \cdot \boldsymbol{n} + \nabla \left(\boldsymbol{u}^2 \cdot \boldsymbol{t}_2 \right) \cdot \boldsymbol{n} \right] \mathrm{d}\Gamma
\end{aligned} \tag{A.21b}$$

$\forall \widetilde{\boldsymbol{\omega}}^1, \forall \widetilde{\boldsymbol{\omega}}^2 \in H^1(\Omega)$.

Note that the appealing symmetry of Equation (A.21) is due to the fact that the enrichment function is the sign function ($\psi\psi = +1$).

Appendix B

Consistent linearisation of the equilibrium and regularisation equations

---

The new model based on smoothed displacements is very attractive from a computational viewpoint, especially regarding the computation of the consistent tangent matrix needed to achieve quadratic convergence in the Newton-Raphson method. In this appendix, this consistent linearisation is presented. First, in Section B.1, the expression of the consistent tangent matrix of the continuous model is reviewed. Second, in Section B.2, the consistent tangent matrix of the continuous-discontinuous model is derived.

B.1 Continuous model

Finite element discretisation of the weak form of the equilibrium and regularisation equations, see Equations (A.4) and (A.10) leads to the two discrete weak forms

$$\mathbf{r}_{\text{equil}}(\mathbf{u}, \widetilde{\mathbf{u}}) := \mathbf{f}_{\text{int}}(\mathbf{u}, \widetilde{\mathbf{u}}) - \mathbf{f}_{\text{ext}} = \mathbf{0} \tag{B.1a}$$

$$\mathbf{r}_{\text{regu}}(\mathbf{u}, \widetilde{\mathbf{u}}) := -(\mathbf{M} + \ell^2 \mathbf{K}_{\text{BC}})\mathbf{u} + (\mathbf{M} + \ell^2 \mathbf{D})\widetilde{\mathbf{u}} = \mathbf{0} \tag{B.1b}$$

where

$$\mathbf{f}_{\text{int}} = \int_{\Omega} \mathbf{B}^T \boldsymbol{\sigma} \, \mathrm{d}\Omega \tag{B.2a}$$

$$\mathbf{f}_{\text{ext}} = \int_{\Gamma_t} \mathbf{N}^T \bar{\boldsymbol{t}} \, \mathrm{d}\Gamma \tag{B.2b}$$

$$\mathbf{M} = \int_{\Omega} \mathbf{N}^T \mathbf{N} \, \mathrm{d}\Omega \tag{B.2c}$$

$$\mathbf{D} = \int_{\Omega} \nabla \mathbf{N}^T \nabla \mathbf{N} \, \mathrm{d}\Omega \tag{B.2d}$$

$$\mathbf{K}_{\text{BC}} = \int_{\Gamma} \mathbf{N}^T \left(\boldsymbol{t}_1^T \boldsymbol{t}_1 + \boldsymbol{t}_2^T \boldsymbol{t}_2 \right) \nabla \mathbf{N} \cdot \boldsymbol{n} \, \mathrm{d}\Gamma \tag{B.2e}$$

with $\mathbf{N}$ the matrix of shape functions, $\nabla \mathbf{N}$ the matrix of shape function gradients and $\mathbf{B}$ the matrix of shape function derivatives.

Linearisation of Equations (B.1) results in the tangent matrix

$$\mathbf{K}_{\text{tan}} = \begin{bmatrix} \mathbf{K}_{\mathbf{u},\mathbf{u}} & \mathbf{K}_{\mathbf{u},\tilde{\mathbf{u}}} \\ \mathbf{K}_{\tilde{\mathbf{u}},\mathbf{u}} & \mathbf{K}_{\tilde{\mathbf{u}},\tilde{\mathbf{u}}} \end{bmatrix} \tag{B.3}$$

with the matrices defined in Table B.1.

Table B.1: Block matrices of the continuous consistent tangent matrix.

$\mathbf{K}_{\mathbf{u},\mathbf{u}} := \int_{\Omega} \mathbf{B}^T \boldsymbol{C} \mathbf{B} \, \mathrm{d}\Omega$	$\mathbf{K}_{\mathbf{u},\tilde{\mathbf{u}}} := -\int_{\Omega} \mathbf{B}^T \boldsymbol{C} \boldsymbol{\varepsilon} D'(\widetilde{Y}) \frac{\partial \widetilde{Y}}{\partial \widetilde{\boldsymbol{\varepsilon}}} \mathbf{B} \, \mathrm{d}\Omega$
$\mathbf{K}_{\tilde{\mathbf{u}},\mathbf{u}} := -(\mathbf{M} + \ell^2 \mathbf{K}_{\text{BC}})$	$\mathbf{K}_{\tilde{\mathbf{u}},\tilde{\mathbf{u}}} := \mathbf{M} + \ell^2 \mathbf{D}$

Some remarks about the tangent matrix (B.3):

- Matrices $\mathbf{K}_{\mathbf{u},\mathbf{u}}$ and $\mathbf{K}_{\mathbf{u},\tilde{\mathbf{u}}}$ are the secant and the local tangent matrices already obtained by Rodríguez-Ferran et al. (2005).
- Matrices $\mathbf{M}$ and $\mathbf{D}$ are the mass and diffusivity matrices already obtained by Rodríguez-Ferran et al. (2005). They are both constant, due to the linearity of the regularisation equation.
- The only difference between matrix (B.3) and the tangent matrix obtained by Rodríguez-Ferran et al. (2005) resides in matrix $\mathbf{K}_{\text{BC}}$. Indeed, if Dirichlet boundary conditions are prescribed for the smoothed displacement field $\widetilde{\boldsymbol{u}}$ (as done in the cited reference), $\mathbf{K}_{\text{BC}} = \mathbf{0}$ thus leading to $\mathbf{K}_{\tilde{\mathbf{u}},\mathbf{u}} = -\mathbf{M}$.

B.2 Continuous-discontinuous model

Finite element discretisation of the weak form of the equilibrium and regularisation equations, see Equations (A.16) and (A.21), leads to the four discrete weak equations

$$\begin{aligned}
\mathbf{r}_{\text{equil},\mathbf{u}^1}(\mathbf{u},\widetilde{\mathbf{u}}) &:= \mathbf{f}_{\text{int},\mathbf{u}^1}(\mathbf{u},\widetilde{\mathbf{u}}) - \mathbf{f}_{\text{ext},\mathbf{u}^1} = \mathbf{0} && \text{(B.4a)}\\
\mathbf{r}_{\text{equil},\mathbf{u}^2}(\mathbf{u},\widetilde{\mathbf{u}}) &:= \mathbf{f}_{\text{int},\mathbf{u}^2}(\mathbf{u},\widetilde{\mathbf{u}}) - \mathbf{f}_{\text{ext},\mathbf{u}^2} = \mathbf{0} && \text{(B.4b)}\\
\mathbf{r}_{\text{regu},\mathbf{u}^1} &:= -(\mathbf{M}+\ell^2\mathbf{K}_{\text{BC}})\mathbf{u}^1 - (\mathbf{M}_\psi+\ell^2\mathbf{K}_{\psi,\text{BC}})\mathbf{u}^2 \\
&\quad +(\mathbf{M}+\ell^2\mathbf{D})\widetilde{\mathbf{u}}^1 + (\mathbf{M}_\psi+\ell^2\mathbf{D}_\psi)\widetilde{\mathbf{u}}^2 = \mathbf{0} && \text{(B.4c)}\\
\mathbf{r}_{\text{regu},\mathbf{u}^2} &:= -(\mathbf{M}_\psi+\ell^2\mathbf{K}_{\psi,\text{BC}})\mathbf{u}^1 - (\mathbf{M}+\ell^2\mathbf{K}_{\text{BC}})\mathbf{u}^2 \\
&\quad +(\mathbf{M}_\psi+\ell^2\mathbf{D}_\psi)\widetilde{\mathbf{u}}^1 + (\mathbf{M}+\ell^2\mathbf{D})\widetilde{\mathbf{u}}^2 = \mathbf{0} && \text{(B.4d)}
\end{aligned}$$

where $\mathbf{f}_{\text{int},\mathbf{u}^1}$ and $\mathbf{f}_{\text{ext},\mathbf{u}^1}$ are the internal and external forces defined in Equations (B.2a) and (B.2b) respectively, $\mathbf{M}$ is the standard mass matrix, see Equation (B.2c), $\mathbf{D}$ is the standard diffusivity matrix, see Equation (B.2d), and $\mathbf{K}_{\text{BC}}$ is the matrix that takes into account the combined boundary conditions, see Equation (B.2e), whereas

$$\begin{aligned}
\mathbf{f}_{\text{int},\mathbf{u}^2} &= \int_\Omega \psi\mathbf{B}^T\boldsymbol{\sigma}\,\mathrm{d}\Omega + 2\int_{\Gamma_d}\mathbf{N}^T\bar{\boldsymbol{t}}_d\,\mathrm{d}\Gamma && \text{(B.5a)}\\
\mathbf{f}_{\text{ext},\mathbf{u}^2} &= \int_{\Gamma_t}\psi\mathbf{N}^T\bar{\boldsymbol{t}}\,\mathrm{d}\Gamma && \text{(B.5b)}\\
\mathbf{M}_\psi &= \int_\Omega \psi\mathbf{N}^T\mathbf{N}\,\mathrm{d}\Omega && \text{(B.5c)}\\
\mathbf{D}_\psi &= \int_\Omega \psi\nabla\mathbf{N}^T\nabla\mathbf{N}\,\mathrm{d}\Omega && \text{(B.5d)}\\
\mathbf{K}_{\psi,\text{BC}} &= \int_\Gamma \psi\mathbf{N}^T\left(\boldsymbol{t}_1^T\boldsymbol{t}_1+\boldsymbol{t}_2^T\boldsymbol{t}_2\right)\nabla\mathbf{N}\cdot\boldsymbol{n}\,\mathrm{d}\Gamma && \text{(B.5e)}
\end{aligned}$$

Note that if traction-free cracks are considered, see Chapter 4, $\bar{\boldsymbol{t}}_d = \mathbf{0}$, thus leading to $\mathbf{f}_{\text{int},\mathbf{u}^2} = \int_\Omega \psi\mathbf{B}^T\boldsymbol{\sigma}\,\mathrm{d}\Omega$.

Linearisation of Equations (B.4) results in the tangent matrix

$$\mathbf{K}_{\text{tan}} = \begin{bmatrix}
\mathbf{K}_{\mathbf{u}^1,\mathbf{u}^1} & \mathbf{K}_{\mathbf{u}^1,\mathbf{u}^2} & \mathbf{K}_{\mathbf{u}^1,\widetilde{\mathbf{u}}^1} & \mathbf{K}_{\mathbf{u}^1,\widetilde{\mathbf{u}}^2}\\
\mathbf{K}_{\mathbf{u}^2,\mathbf{u}^1} & \mathbf{K}_{\mathbf{u}^2,\mathbf{u}^2} & \mathbf{K}_{\mathbf{u}^2,\widetilde{\mathbf{u}}^1} & \mathbf{K}_{\mathbf{u}^2,\widetilde{\mathbf{u}}^2}\\
\mathbf{K}_{\widetilde{\mathbf{u}}^1,\mathbf{u}^1} & \mathbf{K}_{\widetilde{\mathbf{u}}^1,\mathbf{u}^2} & \mathbf{K}_{\widetilde{\mathbf{u}}^1,\widetilde{\mathbf{u}}^1} & \mathbf{K}_{\widetilde{\mathbf{u}}^1,\widetilde{\mathbf{u}}^2}\\
\mathbf{K}_{\widetilde{\mathbf{u}}^2,\mathbf{u}^1} & \mathbf{K}_{\widetilde{\mathbf{u}}^2,\mathbf{u}^2} & \mathbf{K}_{\widetilde{\mathbf{u}}^2,\widetilde{\mathbf{u}}^1} & \mathbf{K}_{\widetilde{\mathbf{u}}^2,\widetilde{\mathbf{u}}^2}
\end{bmatrix} \qquad \text{(B.6)}$$

with the matrices defined in Table B.2.

Some remarks about the tangent matrix (B.6):

Table B.2: Block matrices of the continuous-discontinuous consistent tangent matrix.

$\mathbf{K}_{\mathbf{u}^1,\mathbf{u}^1} := \int_\Omega \mathbf{B}^T \boldsymbol{C} \mathbf{B} \, \mathrm{d}\Omega$	$\mathbf{K}_{\mathbf{u}^1,\mathbf{u}^2} := \int_\Omega \psi_{\Gamma_d} \mathbf{B}^T \boldsymbol{C} \mathbf{B} \, \mathrm{d}\Omega$
$\mathbf{K}_{\mathbf{u}^1,\tilde{\mathbf{u}}^1} := -\int_\Omega \mathbf{B}^T \boldsymbol{C} \boldsymbol{\varepsilon} D'(\widetilde{Y}) \frac{\partial \widetilde{Y}}{\partial \widetilde{\boldsymbol{\varepsilon}}} \mathbf{B} \, \mathrm{d}\Omega$	$\mathbf{K}_{\mathbf{u}^1,\tilde{\mathbf{u}}^2} := -\int_\Omega \psi \mathbf{B}^T \boldsymbol{C} \boldsymbol{\varepsilon} D'(\widetilde{Y}) \frac{\partial \widetilde{Y}}{\partial \widetilde{\boldsymbol{\varepsilon}}} \mathbf{B} \, \mathrm{d}\Omega$
$\mathbf{K}_{\mathbf{u}^2,\mathbf{u}^1} := \int_\Omega \psi \mathbf{B}^T \boldsymbol{C} \mathbf{B} \, \mathrm{d}\Omega$	$\mathbf{K}_{\mathbf{u}^2,\mathbf{u}^2} := \int_\Omega \mathbf{B}^T \boldsymbol{C} \mathbf{B} \, \mathrm{d}\Omega + \mathbf{K}_{\text{cohesion}}$
$\mathbf{K}_{\mathbf{u}^2,\tilde{\mathbf{u}}^1} := -\int_\Omega \psi \mathbf{B}^T \boldsymbol{C} \boldsymbol{\varepsilon} D'(\widetilde{Y}) \frac{\partial \widetilde{Y}}{\partial \widetilde{\boldsymbol{\varepsilon}}} \mathbf{B} \, \mathrm{d}\Omega$	$\mathbf{K}_{\mathbf{u}^2,\tilde{\mathbf{u}}^2} := -\int_\Omega \mathbf{B}^T \boldsymbol{C} \boldsymbol{\varepsilon} D'(\widetilde{Y}) \frac{\partial \widetilde{Y}}{\partial \widetilde{\boldsymbol{\varepsilon}}} \mathbf{B} \, \mathrm{d}\Omega$
$\mathbf{K}_{\tilde{\mathbf{u}}^1,\mathbf{u}^1} := -(\mathbf{M} + \ell^2 \mathbf{K}_{\text{BC}})$	$\mathbf{K}_{\tilde{\mathbf{u}}^1,\mathbf{u}^2} := -(\mathbf{M}_\psi + \ell^2 \mathbf{K}_{\psi,\text{BC}})$
$\mathbf{K}_{\tilde{\mathbf{u}}^1,\tilde{\mathbf{u}}^1} := \mathbf{M} + \ell^2 \mathbf{D}$	$\mathbf{K}_{\tilde{\mathbf{u}}^1,\tilde{\mathbf{u}}^2} := \mathbf{M}_\psi + \ell^2 \mathbf{D}_\psi$
$\mathbf{K}_{\tilde{\mathbf{u}}^2,\mathbf{u}^1} := -(\mathbf{M}_\psi + \ell^2 \mathbf{K}_{\psi,\text{BC}})$	$\mathbf{K}_{\tilde{\mathbf{u}}^2,\mathbf{u}^2} := -(\mathbf{M} + \ell^2 \mathbf{K}_{\text{BC}})$
$\mathbf{K}_{\tilde{\mathbf{u}}^2,\tilde{\mathbf{u}}^1} := \mathbf{M}_\psi + \ell^2 \mathbf{D}_\psi$	$\mathbf{K}_{\tilde{\mathbf{u}}^2,\tilde{\mathbf{u}}^2} := \mathbf{M} + \ell^2 \mathbf{D}$

- Matrix $\mathbf{K}_{\mathbf{u}^1,\mathbf{u}^1}$ and the first term in matrix $\mathbf{K}_{\mathbf{u}^2,\mathbf{u}^2}$ are the secant tangent matrices already obtained in the continuous model. Matrices $\mathbf{K}_{\mathbf{u}^1,\mathbf{u}^2}$ and $\mathbf{K}_{\mathbf{u}^2,\mathbf{u}^1}$ may be understood as enriched secant tangent matrices, since the expression is the same, except for the enrichment function.

- Matrices $\mathbf{K}_{\mathbf{u}^1,\tilde{\mathbf{u}}^1}$ and $\mathbf{K}_{\mathbf{u}^2,\tilde{\mathbf{u}}^2}$ are the local tangent matrices. Analogously to secant matrix, matrices $\mathbf{K}_{\mathbf{u}^1,\tilde{\mathbf{u}}^2}$ and $\mathbf{K}_{\mathbf{u}^2,\tilde{\mathbf{u}}^1}$ can be understood as enriched local tangent matrices.

- Matrices $\mathbf{M}$ and $\mathbf{D}$ are the mass and diffusivity matrices already obtained in the continuous model. They are both constant. Matrices $\mathbf{M}_\psi$ and $\mathbf{D}_\psi$ can be understood as enriched mass and enriched diffusivity matrices.

- Matrices $\mathbf{K}_{\text{BC}}$ and $\mathbf{K}_{\psi,\text{BC}}$ take into account the combined boundary conditions.

- It must be stressed that Equation (4.6) is a compact way to express the finite element approximation of the local and non-local displacements after the introduction of the discontinuity. Indeed, let I denote the set of all nodes in the finite element mesh and J the set of nodes of elements crossed by the crack (denoted here as $n_{\text{std.}}$ and $n_{\text{enr.}}$ respectively). Then, Equation (4.6) can also be

expressed as

$$\boldsymbol{u}\left(\boldsymbol{x}\right) \simeq \boldsymbol{u}^h\left(\boldsymbol{x}\right) = \sum_{i\in I} \mathbf{N}_i\left(\boldsymbol{x}\right)\mathbf{u}_i^1 + \sum_{j\in J} \psi\left(\boldsymbol{x}\right)\mathbf{N}_j\left(\boldsymbol{x}\right)\mathbf{u}_j^2 \tag{B.7a}$$

$$\widetilde{\boldsymbol{u}}\left(\boldsymbol{x}\right) \simeq \widetilde{\boldsymbol{u}}^h\left(\boldsymbol{x}\right) = \sum_{i\in I} \mathbf{N}_i\left(\boldsymbol{x}\right)\widetilde{\mathbf{u}}_i^1 + \sum_{j\in J} \psi\left(\boldsymbol{x}\right)\mathbf{N}_j\left(\boldsymbol{x}\right)\widetilde{\mathbf{u}}_j^2 \tag{B.7b}$$

where ψ is the sign function and $\mathbf{N}_i = N_i\mathbf{I}_n$, with N_i the standard bilinear shape function associated with node i and $\mathbf{I}_n$ the identity matrix of size the dimension of the problem n ($n = 1, 2, 3$). Thus, for the sake of simplicity, in Equation (4.6), $\mathbf{N}$ denotes both the array that multiplies the standard nodal degrees of freedom $\mathbf{u}^1$ and $\widetilde{\mathbf{u}}^1$ —of dimension $n_{\text{dof}} \times n_{\text{dof}}$, with n_{dof} the number of standard degrees of freedom ($n_{\text{dof}} = n \times n_{\text{std.}}$)— and the array that multiplies the enriched nodal degrees of freedom $\mathbf{u}^2$ and $\widetilde{\mathbf{u}}^2$ —of dimension $n_{\text{dof}^*} \times n_{\text{dof}^*}$, with n_{dof^*} the number of enriched degrees of freedom ($n_{\text{dof}^*} = n \times n_{\text{enr.}}$).

Analogous comments hold for the array $\mathbf{B}$. It denotes both the array that multiplies the standard $\mathbf{u}^1$, $\widetilde{\mathbf{u}}^1$ and the enriched $\mathbf{u}^2$, $\widetilde{\mathbf{u}}^2$ nodal degrees of freedom.

Therefore, due to this abuse of notation, the mass matrix in $\mathbf{K}_{\widetilde{\mathbf{u}}^1,\mathbf{u}^1}$, for instance, has dimension $n_{\text{dof}} \times n_{\text{dof}}$, while the mass matrix in $\mathbf{K}_{\widetilde{\mathbf{u}}^2,\mathbf{u}^2}$ has dimension $n_{\text{dof}^*} \times n_{\text{dof}^*}$.

- The dimensions of all the enriched matrices change during the numerical simulation, since the number of enriched nodes $n_{\text{enr.}}$ varies during the computation. In particular, $\mathbf{M}_\psi$, $\mathbf{D}_\psi$ and $\mathbf{K}_{\psi,\text{BC}}$ are also affected by this change of dimensions.

  Indeed, let $\mathbf{M}_\psi^{k,i}$ and $\mathbf{D}_\psi^{k,i}$ denote the enriched mass and the enriched diffusivity matrices at a Newton iteration i within a time step k. Besides, let $\mathbf{K}_{\psi,\text{BC}}^{k,i}$ denote the matrix concerning the combined boundary conditions at a iteration i within a time step k.

  On the one hand, since the crack length is considered to be constant during a fixed step,

$$\mathbf{M}_\psi^{k,i} = \mathbf{M}_\psi^{k,i-1} \qquad \forall i \tag{B.8a}$$

$$\mathbf{D}_\psi^{k,i} = \mathbf{D}_\psi^{k,i-1} \qquad \forall i \tag{B.8b}$$

$$\mathbf{K}_{\psi,\text{BC}}^{k,i} = \mathbf{K}_{\psi,\text{BC}}^{k,i-1} \qquad \forall i \tag{B.8c}$$

and the subscript i may be dropped. On the other hand, if the crack length at time step $k-1$ is the same at time step k,

$$\mathbf{M}_{\psi}^{k} = \mathbf{M}_{\psi}^{k-1} \tag{B.9a}$$

$$\mathbf{D}_{\psi}^{k} = \mathbf{D}_{\psi}^{k-1} \tag{B.9b}$$

$$\mathbf{K}_{\psi,\mathrm{BC}}^{k} = \mathbf{K}_{\psi,\mathrm{BC}}^{k-1} \tag{B.9c}$$

That is, in contrast to the continuous tangent matrix, where all the block matrices regarding the regularisation equation are constant, here the block matrices regarding the continuous-discontinuous regularisation equation are not constant. Nevertheless, they change only in those steps where the crack propagates —a low number compared to the total number of load steps of the entire simulation.

- As discussed in Appendix A, the appealing symmetry of Equation (B.6) is due to the fact that the enrichment function is the sign function ($\psi\psi = +1$). Indeed, let us consider the mass matrix of $\mathbf{K}_{\tilde{\mathbf{u}}^2,\tilde{\mathbf{u}}^2}$. It must be stressed that the property

$$\int_{\Omega} \psi \mathbf{N}^T \psi \mathbf{N} \, \mathrm{d}\Omega = \int_{\Omega} \mathbf{N}^T \mathbf{N} \, \mathrm{d}\Omega \tag{B.10}$$

has been considered.

- Matrix $\mathbf{K}_{\mathrm{cohesion}}$ takes into account the cohesive law of the crack. On the one hand, if traction-free cracks are considered, $\mathbf{K}_{\mathrm{cohesion}} = \mathbf{0}$. On the other hand, if cohesive laws are considered, the traction rate at the discontinuity

$$\dot{\boldsymbol{t}}_d = \mathbf{T}[\![\dot{\mathbf{u}}]\!] = \mathbf{T}\left(\mathbf{N}\dot{\mathbf{u}}^2\right)_{|\Gamma_d} \tag{B.11}$$

is introduced, where $\mathbf{T}$ relates traction rate $\dot{\boldsymbol{t}}_d$ and displacement jump rate $[\![\dot{\mathbf{u}}]\!]$. Therefore, if a linear cohesive law is considered, see Chapter 5,

$$\mathbf{K}_{\mathrm{cohesion}} = 2\int_{\Gamma_d} \mathbf{N}^T \mathbf{T} \mathbf{N} \, \mathrm{d}\Gamma \tag{B.12}$$

Appendix C

Numerical integration in X-FEM

An important issue in the implementation of X-FEM is the numerical integration of the weak form. Traditional quadrature rules such as Gauss quadratures cannot adequately integrate discontinuous functions. Therefore, for elements cut by the crack, alternative integration rules should be used, see Belytschko et al. (2009) for a detailed review of these methods. One of these alternative methods consists of subdividing the cracked element into quadrature subdomains with boundaries aligned with the discontinuity, see Moës et al. (1999). In this appendix, this alternative integration scheme is reviewed. Both the two- and three-dimensional schemes are presented. More specifically, the schemes for quadrilateral and hexahedral elements are considered. For illustrative purposes, the numerical integration of the mass matrix in cracked quadrilaterals, Section C.1, and hexahedra, Section C.2, is analysed in detail.

C.1 Quadrature in cracked quadrilaterals

Let us assume a quadrilateral element and a set of points Q_i $(i = 1 \dots N)$ belonging to the simplified medial axis of the isoline $D(\boldsymbol{x}) = D^*$, see Figure C.1(a). Applying first the standard bilinear transformation —from the actual geometry to the reference element— the set of points $P_i = \Phi(Q_i)$ belonging to the bilinear quadrilateral reference element are obtained, see Figure C.1(b).

Then, the crack is considered to be the straight line $r := a\xi + b\eta + c = 0$ such

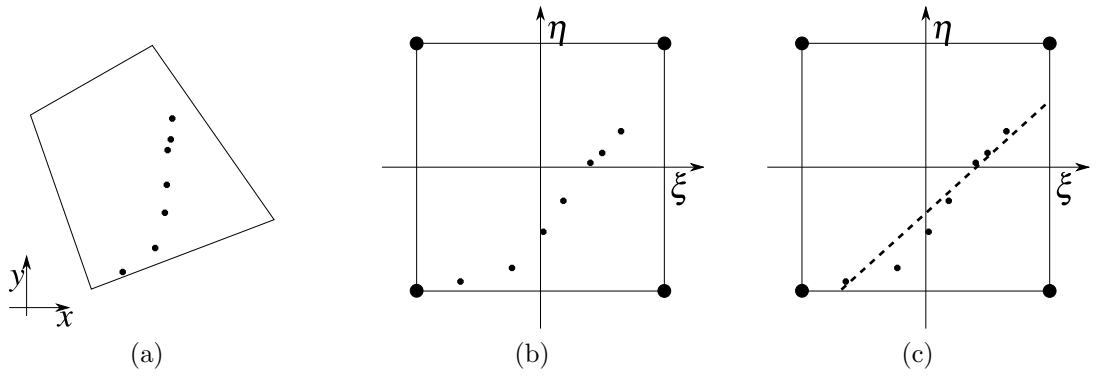

(a) (b) (c)

Figure C.1: (a) The quadrilateral element and the set of points Q_i that belong to the $\theta-$SMA of the isoline $D(\boldsymbol{x}) = D^*$ (b) are mapped to the bilinear reference element. (c) Then, the propagating discontinuity is obtained by minimising the sum of distances from P_i to the crack r.

that the sum of distances from P_i to the line r

$$D = \sum_{i=1}^{N} d_i = \sum_{i=1}^{n} d(r, P_i) = \frac{|a\xi_i + b\eta_i + c|}{\sqrt{a^2 + b^2}} \tag{C.1}$$

is minimum, see Figure C.1(c).

Hence, the crack is assumed to be a piecewise linear interface in the reference domain. Then, as proposed by Moës et al. (1999), the cracked quadrilateral is decomposed into subelements whose boundaries align with the discontinuity, see Figure C.2(a). Although special quadratures are available for polygons with n edges, a further decomposition into quadrilaterals and triangles is useful. In this work, the cracked quadrilateral element is decomposed into two subelements that are further triangulated, see Figure C.2(b). Then, each triangular subdomain is mapped to a parent unit triangle over which a standard Gauss quadrature may be considered, since the functions to be integrated are continuous within the triangles, see Figure C.2(c).

C.1.1 Numerical integration of the mass matrix

As discussed in Appendix B, smoothed displacements are attractive from a computational viewpoint, especially regarding the computation of the consistent tangent matrix needed to achieve quadratic convergence in the Newton-Raphson method, see Equation (B.6). Regarding the finite element discretisation of the regularisation equa-

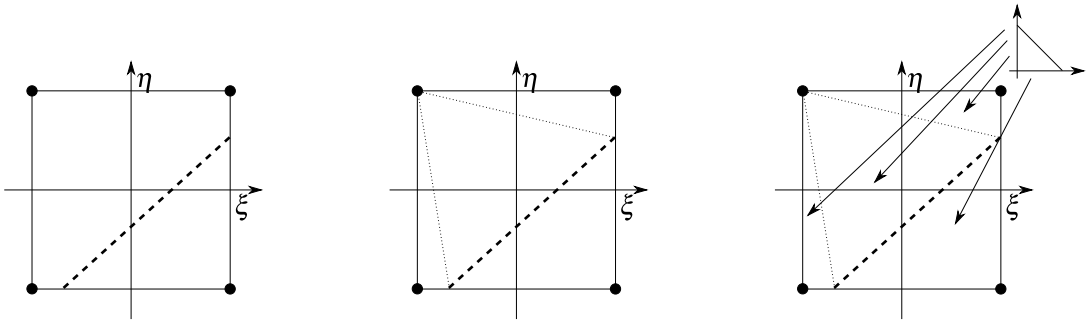

(a) (b) (c)

Figure C.2: (a) The straight crack cuts the reference element into a triangle and a pentagon, (b) which is further divided into triangles. (c) Then, each triangular subdomain is mapped to a parent unit triangle.

tion, the mass and the diffusivity matrices —both the standard and the enriched— need to be exactly computed. Note that if the shape functions are exactly integrated —that is, the mass matrix is exactly computed—, the shape function gradients are also exactly integrated thus leading to the exact integration of the diffusivity matrix. Hence, for illustrative purposes, the integration of the enriched mass matrix is analysed in detail.

To compute the mass matrix, we need to integrate

$$I := \int_{\Omega} f(x,y)\,\mathrm{d}x\,\mathrm{d}y \tag{C.2}$$

where $f(x,y) = N_i(x,y)N_j(x,y)$.

Applying the first transformation —from the actual geometry to the reference element— one obtains

$$I := \int_{\Omega} f(x,y)\,\mathrm{d}x\,\mathrm{d}y = \int_{-1}^{1}\int_{-1}^{1} f_*(\xi,\eta)\cdot|J(\xi,\eta)|\,\mathrm{d}\xi\,\mathrm{d}\eta \tag{C.3}$$

where $f_*(\xi,\eta) = f(\Phi_\xi(\xi,\eta),\Phi_\eta(\xi,\eta))$ and J denotes the determinant of the Jacobian matrix of this first transformation.

Then, applying the second transformation —from each triangular subdomain to the parent unit triangle— one obtains

$$I := \sum_{i=1}^{\mathrm{S}} g(\hat{\xi},\hat{\eta}) \tag{C.4}$$

where S is the number of triangular subdomains and

$$g(\hat{\xi},\hat{\eta}) = \int_0^1 \int_0^{1-\hat{\eta}} f_{**}(\hat{\xi},\hat{\eta}) \cdot |J(\hat{\Phi}_{\hat{\xi}}(\hat{\xi},\hat{\eta}), \hat{\Phi}_{\hat{\eta}}(\hat{\xi},\hat{\eta}))| \cdot |\hat{J}(\hat{\xi},\hat{\eta})| \, \mathrm{d}\hat{\xi} \, \mathrm{d}\hat{\eta} \tag{C.5}$$

where $f_{**}(\hat{\xi},\hat{\eta}) = f_*(\hat{\Phi}_{\hat{\xi}}(\hat{\xi},\hat{\eta}), \hat{\Phi}_{\hat{\eta}}(\hat{\xi},\hat{\eta}))$ and $\hat{J}$ denotes the determinant of the Jacobian matrix of the second transformation.

Therefore, and regarding the first transformation, the monomials of maximum degree to be exactly integrated are

$$\begin{array}{rcl} N_i N_j & \rightarrow & \xi^2\eta^2 \\ |J(\xi,\eta)| & \rightarrow & \xi, \eta \\ \hline & & \xi^3\eta^2, \xi^2\eta^3 \end{array}$$

Since the second transformation is linear, the monomials of maximum degree to be exactly integrated are $\xi^3\eta^2, \xi^2\eta^3$, which leads to a quadrature of degree 5 for triangles (e.g. a quadrature with $N_g = 7$ points), see Felippa (2004).

C.2 Quadrature in cracked hexahedra

Let us suppose a hexahedral element and a set of points Q_i $(i = 1 \dots N)$ belonging to the simplified medial surface of the isosurface $D(\boldsymbol{x}) = D^*$, see Figure C.3(a). Analogously to a two-dimensional setting, the crack is considered to be the plane $\Pi := a\xi + b\eta + c\zeta + d = 0$ such that the sum of distances from $P_i = \Phi(Q_i)$, see Figure C.3(b), to the plane Π

$$D = \sum_{i=1}^{N} d_i = \sum_{i=1}^{n} d(\Pi, P_i) = \frac{|a\xi_i + b\eta_i + c\zeta_i + d|}{\sqrt{a^2 + b^2 + c^2}} \tag{C.6}$$

is minimum, see Figure C.3(c).

Then, the cracked hexahedral element is decomposed into two polyhedra whose boundaries align with the discontinuity, see Figure C.4(a), that are further decomposed into tetrahedral subelements, see Figure C.4(b). Then, each tetrahedral subelement is mapped to a unit tetrahedron, see Figure C.4(c).

C.2.1 Numerical integration of the mass matrix

Analogously to the two-dimensional case, the enriched mass —and diffusivity— matrices must be computed. In a three-dimensional setting, to compute the mass matrix,

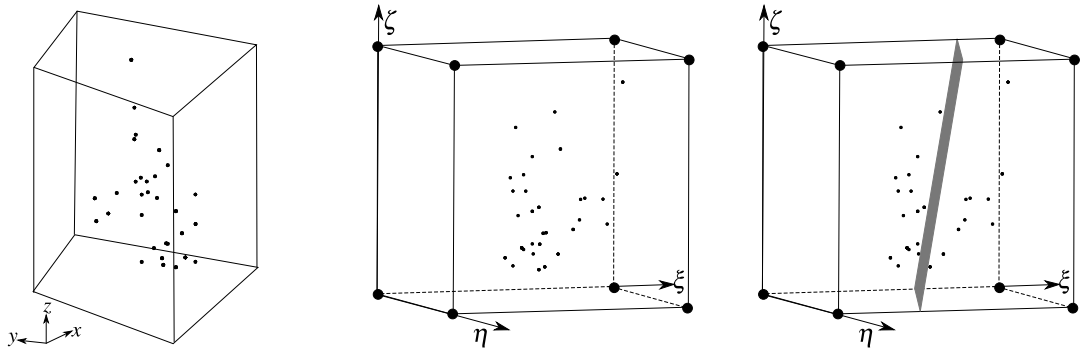

(a) (b) (c)

Figure C.3: (a) The hexahedral element and the set of points Q_i that belong to the $\theta-$SMA of the isosurface $D(\boldsymbol{x}) = D^*$ (b) are mapped to the eight-noded reference element. (c) Then, the propagating discontinuity is obtained by minimising the sum of distances from P_i to the crack Π.

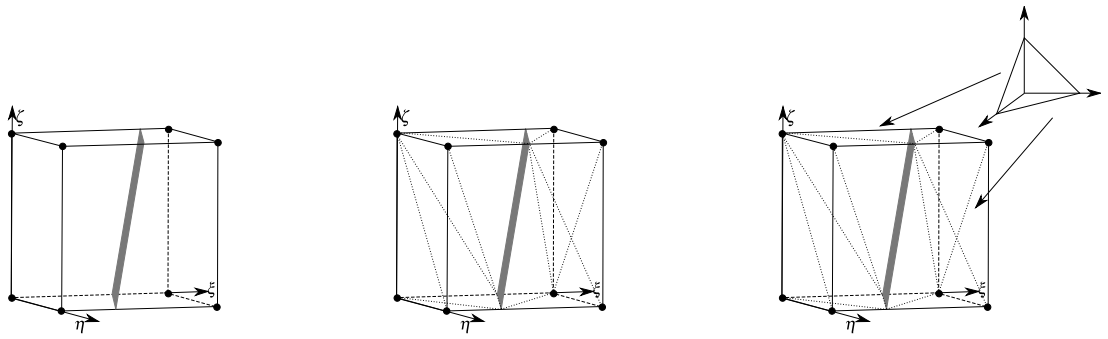

(a) (b) (c)

Figure C.4: (a) The plane cuts the reference element into two different polyhedra, (b) which is further divided into tetrahedra. (c) Then, each tetrahedral subdomain is mapped to a parent unit tetrahedron.

we need to integrate

$$I := \int_\Omega f(x,y,z)\,\mathrm{d}x\,\mathrm{d}y\,\mathrm{d}z \tag{C.7}$$

where $f(x,y,z) = N_i(x,y,z)N_j(x,y,z)$.

Applying the first transformation —from the actual geometry to the reference element— one obtains

$$I := \int_\Omega f(x,y,z)\,\mathrm{d}x\,\mathrm{d}y\,\mathrm{d}z = \int_{-1}^{1}\int_{-1}^{1}\int_{-1}^{1} f_*(\xi,\eta,\zeta)\cdot|J(\xi,\eta,\zeta)|\,\mathrm{d}\xi\,\mathrm{d}\eta\,\mathrm{d}\zeta \tag{C.8}$$

where $f_*(\xi,\eta,\zeta) = f(\Phi_\xi(\xi,\eta,\zeta), \Phi_\eta(\xi,\eta,\zeta), \Phi_\zeta(\xi,\eta,\zeta))$ and J denotes the determinant of the Jacobian matrix of this first transformation.

Analogously to a two-dimensional setting, see Section C.1, the second transformation is linear. Therefore, the monomials of maximum degree to be exactly integrated are

$$\begin{array}{rcc} N_i N_j & \rightarrow & \xi^2\eta^2\zeta^2 \\ |J(\xi,\eta,\zeta)| & \rightarrow & \xi^2\eta\zeta, \xi\eta^2\zeta, \xi\eta\zeta^2 \\ \hline & & \xi^4\eta^3\zeta^3, \xi^3\eta^4\zeta^3, \xi^3\eta^3\zeta^4 \end{array}$$

thus leading to a quadrature of degree 10 for tetrahedra.

Bibliography

Armero, F. and K. Garikipati (1996). An analysis of strong discontinuities in multiplicative finite strain plasticity and their relation with the numerical simulation of strain localization in solids. *International Journal of Solids and Structures 33*(20-22), 2863–2885. doi: 10.1016/0020-7683(95)00257-X.

Babuška, I. and J. M. Melenk (1997). The partition of unity method. *International Journal for Numerical Methods in Engineering 40*(4), 727–758. doi: 10.1002/(SICI)1097-0207(19970228)40:4<727::AID-NME86>3.0.CO;2-N.

Barenblatt, G. I. (1962). *The Mathematical Theory of Equilibrium Cracks in Brittle Fracture*, Volume 7 of *Advances in Applied Mechanics*, pp. 55–129. Elsevier. doi: 10.1016/S0065-2156(08)70121-2.

Bažant, Z. (2000). Size effect. *International Journal of Solids and Structures 37*(1–2), 69–80. doi: 10.1016/S0020-7683(99)00077-3.

Bažant, Z. and M. Jirásek (2002). Nonlocal Integral Formulations of Plasticity and Damage: Survey of Progress. *Journal of Engineering Mechanics 128*(11), 1119–1149. doi: 10.1061/(ASCE)0733-9399(2002)128:11(1119).

Bažant, Z. and F. B. Lin (1988). Nonlocal Smeared Cracking Model for Concrete Fracture. *Journal of Structural Engineering 114*(11), 2493–2510. doi: 10.1061/(ASCE)0733-9445(1988)114:11(2493).

Bažant, Z. and B. H. Oh (1983). Crack band theory for fracture of concrete. *Matériaux et Construction 16*(3), 155–177. doi: 10.1007/BF02486267.

Bažant, Z. and G. Pijaudier-Cabot (1988). Nonlocal Continuum Damage, Localization Instability and Convergence. *Journal of Applied Mechanics 55*(2), 287–293. doi: 10.1115/1.3173674.

Belytschko, T. and T. Black (1999). Elastic crack growth in finite elements with minimal remeshing. *International Journal for Numerical Methods in Engineering 45*(5), 601–620. doi: 10.1002/(SICI)1097-0207(19990620)45:5<601::AID-NME598>3.0.CO;2-S.

Belytschko, T., J. Fish, and B. E. Engelmann (1988). A finite element with embedded localization zones. *Computer Methods in Applied Mechanics and Engineering 70*(1), 59–89. doi: 10.1016/0045-7825(88)90180-6.

Belytschko, T., R. Gracie, and G. Ventura (2009). A review of extended/generalized finite element methods for material modeling. *Modelling and Simulation in Materials Science and Engineering 17*(4), 043001. doi: 10.1088/0965-0393/17/4/043001.

Belytschko, T., Y. Krongauz, D. Organ, M. Fleming, and P. Krysl (1996). Meshless methods: An overview and recent developments. *Computer Methods in Applied Mechanics and Engineering 139*(1-4), 3–47. doi: 10.1016/S0045-7825(96)01078-X.

Benvenuti, E., B. Loret, and A. Tralli (2004). A unified multifield formulation in nonlocal damage. *European Journal of Mechanics - A/Solids 23*(4), 539–559. doi: 10.1016/j.euromechsol.2004.03.005.

Benvenuti, E. and A. Tralli (2012). Simulation of finite-width process zone in concrete-like materials by means of a regularized extended finite element model. *Computational Mechanics 50*(4), 479–497. doi: 10.1007/s00466-012-0685-y.

Bernard, P. E., N. Moës, and N. Chevaugeon (2012). Damage growth modeling using the Thick Level Set (TLS) approach: Efficient discretization for quasi-static loadings. *Computer Methods in Applied Mechanics and Engineering 233-236*(0), 11–27. doi: 10.1016/j.cma.2012.02.020.

Blum, H. (1967). A transformation for extracting new descriptors of shape. *Models for the perception of speech and visual form 19*(5), 362–380.

Bouchard, P. O., F. Bay, Y. Chastel, and I. Tovena (2000). Crack propagation modelling using an advanced remeshing technique. *Computer Methods in Applied Mechanics and Engineering 189*(3), 723–742. doi: 10.1016/S0045-7825(99)00324-2.

Bourdin, B., G. A. Francfort, and J. J. Marigo (2000). Numerical experiments in revisited brittle fracture. *Journal of the Mechanics and Physics of Solids 48*(4), 797–826. doi: 10.1016/S0022-5096(99)00028-9.

Cazes, F., M. Coret, A. Combescure, and A. Gravouil (2009). A thermodynamic method for the construction of a cohesive law from a nonlocal damage model. *International Journal of Solids and Structures 46*(6), 1476–1490. doi: 10.1016/j.ijsolstr.2008.11.019.

Cazes, F., A. Simatos, M. Coret, and A. Combescure (2010). A cohesive zone model which is energetically equivalent to a gradient-enhanced coupled damage-plasticity model. *European Journal of Mechanics - A/Solids 29*(6), 976–989. doi: doi:10.1016/j.euromechsol.2009.11.003.

Cervera, M., M. Chiumenti, and R. Codina (2011). Mesh objective modeling of cracks using continuous linear strain and displacement interpolations. *International Journal for Numerical Methods in Engineering 87*(10), 962–987. doi: 10.1002/nme.3148.

Cervera, M., L. Pelà, R. Clemente, and P. Roca (2010). A crack-tracking technique for localized damage in quasi-brittle materials. *Engineering Fracture Mechanics 77*(13), 2431–2450. doi: 10.1016/j.engfracmech.2010.06.013.

Comi, C. (1999). Computational modelling of gradient-enhanced damage in quasi-brittle materials. *Mechanics of Cohesive-frictional Materials 4*(1), 17–36. doi: 10.1002/(SICI)1099-1484(199901)4:1<17::AID-CFM55>3.0.CO;2-6.

Comi, C. (2001). A non-local model with tension and compression damage mechanisms. *European Journal of Mechanics - A/Solids 20*(1), 1–22. doi: 10.1016/S0997-7538(00)01111-6.

Comi, C., S. Mariani, and U. Perego (2007). An extended FE strategy for transition from continuum damage to mode I cohesive crack propagation. *International Journal for Numerical and Analytical Methods in Geomechanics 31*(2), 213–238. doi: 10.1002/nag.537.

Cundall, P. A. and O. D. L. Strack (1979). A discrete numerical model for granular assemblies. *Géotechnique 29*(1), 47–65. doi: 10.1680/geot.1979.29.1.47.

Cuvilliez, S., F. Feyel, E. Lorentz, and S. Michel-Ponnelle (2012). A finite element approach coupling a continuous gradient damage model and a cohesive zone model within the framework of quasi-brittle failure. *Computer Methods in Applied Mechanics and Engineering 237–240*(0), 244–259. doi: 10.1016/j.cma.2012.04.019.

Daux, C., N. Moës, J. Dolbow, N. Sukumar, and T. Belytschko (2000). Arbitrary branched and intersecting cracks with the extended finite element method. *International Journal for Numerical Methods in Engineering 48*(12), 1741–1760. doi: 10.1002/1097-0207(20000830)48:12<1741::AID-NME956>3.0.CO;2-L.

de Borst, R., J. Pamin, R. H. J. Peerlings, and L. J. Sluys (1995). On gradient-enhanced damage and plasticity models for failure in quasi-brittle and frictional materials. *Computational Mechanics 17*(1-2), 130–141. doi: 10.1007/BF00356485.

de Vree, J. H. P., W. A. M. Brekelmans, and M. A. J. van Gils (1995). Comparison of nonlocal approaches in continuum damage mechanics. *Computers and Structures 55*(4), 581–588. doi: 10.1016/0045-7949(94)00501-S.

Dufour, F., G. Legrain, G. Pijaudier-Cabot, and A. Huerta (2012). Estimation of crack opening from a two-dimensional continuum-based finite element computation. *International Journal for Numerical and Analytical Methods in Geomechanics 36*(16), 1813–1830. doi: 10.1002/nag.1097.

Dufour, F., G. Pijaudier-Cabot, M. Choinska, and A. Huerta (2008). Extraction of a crack opening from a continuous approach using regularized damage models. *Computers and Concrete 5*(4), 375–388.

Dugdale, D. S. (1960). Yielding of steel sheets containing slits. *Journal of the Mechanics and Physics of Solids 8*(2), 100–104. doi: 10.1016/0022-5096(60)90013-2.

Felippa, C. A. (2004). A compendium of FEM integration formulas for symbolic work. *Engineering Computations 21*(8), 867–890. doi: 10.1108/02644400410554362.

Foskey, M., M. C. Lin, and D. Manocha (2003). Efficient computation of a simplified medial axis. In *Proceedings of the eighth ACM symposium on Solid modeling and applications*, SM '03, New York, NY, USA, pp. 96–107. ACM. doi: 10.1145/781606.781623.

Francfort, G. A. and J. J. Marigo (1998). Revisiting brittle fracture as an energy minimization problem. *Journal of the Mechanics and Physics of Solids 46*(8), 1319–1342. doi: 10.1016/S0022-5096(98)00034-9.

Fries, T. P. and T. Belytschko (2010). The extended/generalized finite element method: An overview of the method and its applications. *International Journal for Numerical Methods in Engineering 84*(3), 253–304. doi: 10.1002/nme.2914.

Grassl, P. and M. Jirásek (2010). Meso-scale approach to modelling the fracture process zone of concrete subjected to uniaxial tension. *International Journal of Solids and Structures 47*(7–8), 957–968. doi: 10.1016/j.ijsolstr.2009.12.010.

Hillerborg, A., M. Modéer, and P. E. Petersson (1976). Analysis of crack formation and crack growth in concrete by means of fracture mechanics and finite elements. *Cement and Concrete Research 6*(6), 773–781. doi: 10.1016/0008-8846(76)90007-7.

Jirásek, M. (1998). Nonlocal models for damage and fracture: Comparison of approaches. *International Journal of Solids and Structures 35*(31-32), 4133–4145. doi: 10.1016/S0020-7683(97)00306-5.

Jirásek, M. (2000). Comparative study on finite elements with embedded discontinuities. *Computer Methods in Applied Mechanics and Engineering 188*(1-3), 307–330. doi: 10.1016/S0045-7825(99)00154-1.

Jirásek, M. (2002). Objective modeling of strain localization. *Revue Française de Génie Civil 6*(6), 1119–1132. doi: 10.1080/12795119.2002.9692735.

Jirásek, M. (2007). Mathematical analysis of strain localization. *Revue Européenne de Génie Civil 11*(7-8), 977–991. doi: 10.1080/17747120.2007.9692973.

Jirásek, M. and M. Bauer (2012). Numerical aspects of the crack band approach. *Computers and Structures 110–111*(0), 60–78. doi: 10.1016/j.compstruc.2012.06.006.

Jirásek, M. and T. Belytschko (2002). Computational resolution of strong discontinuities. In *Proceedings of Fifth World Congress on Computational Mechanics, WCCM V, Vienna University of Technology, Austria*.

Jirásek, M. and S. Marfia (2005). Non-local damage model based on displacement averaging. *International Journal for Numerical Methods in Engineering 63*(1), 77–102. doi: 10.1002/nme.1262.

Jirásek, M. and S. Marfia (2006). Nonlocal damage models: displacement-based formulations. In *Proceedings of EURO- C2006: Computational Modelling of Concrete Structures*, pp. 381–390.

Jirásek, M. and T. Zimmermann (2001). Embedded crack model. Part II: combination with smeared cracks. *International Journal for Numerical Methods in Engineering 50*(6), 1291–1305. doi: 10.1002/1097-0207(20010228)50:6<1291::AID-NME12>3.0.CO;2-Q.

Kawai, T. (1978). New discrete models and their application to seismic response analysis of structures. *Nuclear Engineering and Design 48*(1), 207–229. doi: 10.1016/0029-5493(78)90217-0.

Krayani, A., G. Pijaudier-Cabot, and F. Dufour (2009). Boundary effect on weight function in nonlocal damage model. *Engineering Fracture Mechanics 76*(14), 2217–2231. doi: 10.1016/j.engfracmech.2009.07.007.

Lemaitre, J. and J. L. Chaboche (1990). *Mechanics of solid materials*. Cambridge University Press. ISBN-10: 0521328535.

Mazars, J. (1986). A description of micro- and macroscale damage of concrete structures. *Engineering Fracture Mechanics 25*(5–6), 729–737. doi: 10.1016/0013-7944(86)90036-6.

Mazars, J. and G. Pijaudier-Cabot (1996). From damage to fracture mechanics and conversely: A combined approach. *International Journal of Solids and Structures 33*(20–22), 3327–3342. doi: 10.1016/0020-7683(96)00015-7.

Melenk, J. M. and I. Babuška (1996). The partition of unity finite element method: Basic theory and applications. *Computer Methods in Applied Mechanics and Engineering 139*(1–4), 289–314. doi: 10.1016/S0045-7825(96)01087-0.

Moës, N., J. Dolbow, and T. Belytschko (1999). A finite element method for crack growth without remeshing. *International Journal for Numerical Methods in Engineering 46*(1), 131–150. doi: 10.1002/(SICI)1097-0207(19990910)46:1<131::AID-NME726>3.0.CO;2-J.

Moës, N., C. Stolz, P. E. Bernard, and N. Chevaugeon (2011). A level set based model for damage growth: The thick level set approach. *International Journal for Numerical Methods in Engineering 86*(3), 358–380. doi: 10.1002/nme.3069.

Mühlhaus, H. B. and E. C. Alfantis (1991). A variational principle for gradient plasticity. *International Journal of Solids and Structures 28*(7), 845 – 857. doi: 10.1016/0020-7683(91)90004-Y.

Nguyen, V. P., T. Rabczuk, S. Bordas, and M. Duflot (2008). Meshless methods: A review and computer implementation aspects. *Mathematics and Computers in Simulation 79*(3), 763–813. doi: 10.1016/j.matcom.2008.01.003.

Oliver, J. and A. E. Huespe (2004). Continuum approach to material failure in strong discontinuity settings. *Computer Methods in Applied Mechanics and Engineering 193*(30-32), 3195–3220. doi: 10.1016/j.cma.2003.07.013.

Oliver, J., A. E. Huespe, and P. Sanchez (2006). A comparative study on finite elements for capturing strong discontinuities: E-FEM vs X-FEM. *Computer Methods in Applied Mechanics and Engineering 195*(37-40), 4732–4752. doi: 10.1016/j.cma.2005.09.020.

Ortiz, M., Y. Leroy, and A. Needleman (1987). A finite element method for localized failure analysis. *Computer Methods in Applied Mechanics and Engineering 61*(2), 189–214. doi: 10.1016/0045-7825(87)90004-1.

Peerlings, R. H. J., R. de Borst, W. A. M. Brekelmans, and J. H. P. de Vree (1996). Gradient enhanced damage for quasi-brittle materials. *International Journal for Numerical Methods in Engineering 39*(19), 3391–3403. doi: 10.1002/(SICI)1097-0207(19961015)39:19<3391::AID-NME7>3.0.CO;2-D.

Peerlings, R. H. J., R. de Borst, W. A. M. Brekelmans, and M. G. D. Geers (1998). Gradient-enhanced damage modelling of concrete fracture. *Mechanics of Cohesive-frictional Materials 3*(4), 323–342. doi: 10.1002/(SICI)1099-1484(1998100)3:4<323::AID-CFM51>3.0.CO;2-Z.

Peerlings, R. H. J., M. G. D. Geers, R. de Borst, and W. A. M. Brekelmans (2001). A critical comparison of nonlocal and gradient-enhanced softening continua. *International Journal of Solids and Structures 38*(44–45), 7723–7746. doi: 10.1016/S0020-7683(01)00087-7.

Pijaudier-Cabot, G. and Z. Bažant (1987). Nonlocal Damage Theory. *Journal of Engineering Mechanics 113*(10), 1512–1533. doi: 10.1061/(ASCE)0733-9399(1987)113:10(1512).

Pijaudier-Cabot, G. and F. Dufour (2010). Non local damage model: boundary and evolving boundary effects. *European Journal of Environmental and Civil Engineering 14*(6-7), 729–749. doi: 10.1080/19648189.2010.9693260.

Pizer, S. M., K. Siddiqi, G. Székely, J. N. Damon, and S. W. Zucker (2003). Multiscale Medial Loci and Their Properties. *International Journal of Computer Vision 55*(2–3), 155–179. doi: 10.1023/A:1026135101267.

Polizzotto, C. (2003). Gradient elasticity and nonstandard boundary conditions. *International Journal of Solids and Structures 40*(26), 7399–7423. doi: 10.1016/j.ijsolstr.2003.06.001.

Rabczuk, T. (2013). Computational Methods for Fracture in Brittle and Quasi-Brittle Solids: State-of-the-Art Review and Future Perspectives. *ISRN Applied Mathematics 2013*, 38 pages. doi: 10.1155/2013/849231.

Rodríguez-Ferran, A., T. Bennett, H. Askes, and E. Tamayo-Mas (2011). A general framework for softening regularisation based on gradient elasticity. *International Journal of Solids and Structures 48*(9), 1382–1394. doi: 10.1016/j.ijsolstr.2011.01.022.

Rodríguez-Ferran, A. and A. Huerta (2000). Error estimation and adaptivity for nonlocal damage models. *International Journal of Solids and Structures 37*(48–50), 7501–7528. doi: 10.1016/S0020-7683(00)00209-2.

Rodríguez-Ferran, A., I. Morata, and A. Huerta (2005). A new damage model based on non-local displacements. *International Journal for Numerical and Analytical Methods in Geomechanics 29*(5), 473–493. doi: 10.1002/nag.422.

Seabra, M. R. R., J. M. A. César de Sá, F. X. C. Andrade, and F. M. A. Pires (2011). Continuous-discontinuous formulation for ductile fracture. *International Journal of Material Forming 4*(3), 271–281. doi: 10.1007/s12289-010-0991-x.

Simo, J. C. and J. Oliver (1994). A new approach to the analysis and simulation of strain softening in solids. In *Fracture and damage in quasibrittle structures*, pp. 25–39.

Simo, J. C., J. Oliver, and F. Armero (1993). An analysis of strong discontinuities induced by strain-softening in rate-independent inelastic solids. *Computational Mechanics 12*(5), 277–296. doi: 10.1007/BF00372173.

Simone, A., H. Askes, and L. J. Sluys (2004). Incorrect initiation and propagation of failure in non-local and gradient-enhanced media. *International Journal of Solids and Structures 41*(2), 351–363. doi: 10.1016/j.ijsolstr.2003.09.020.

Simone, A., G. N. Wells, and L. J. Sluys (2003). From continuous to discontinuous failure in a gradient-enhanced continuum damage model. *Computer Methods in Applied Mechanics and Engineering 192*(41–42), 4581–4607. doi: 10.1016/S0045-7825(03)00428-6.

Stolarska, M., D. L. Chopp, N. Moës, and T. Belytschko (2001). Modelling crack growth by level sets in the extended finite element method. *International Journal for Numerical Methods in Engineering 51*(8), 943–960. doi: 10.1002/nme.201.

Suresh, K. (2013). 2D Medial Axis Computation. `http://www.mathworks.com/matlabcentral/fileexchange/12399-2-d-medial-axis-computation`. Last accessed on 2013-08-07.

Tamayo-Mas, E. and A. Rodríguez-Ferran (2012). Condiciones de contorno en modelos de gradiente con desplazamientos suavizados. *Revista Internacional de Métodos Numéricos para Cálculo y Diseño en Ingeniería 28*(3), 170–176. doi: 10.1016/j.rimni.2012.03.006.

Wells, G. N., L. J. Sluys, and R. de Borst (2002). Simulating the propagation of displacement discontinuities in a regularized strain-softening medium. *International Journal for Numerical Methods in Engineering 53*(5), 1235–1256. doi: 10.1002/nme.375.

Yoshizawa, S. (2013). SM03Skeleton. `http://www.riken.jp/brict/Yoshizawa/Research/Skeleton.html`. Last accessed on 2013-08-07.

Zlotnik, S. and P. Díez (2009). Hierarchical X-FEM for n-phase flow (n > 2). *Computer Methods in Applied Mechanics and Engineering 198*(30–32), 2329–2338. doi: 10.1016/j.cma.2009.02.025.